The Dissertation Committee for James Madigan Loy certifies that this is the approved version of the following dissertation:

An Efficient Solution Procedure for Simulating Phonon Transport in Multiscale Multimaterial Systems

Committee:

Jayathi Y. Murthy, Supervisor

Sanjay R. Mathur

Li Shi

Robert Moser

Matthew McNenly

An Efficient Solution Procedure for Simulating Phonon Transport in Multiscale Multimaterial Systems

by

James Madigan Loy, B. S. M. E.; M. S. M. E.

Dissertation

Presented to the Faculty of the Graduate School of

The University of Texas at Austin

in Partial Fulfillment

of the Requirements

for the Degree of

Doctor of Philosophy

The University of Texas at Austin

May 2013

Dedication

For my Mother and Father-- a constant source of support and inspiration.

Acknowledgments

I must first acknowledge my advisor, Jayathi Murthy. The past six years of my life have been so amazing because I have had the privilege of working with such a brilliant, passionate, nurturing, and kind person. From our first meeting, through our move to Austin, to the time of my defense, she has been very supportive of me, and I never fail to learn from her.

I am also very thankful to my committee members: Dr. Robert Moser, Dr. Li Shi, Dr. Sanjay Mathur, and Dr. Matthew McNenly. In particular, I would like to thank Dr. Mathur for helping me immensely with the development of COMET, and always having faith in my abilities. I would also like to thank Dr. McNenly for his help during my stay at Lawrence Livermore National Laboratory, and continuing to be a friend and a mentor.

If not for my lab mates, the transition from Purdue University to The University of Texas would have been exceedingly difficult. I am grateful to have worked with very kind and smart people: Ben Pax, Columbia Mishra, Prabhakar Marepalli, Ajay Vadakkepatt, Brad Trembacki, Dr. Dhruv Singh, Dr. Shankhadeep Das, and Dr. Chandra Varanasi. I especially would like to thank Ajay Vadakkepatt and Brad Trembacki for their help in developing the sequential solver for gray interface transport. I would also like to thank Dr. Dhruv Singh for providing the silicon and germanium dispersion relations as well as for many helpful conversations. I would also like to thank Prabhakar Marepalli and Columbia Mishra for helping me practice my defense.

I have had several conversations with Dr. Alan McGaughey, which were very helpful in understanding the behavior of phonons in nanoparticle composites.

Finally, I would like to thank my parents, to whom this dissertation is dedicated. Without your help, I would not have gotten where I am today. Thank you for everything that I am, and that I hope to be.

An Efficient Solution Procedure for Simulating Phonon Transport in Multiscale Multimaterial Systems

James Madigan Loy, Ph. D.

The University of Texas at Austin, 2013

Supervisor: Jayathi Y. Murthy

Over the last two decades, advanced fabrication techniques have enabled the fabrication of materials and devices at sub-micron length scales. For heat conduction, the conventional Fourier model for predicting energy transport has been shown to yield erroneous results on such length scales. In semiconductors and dielectrics, energy transport occurs through phonons, which are quanta of lattice vibrations. When phase coherence effects can be ignored, phonon transport may be modeled using the semi-classical phonon Boltzmann transport equation (BTE). The objective of this thesis is to develop an efficient computational method to solve the BTE, both for single-material and multi-material systems, where transport across heterogeneous interfaces is expected to play a critical role. The resulting solver will find application in the design of microelectronic circuits and thermoelectric devices.

The primary source of computational difficulties in solving the phonon BTE lies in the scattering term, which redistributes phonon energies in wave-vector space. In its complete form, the scattering term is non-linear, and is non-zero only when energy and momentum conservation rules are satisfied. To reduce complexity, scattering interactions are often approximated by the single mode relaxation time (SMRT) approximation,

which couples different phonon groups to each other through a thermal bath at the equilibrium temperature.

The most common methods for solving the BTE in the SMRT approximation employ sequential solution techniques which solve for the spatial distribution of the phonon energy of each phonon group one after another. Coupling between phonons is treated explicitly and updated after all phonon groups have been solved individually. When the domain length is small compared to the phonon mean free path, corresponding to a high Knudsen number ($Kn=\lambda/L$, where λ is the phonon mean free path), this sequential procedure works well. At low Knudsen number, however, this procedure suffers long convergence times because the coupling between phonon groups is very strong for an explicit treatment of coupling to suffice. In problems of practical interest, such as silicon-based microelectronics, for example, phonon groups have a very large spread in mean free paths, resulting in a combination of high and low Knudsen number; in these problems, it is virtually impossible to obtain solutions using sequential solution techniques.

In this thesis, a new computational procedure for solving the non-gray phonon BTE under the SMRT approximation is developed. This procedure, called the coupled ordinates method (COMET), is shown to achieve significant solution acceleration over the sequential solution technique for a wide range of Knudsen numbers. Its success lies in treating phonon-phonon coupling implicitly through a direct solution of all equations in wave vector space at a particular spatial location. To increase coupling in the spatial domain, this procedure is embedded as a relaxation sweep in a geometric multigrid. Due to the heavy computational load at each spatial location, COMET exhibits excellent scaling on parallel platforms using domain decomposition. On serial platforms, COMET is shown to achieve accelerations of 60 times over the sequential procedure for $Kn<1.0$

for gray phonon transport problems, and accelerations of 233 times for non-gray problems.

COMET is then extended to include phonon transport across heterogeneous material interfaces using the diffuse mismatch model (DMM). Here, coupling between phonon groups occurs because of reflection and transmission. Efficient algorithms, based on heuristics, are developed for interface agglomeration in creating coarse multigrid levels. COMET is tested for phonon transport problems with multiple interfaces and shown to outperform the sequential technique.

Finally, the utility of COMET is demonstrated by simulating phonon transport in a nanoparticle composite of silicon and germanium. A realistic geometry constructed from x-ray CT scans is employed. This composite is typical of those which are used to reduce lattice thermal conductivity in thermoelectric materials. The effective thermal conductivity of the composite is computed for two different domain sizes over a range of temperatures. It is found that for low temperatures, the thermal conductivity increases with temperature because interface scattering dominates, and is insensitive to temperature; the increase of thermal conductivity is primarily a result of the increase in phonon population with temperature consistent with Bose-Einstein statistics. At higher temperatures, Umklapp scattering begins to take over, causing a peak in thermal conductivity and a subsequent decrease with temperature. However, unlike bulk materials, the peak is shallow, consistent with the strong role of interface scattering. The interaction of phonon mean free path with the particulate length scale is examined. The results also suggest that materials with very dissimilar cutoff frequencies would yield a thermal conductivity which is closest to the lowest possible value for the given geometry.

Table of Contents

List of Tables

List of Figures

1. INTRODUCTION

1.1 Motivation

The past decade has brought about amazing advances in the field of micro/nanofabrication. Researchers have been able to create devices which have length scales of interest ranging from the nanometer scale and below [1–3] to 10s and 100s of microns [4–6]. As an example, in [3], a silicon nanowire with a diameter of 18 nm was used to create a field effect transistor (FET), the building block of modern computing. Ref. [5] describes a series of inter-digitated conductive cantilevers, or combs, which are used as tunable resonators. These cantilevers have a length of 30 μm, with gaps between features that can be as small as 1 μm. As well, a wide range of physics must be considered. For example, in [7] a Fabry-Perot cavity was fabricated using micron sized graphene sheets. In this device, a graphene sheet suspended above a silicon substrate was irradiated with continuous laser light. Radiation pressure, as well as thermal expansion, caused the sheet to vibrate. By changing the voltage across the graphene and the substrate, the frequency of the oscillation could be tuned. To fully model this device, photon-electron, electron-phonon, and phonon-phonon interactions must be considered, as well as the mechanical properties of graphene. Thermoelectric materials have also been of interest recently. These are materials which are able to generate electric current from an imposed temperature difference (or vice versa). Inherent in this phenomenon is the coupling between electrons and phonons. There are many other pertinent examples in which sub-continuum phenomena exist and are crucial to modern technology.

The ubiquitous need for fast information processing and massive information storage has led to the development of extremely small scale integrated circuit (IC) components. Gate lengths in metal oxide field effect transistors (MOSFETs) have reached 10 nm and are continuing to shrink. In the past decade, the diminishing IC component size has exacerbated issues with thermal management, which continues to be a central cause of device failure and a predictor of device performance [8]. On the length scales of interest for these IC's (10's to 100's of nm), the conduction of heat is dominated by quantized lattice vibrations called phonons [9,10]. Self-heating occurs when an electron is accelerated under a strong electric field. The accelerated electrons interact with the lattice atoms, creating phonons, which are quanta of lattice vibrations. These newly created phonons travel through the solid and scatter on other carriers, grain boundaries, defects and interfaces. Electron-phonon interaction, and the resulting sub-micron heat generation and dissipation mechanisms must be understood in order to design more reliable ultra-scaled microelectronics.

Another area in which sub-micron thermal transport is important is emerging microelectronics. Capacitive metal oxide semiconductor (CMOS) technology is reaching its theoretical limit [11]. To maintain Moore's law scaling, new materials which are compatible with existing CMOS technology are being developed. In particular, lower-dimensional materials such as graphene [12,13], carbon nano-ribbons [14,15], carbon nanotubes (CNTs) [16,17], and silicon and germanium nanowires (NWs) [3,18,19] have been the focus of much research. Because of the reduced dimension, a detailed description of phonon transport is even more necessary than their bulk counterparts.

Another strategy to maintain Moore's law is by creating 3D integrated circuits [11,20,21] which have a higher MOSFET density than traditional 2D integrated circuits. This is also thought to increase processing speed by reducing latency time because of shorter interconnects. However, this strategy drastically compounds the issue of thermal management, and an understanding of heat transfer at sub-micron scales becomes necessary.

Nanotechnologies for energy conversion are another area requiring improved knowledge of sub-micron thermal transport. Thermoelectric devices offer a very promising means to increase the efficiency of any cycle which produces waste heat, for example, in stationary power generation and automobile engines. In today's cars, 70% of the fuel energy is lost as waste heat, 35%-40% of which leaves through the exhaust pipe. A thermoelectric device working in a Chevy Suburban was shown to increase the fuel efficiency by approximately 5% [22]. Nationally, this increase in efficiency would results in a decrease of ~$25 billion dollars in fuel spending [23,24]. The efficiency of a thermoelectric device is governed by the dimensionless figure of merit $ZT=S^2\sigma T/k$ [25], where S is the Seebeck coefficient, σ the electrical conductivity, and T the operating temperature. Current work has focused on reducing the value of the total thermal conductivity, k, which is made up of an electronic contribution and a phononic contribution. Successful reductions have come from several strategies. Alloy scattering and interface scattering have been shown to produce the best results [26]. Understanding the details of phonon transport and scattering in thermoelectric materials is paramount in creating efficient thermoelectric devices.

Since the discovery of thermoelectricity in semiconductors in the 1950s and until recently, it was thought that the best way to reduce the conductivity of phonons was by using atomically heavy materials to slow the group velocity in tandem with alloy scattering to impede short wave length phonons. Particularly, PbTe, SiGe, and $Bi_2Te_3/Sb_2Te_3/Bi_2Se_3$ have been employed in thermoelectric applications [27]. Despite being researched for over 50 years, this class of materials has only been able to achieve a *ZT* of about 1.2. More recently a further reduction in the lattice conductivity was attained by introducing nanostructures [26,28–32]. In [26], a room temperature *ZT* of 2.4 was attained by using a Bi_2Te_3/Sb_2Te_3 superlattice which reduced the phonon thermal conductivity while not significantly reducing the electrical conductivity. Hsu *et al.* [32] achieved a *ZT* at 800 K of 2.4 using $Ag_nPb_mSb_nTe_{m+2n}$ materials and attributed the increase to the formation of nanodots of Ag and Pb inside a matrix of PbTe. These nanodots acted to scatter phonons and reduce thermal conductivity. Similar to this, in [29–31] nanoscructures were created by ball milling bulk materials and then fusing the resulting nanopowder. [29] used nanograins alone to obtain a peak *ZT* of 1.4 for BiSbTe bulk alloys, while [30,31] also used modulation doping to simultaneously increase the carrier mobility to achieve a peak *ZT* of ~1.2 for SiGe nanocomposites. From the above examples, it is clear that phonon scattering at interfaces is a crucial mechanism in reducing the phononic contribution in engineered nanostructured materials. For these reductions to occur, the distance between interfaces must be smaller than the dominant phonon mean free paths in the direction of heat transport. In order to effectively engineer

devices which utilize this mechanism, it is necessary to have the ability to simulate the details of phonon transport between and across interfaces.

Unfortunately, our fundamental understanding of the governing physics on such small scales is limited compared to our knowledge of continuum scale physics. Moreover, in many applications of engineering interest, for example, RF MEMS, microgears, microelectronics, and thermoelectrics, little is understood about the interaction of multiple physical models at these scales [33,34]. As such, our ability to create novel and reliable engineering devices is highly dependent on our ability to analyze and understand these physics and their coupled behavior.

It is known that predicting thermal behavior on length and time scales of these microsystems using Fourier's law yields erroneous results [35]. Thermal transport in semiconductors and dielectrics is due quantized lattice vibrations called phonons [9]. Depending on the length scale, phonons can exhibit particle-like behavior, or wave-like behavior with interference and coherence effects. Scientists and engineers have employed several strategies to model thermal behavior with varying success. These include atomistic models of thermal transport using molecular dynamics [36,37] and mesoscale models based on the Boltzmann transport equation [35,38]. Multiscale models integrating thermal behaviors across scales have also begun to appear [39]. The semi-classical Boltzmann transport equation (BTE) has been used to model phonon transport in semiconductors and dielectrics and is valid when the characteristic length of the domain is much larger than the phonon wavelength [35,40,41]. In this regime, wave effects may

be ignored and phonons can be viewed as semi-classical particles. Under this assumption, many of the devices discussed can be correctly modeled.

As such, the BTE has become a mainstay in device analysis. Although a particle viewpoint for carriers is valid, the computational complexity entailed therein can be prohibitive. Inter-particle scattering creates strongly coupled equations that cannot be solved using conventional methods, which numerically treat this coupling explicitly. Because of the explicit treatment of tightly coupled equations, convergence times for the sequential procedure when inter-particle scattering becomes important. This alone is enough to limit our simulation capabilities to simple scenarios which are far from reality. More damningly, frequency dependent behavior leads to added dimensionality. This effectively creates an additional phase space that must be resolved, increasing the number of discrete particles necessary for accurate simulation.

The devices discussed are far too intricate to rely on simplified modeling. Given that accurate modeling and simulation is paramount in effective and reliable design, it is vital that we develop a class of numerical methods capable of solving particle based transport equations; and in particular, the phonon BTE. The objective of this thesis is to develop an efficient computational technique to solve the phonon BTE. Our intent is to resolve phonon wave-vector dependence accurately, and to address complex geometries such as those occurring in nanoparticle composites. Furthermore, the computational technique must be able to exploit emerging high-performance computing platforms.

In the sections that follow, we provide an overview of past and current research in the area of phonon transport modeling and simulation, and present the specific goals of the thesis.

1.2 Lattice Dynamics

Thermal energy in a solid is propagated through atomic vibrations. These fluctuations, which are about an equilibrium position, can be grouped together to form traveling waves which traverse the solid, much like a sound wave propagates through air. This wave, called a phonon, travels with a predetermined velocity and frequency. The frequency and velocity are properties inherent to the crystal and are determined by the periodic arrangement of its constituent atoms, as well as their interacting potentials.

To deduce the allowed frequencies of a periodic arrangement of atoms, we assume that all atoms in the solid are connected to each other by a linear spring. The spring constant is the second derivative of the total crystal energy with respect to the atomic displacements, shown as:

$$\phi_{\alpha\beta}^{l(i)n(j)} = -\frac{\partial^2 U}{\partial u_{\alpha,l(i)} \partial u_{\beta,n(j)}} \tag{1}$$

Above, ϕ is the spring constant, U is the total crystal energy between the l^{th} atom in the i^{th} unit cell and the n^{th} atom in the j^{th} unit cell, and u is the atomic displacement. The subscripts of ϕ, α and β, denote the direction of the atomic displacement, making ϕ a second order tensor. Using Newton's second law, we can write an equation relating the force on an atom to the displacement of the surrounding atoms:

$$m\ddot{u}_{\alpha,l(0)} = \sum_{i,n} \sum_{\beta=x,y,z} \phi_{\alpha\beta}^{l(0)n(i)} u_{\beta,n(i)} \tag{2}$$

This is the force acting on the reference atom, *l(0)*, in the α direction. The first summation is over all atoms in all unit cells, and the second atom is over all directions, *x*, *y*, *z*. If we assume a plane wave solution to Eq. (2), then the displacement can be written as:

$$\omega^2(\boldsymbol{K})\varepsilon_{\alpha,l}(\boldsymbol{K}) = \sum_{n,\beta} \sqrt{m_l m_n} \sum_i \phi_{\alpha\beta}^{l(0)n(i)} \exp\left[-i(\boldsymbol{K}\cdot\boldsymbol{R}_i - \omega t)\right] \varepsilon_{\beta,n}(\boldsymbol{K}) \tag{3}$$

This equation can be solved for the phonon frequency, ω, as a function of the phonon wave vector, $\boldsymbol{K}$. The resulting solution is called the dispersion relation (Fig. (1)). A phonon is a group of vibrations which form a travelling wave, the velocity of which is the gradient of the dispersion relation with respect to the wave vector. The wave vector is proportional to the inverse of the phonon wave length, and has units of m^{-1}. A phonon's momentum is defined as $\hbar\boldsymbol{K}$, where $\hbar$ is the reduced Planck's constant. Since there is finite spacing between atoms, there only exists a finite extent of the wave vector space which is unique, called the first Brillouin zone. For every point, $\boldsymbol{K}$, inside the first Brillouin zone there may exist several different polarizations and modes, each vibrating at (usually) different energies. Different polarizations arise from atoms having different degrees of freedom for vibration, whereas different modes arise from multiple basis atoms. Each type of phonon has its own branch of the dispersion relation, which can be seen in Fig. (1).

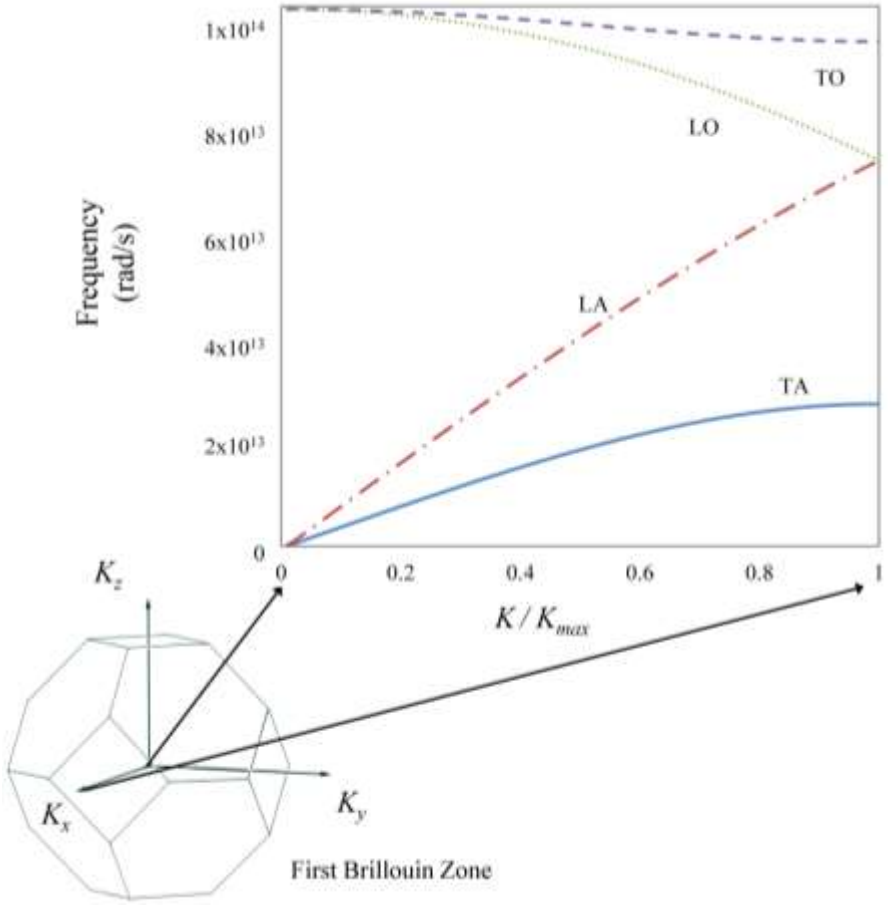

Figure 1: Dispersion relation for silicon in a the [100] direction found using [42]

1.3 The Boltzmann Transport Equation (BTE)

In this thesis, we will focus on solving the energy moment of the phonon BTE:

$$\frac{\partial e''}{\partial t} + \boldsymbol{v} \cdot \nabla_{\boldsymbol{x}} e'' = \dot{E}_I + \dot{E}_{II} \qquad (4)$$
$$e = \hbar \omega f$$

Here, *e''* is the non-equilibrium energy density of the phonon at wave vector ***K***, polarization ε, and position ***x***. $\hbar$ is the reduced Planck's constant, which multiplies the

phonon frequency, ω, to make the phonon energy. The phonon energy is multiplied by the occupation probability, *f*. The dominant phonon scattering events involve three phonons, as shown on the RHS of Eq. (4). The first term, $\dot{E}_I$, represents type I collisions whereby the phonon of interest at polarization ε interacts with a phonon of polarization ε' to form a third phonon of polarization ε'' (and the reverse process). Energy generated by type II collisions, $\dot{E}_{II}$, is represented by the second term which is when the phonon of interest at polarization ε decomposes into two phonons of polarization ε' and ε'' (and the reverse process). In this form, scattering involves large summations over the entire wave vector space which are very expensive [43]. A common simplification to the full scattering term is to use the single mode relaxation time (SMRT) approximation [9,44]. In this, it is assumed that a single phonon mode is perturbed from equilibrium and follows an exponential decay back to equilibrium. The characteristic time at which the phonon decays is called the relaxation time. The SMRT approximation is shown below:

$$\left(\frac{\partial e''}{\partial t}\right)_{scattering} = \frac{e^0 - e''}{\tau}$$
$$e^0 = \hbar\omega\left[\exp\left(\hbar\omega \big/ k_B T\right) - 1\right]^{-1} \tag{5}$$

where τ is the relaxation time and e^0 is the Bose-Einstein distribution function at lattice temperature *T*, multiplied by the phonon energy $\hbar\omega$. k_B is Boltzmann's constant. Under this approximation, each phonon communicates with the lattice temperature (through the equilibrium energy density), which creates an indirect coupling among all phonons. The main limitation of this approximation lies in its inability to account for collisions which

are momentum conserving (Normal processes). Since these collisions do not directly impede heat flow, a relaxation time which includes Normal processes will under predict the conductivity at low temperatures, say 5 K for silicon, when these processes are important. For most three dimensional materials at near room temperature, the effect of Normal processes is small and the SMRT approximation agrees relatively well with experiment. Klemens in [44] was able to derive an expression for the thermal conductivity of quartz at low temperatures and made the first attempt to separately consider the contribution of longitudinal and transverse phonons. In [45], Callaway found expressions for the conductivity which included the effects of momentum conserving collisions (Normal) and momentum destroying collisions (Umklapp). Holland further employed the SMRT approximation to obtain an expression for the bulk thermal conductivity of a silicon and germanium [46]. Because of several approximations in these models, fitted parameters were necessary to match thermal conductivity data.

To move away from using fitted parameters, other methods for determining the relaxation time for different phonon groups have been developed. Fermi's Golden Rule may be used to calculate the transition probability per unit time of quantum interactions [47]. This method couples the initial and final density of states through a perturbing potential. Single mode relaxation times may be calculated by summing over all possible three-phonon collisions for a particular phonon. The total transition probability per unit time can be thought of as a relaxation time [43]. However, using this method includes in

the transition probability Normal scattering processes, which do not contribute to thermal resistance. Therefore, caution must be used when this relaxation time is calculated.

In [48], Ladd *et al.* used molecular dynamics simulations to simulate heat transfer in solid argon for a range of temperatures above the Debye temperature of 6 K. The temporal decay of the potential energy autocorrelation function was then to calculate the relaxation time and used to calculate the thermal conductivity. Later, McGaughey and Kaviany [49] improved upon this method by finding the autocorrelation of the total energy of solid argon, which included the kinetic energy. Henry and Chen [50] used this same technique to calculate the relaxation times in silicon. One of the benefits of this method was exemplified when applied by Thomas *et al.* [51] to examine the thermal conductivity of carbon nanotubes. MD simulations include all orders of anharmonicity, not just the first anharmonic term (third order derivative of the total crystal energy). When comparing to thermal conductivity calculations that only include up to the third order derivative (Fermi's Golden Rule), significant differences were discovered at higher temperatures.

1.4 Phonon Transport at Interfaces

Kapitza first encountered a temperature jump between dissimilar materials in 1941 when he submerged a solid in liquid helium. As seen from the point of view of a phonon as a particle, the abrupt change in materials has two effects: the phonon may incur scattering due to surface roughness at the interface, and the phonon will be affected by the difference in material properties of its new medium. Khalatnikov [52] and Little [53] developed the acoustic mismatch model (AMM) to explain the cause of this

temperature jump by considering the mismatch in sound velocity in the two media. They adopted a harmonic model in which a phonon encounters a geometrically perfect interface, and all transmission/reflection happens elastically. With these assumptions, the transmission and reflection coefficients can be determined by the angle of the incident phonon and the acoustic velocities of the phonon on either side of the interface. Schelling, Phillpot, and Keblinski [54] performed a MD simulation between silicon and a fictitious material which was exactly the same as silicon, except it had four times the atomic mass. The simulation created a single wave packet in silicon belonging to a specific polarization and wave vector which was allowed to propagate across the interface. From there, transmission coefficients could be calculated. The found that for low frequency acoustic phonons, the AMM matches the MD simulations well, but for high frequency phonons the AMM was incorrect. Swartz and Pohl [55] postulated that at high enough temperatures and with sufficient interface roughness, the effects of the acoustic mismatch are small and the dominant mechanism governing interface transmission is the relative density of states of the two materials. Because the interface is assumed rough, a phonon which encounters the interface is either transmitted or reflected in a (still elastic) diffuse manner. A crucial assumption in the formulation was that the transmission coefficient of a phonon across the interface is equal to the reflection coefficient of a phonon traveling in the opposite direction. This meant that a phonon "lost its memory" once the interface was encountered. This model was later termed the diffuse mismatch model (DMM). The accuracy of the DMM has a large variability depending on the mismatch in the Debye temperature of the materials, among other factors [56–59]. The mismatch in Debye temperatures implies a large difference in the maximum frequency in the two materials. Errors in the DMM arise because of its elastic transmission assumption. For materials which have a large Debye mismatch, the thermal

conductance was found to be much larger than that calculated by the DMM. This implies the presence of inelastic scattering channels. The atomistic Green's function (AGF) has also recently been applied to interfacial phonon transport [60–64]. This method ignores anharmonicity and takes a quantum mechanical approach to the transport of energy across an interface. This is done by decomposing the system into different sub-sections- the device and the two contacts - and calculating the Green's function of the sub-sections. With the three different Green's functions, it is possible to simulation the systems response to a wave packet travelling through the system.

1.5 Numerical Simulations of Phonon Transport

LINEARIZED BTE

A commonly-used technique for computing thermal conductivity of bulk materials is the linearized BTE. The linearized BTE is valid for small temperature differences, which allows us to assume transport is proportional to the thermal gradient. Arriving at the linearized form comes from two main assumptions. First, the convective term is assumed proportional to the temperature gradient. Second, the perturbation from equilibrium is assumed to be proportional to the magnitude and direction of the temperature gradient. Using these two assumptions, it is possible to arrive at a linear system which can be solved iteratively. Lattice dynamical equations (Eq. (3)) are used for calculating the dispersion relation and the group velocity of the phonon modes. Fermi's Golden Rule is then used to calculate the transition probabilities for the three-phonon collisions [43]. In [65] and [66], Omini and Sparavigna introduced the solution to the linearized BTE to calculate the thermal conductivity of solid argon and krypton. Interatomic force constants were taken from empirical relations and the consequence of such choices was examined in [67]. Of particular importance in the choice of the

interatomic potential is the calculation of the dispersion relation. The three potentials considered in [67] over-predicted the frequencies of the transverse acoustic modes and their group velocities, which lead to an over-prediction of the thermal conductivity when phonon-phonon scattering was the dominant scattering mechanism. Sparavigna later used this same technique to evaluate the importance of isotope scattering in diamond in [68], and the conductivity of silicon carbide in [69]. Broido and Reinecke [70] adapted the method to predict the thermal conductivity of superlattice structures of silicon and germanium, and later this was also used by Ward and Broido [71] on silicon/germanium and GaAs/AlAs nanostructures. More recently, the use of empirical interatomic potentials was eliminated and replaced with density functional perturbation theory by Broido, et al. [72]. This removed the need for any fitting parameters in the calculation and yielded predictions of thermal conductivity which were within 5% of the experimentally-measured room temperature thermal conductivity of diamond. This same strategy was then used to calculate the thermal conductivity of silicon and germanium [73] and again of diamond [74]. Since its introduction, the linearized BTE has been used to examine more complex systems such as lower dimensional materials (graphene) [75,76] and alloys [77].

MONTE CARLO SIMULATION

Given that the BTE is a model for the stochastic behavior of particles, a very intuitive way to solve the BTE is through a Monte Carlo (MC) method. Mazumder and Majumdar [78] first introduced the solution of the phonon BTE by MC. Their method accounted for part of the phonon dispersion and separated the phonon spectrum into discrete frequency bins. The spatial domain was also separated into discrete bins. To initialize the simulation, a local temperature is chosen at each spatial bin. The amount,

frequency, wave vector, and polarization of phonon meta-particles inside each spatial bin are randomly chosen based on the Bose-Einstein distribution at the given temperature. An iteration consists of two decoupled steps: convection and collision. The convective step moves all the phonons to different spatial bins, which changes the temperature and total energy at each spatial bin. During the collision step, the temperature and energy at each spatial bin are recalculated and stored. Then phonons are selected to participate in a collision based on the time step and the characteristic collision times. If a phonon is selected to collide, its frequency, polarization, and wave vector are changed randomly according to the temperature which was calculated in the beginning of the collision process. After all phonon collisions have been calculated, energy conservation is explicitly enforced by adding and/or removing phonons from each cell based on the equilibrium distribution at the cell temperature. The subtraction/addition continues until the post-collision energy matches the pre-collision energy. With this collision scheme, the underlying model for phonon scattering is the relaxation time approximation. Hence, any shortcomings the relaxation time approximation has, this method does as well.

Since the publication of [78], several improvements/variations have appeared in the literature. Lacroix et al. [79] applied the phonon MC to transient heat conduction in silicon and germanium. Chen et al. [80] used a genetic algorithm to treat energy and momentum conservation when they used the phonon MC method for predicting the thermal conductivity of silicon nanowires. In [81], Jeng and coworkers included interface transmission coefficients to predict the thermal conductivity of nanoparticle composites. Mittal and Mazumder [82] modified the original simulation with the

inclusion of optical phonons. Hamzeh and Aniel [83] applied the same MC procedure to a spatially uniform relaxation of hot zone center phonons in III-V compounds.

In contrast to Mazumder and Majumdar's initial solution method, Randrianalisoa and Baillis [84] proposed an alternative procedure for solving the steady state phonon BTE. In all other methods discussed, the state of the system was initialized and time was incremented until a steady state solution was achieved. However, this method achieves convergence by adjusting the temperature of each volumetric cell to balance the creation/destruction and flux of phonons. This method was shown to be much more efficient that the previously proposed methods.

In [85], Pascual-Gutierrez and co-workers developed a Monte Carlo method which explicitly included three phonon scattering events. The computational process was performed in the same way as [78], where an iteration is divided into a collision and a convection step. The difference between the two methods lies in the collision step. Transition probabilities were calculated using Fermi's Golden Rule for each of the possible three-phonon processes. To rectify the short comings of the relaxation time approximation, only events which satisfied energy and momentum conservation were chosen.

Regardless of the strategy used for phonon MC, there is always an increase in computational effort with a decrease in Knudsen number. This is due to an increase in phonon collisions which drives the allowed time step to smaller and smaller values. The time step must be small enough so that for each streaming step, the probability of phonon collision is small, otherwise it would not be accurate to separate the two processes. Thus,

when the required time step is very small, convergence to steady state requires a large number of computational steps to achieve.

Recently, however, Péraud and Hadjiconstantinou [86,87] developed a variance reduction method to significantly reduce the computational effort needed for the MC solution of the phonon BTE for near equilibrium problems. This was accomplished by only tracking particles which deviated from equilibrium. The equilibrium value was chosen for the entire domain and used as a reference. Because all phonons in the domain are very near equilibrium, this reduced the number of particles necessary for accurate simulation.

MOLECULAR DYNAMICS SIMULATION

For systems which are small enough, of the order of a micron or smaller, molecular dynamics (MD) can be used to simulate thermal transport. MD simulations are essentially a time integration of Newton's second law on the atomic level. Each atom is treated as a point particle which interacts with other particles through an interaction potential. To find the interaction potential, empirical models are used which are generally devised to fit specific bulk data [42,88–90]. However, increasingly, force constants based on density functional theory are being used [91]. The trajectory of every atom is calculated for a set of discrete time steps typically spanning nanoseconds. These data can be analyzed and transport parameters such as thermal conductivity may be extracted.

To calculate thermal conductivity, one of two methods is adopted: equilibrium molecular dynamics (EMD) [92] or non-equilibrium molecular dynamics (NEMD) [93]. In EMD, the system is initialized in a state which is non-equilibrium and is allowed to

relax down to equilibrium. The rate of this relaxation is related to the thermal conductivity. In contrast, NEMD imposes a heat flux and calculates a temperature gradient and the thermal conductivity is computed as the ratio of the two. A study comparing the two methods found them to be consistent with each other and in reasonable agreement with experiment [94]. Though MD simulations account for anharmonicity to all orders, the classical nature of the implementation makes it difficult to include quantum effects. Thus, simulations below the Debye temperature are suspect and must be used with caution.

MD simulations can also be used to calculate phonon properties. In [51], Thomas *et al.* developed a method for calculating the dispersion relation and lifetimes of phonons using the spectral energy density and applied it to carbon nanotubes. This method is particularly useful because it reduces the computation time of a typical NEMD simulation to extract the thermal conductivity. In [95], Goicochea et al. used MD simulations as the basis for predicting thermal transport in electronic devices. A quantum correction was then used to correct the MD calculations. These were then used in the Boltzmann transport equation to model the heat flow in the devices. This so-called hierarchical modeling was also used in [96].

MD has many advantages. Because of the simplicity of the simulation, the only inputs necessary are the interatomic potentials and the initial position of the atoms. The evolution of the system is straight forward and lends itself to large scale computing platforms. The main limitations of MD are either in the physics of the simulation, or in the computational requirement. The neglect of quantum effects makes MD simulations invalid below the Debye temperature. For silicon, the Debye temperature is 660 K, while for graphene it is around 2300 K. Thus, all room-temperature predictions in these materials are suspect. Also, the behavior of the surrounding electrons is treated in an

inexact way and may not always be useful. With current computing power, practical problems are difficult to address using MD because of the large number of atoms needed for domain sizes of interest.

DETERMINISTIC SIMULATIONS OF THE BOLTZMANN TRANSPORT EQUATION

In contrast to the Monte Carlo techniques described above, a variety of deterministic solution techniques have been published in the literature [38,40,97,98]. These are typically based on solution techniques used in the thermal radiation literature [99,100]. In a typical scheme, the physical domain is discretized into control volumes. In keeping with the finite volume idea, the Brillouin zone is also discretized into finite volumes, though discrete ordinates approaches have been used as well [38,40,97]. Discrete equations for each physical and $\boldsymbol{K}$-space control volume are developed by imposing energy balances. Most published work has been based on the relaxation time approximation to the scattering term.

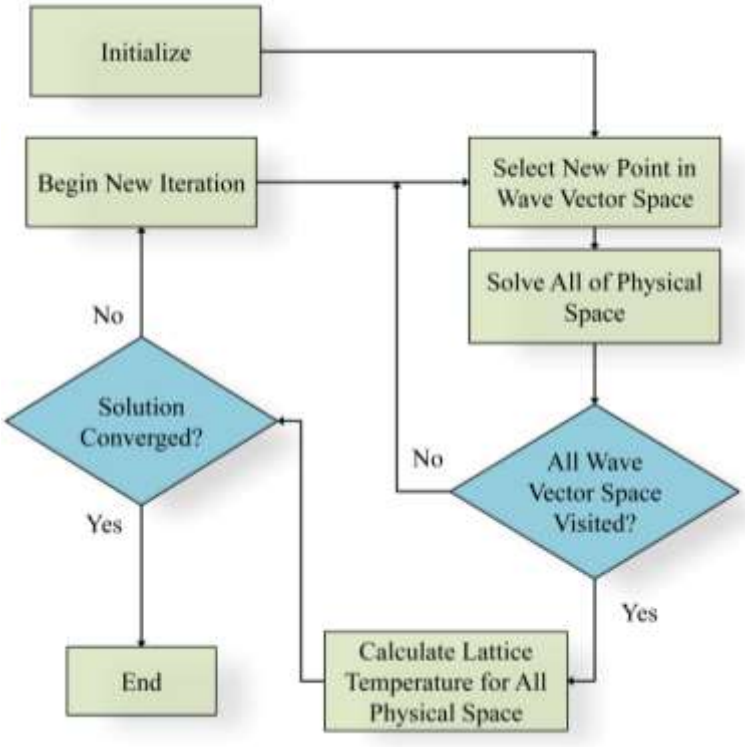

Figure 2: Flow chart for the sequential solution procedure.

Once both the spatial and wave vector domain have been discretized, a single control volume in wave vector space is chosen and the entire physical space is solved using prevailing values for the equilibrium energy density. The next volume in wave vector space is then chosen and the spatial domain is solved. This procedure is repeated until the entire volume of wave vector space has been visited. The lattice temperature is then updated and the convergence is checked.

The sequential procedure suffers from slow convergence when the phonon mean free path is much small than the length of the domain. This occurs because of the increased amount of phonon-phonon scattering which can tightly couple the discrete

equations. For this reason, simulations using realistic representations of phonon properties are currently out of reach. More detail about this coupling is discussed in a later chapter.

1.6 Aims and Scope of this Dissertation

The objective of this thesis is to develop an efficient computational procedure for the solution of the ***K***-resolved phonon Boltzmann transport equation for arbitrary geometries, and to demonstrate its applicability for computing thermal transport in complex composite materials. An important goal is to address the difficulties in convergence that conventional sequential solution techniques encounter, especially when applied to materials such as silicon, which exhibit a 3-4 order magnitude in mean free path, or when applications with heterogeneous interfaces are simulated. The specific aims of the thesis are listed below.

- The numerical procedure, named the coupled ordinates method (COMET), will be developed. This method treats phonon-phonon coupling implicitly to mitigate convergence problems at low Knudsen number. Spatial coupling is enhanced with the use of a geometric multigrid.
- COMET will be benchmarked against a sequential solution procedure for a wide range of Knudsen numbers to characterize the improvement.
- COMET will be parallelized using domain decomposition. COMET's performance on multiple cores is examined, and is shown to be highly scalable.
- COMET will be extended to include phonon transport across interfaces. It will be shown that the sequential procedure suffers from slow convergence when interfaces are present, whereas COMET is shown to perform well.

- The performance of COMET will be explored on single and multiprocessor processor platforms.
- The utility of COMET will be demonstrated by using the solution procedure to compute phonon transport in realistic silicon/germanium particulate composites and obtain frequency dependent heat transfer.

Chapter 2 presents the Boltzmann transport equation and reviews the treatment of boundary and interface conditions. The discretization of the BTE using the finite volume method is then discussed, and the relevant dimensionless parameters are identified. Chapter 3 develops the solution procedure for solving the discrete equation set. It presents detailed comparisons between the performance of the conventional sequential solution procedure and COMET. Parallel scaling of COMET is also explored. In Chapter 4, the COMET procedure is extended to include phonon transport across interfaces. The performance of COMET is compared with that of the sequential solution procedure for problems involving heterogeneous material interfaces. Nuances of the implementation needed to achieve optimal performance are highlighted. The utility of COMET is then demonstrated in Chapter 5 where we explore phonon transport in nanoparticle composites. Realistic particle composite geometries are constructed from X-ray CT scans, and meshed using arbitrary unstructured meshes. Composite thermal conductivity is calculated as a function of temperature for a wide temperature range. The spectral composition of the heat flux through the composite is determined, and the underlying physics are discussed. Finally, Chapter 6 summarizes the main results of the thesis and suggests future work in the area of simulating phonon transport.

2. THE PHONON BTE

In this chapter, we will discuss in great detail the BTE and its numerical solution. This will include the formulation of the boundary and interface conditions, followed by the discretization using the finite volume method [40,99,101]. We will then non-dimensionalize the BTE and identify the relevant dimensionless groups. Coupling within the discrete equations are discussed briefly to motivate Chapter 3, where the new solution method is proposed.

2.1 Structure

When phase coherence effects can be ignored, the semi-classical Boltzmann transport equation (BTE) may be used to describe conduction heat transfer in semi-conductors and dielectrics. In this view, phonons may be treated as notional particles with position $\boldsymbol{x}$ and crystal momentum $\boldsymbol{p}$. In Hamiltonian mechanics, we wish to determine the position and momentum of every particle in a system. It would be ideal to calculate the momentum and position of every particle in a given system, but this is not possible computationally for practical problems. The Boltzmann transport equation (BTE) [102] circumvents the problem of tracking *every particle's* position and momentum by tracking the *probability* of finding a particle at a particular position and with a particular momentum. Perhaps more clearly, this can be thought of as calculating the number density of a particular type of particle. We can track this density, which is a function of three-dimensional position and three-dimensional momentum, yielding a six-dimensional equation [9,10,25]:

$$\frac{\partial f}{\partial t} + \boldsymbol{v} \cdot \nabla_{\boldsymbol{x}} f + \boldsymbol{F} \cdot \nabla_{\boldsymbol{p}} f = \left(\frac{\partial f}{\partial t} \right)_{scattering} \tag{6}$$

Here, $f=f(t, \boldsymbol{x}, \boldsymbol{p})$ is the number density of a particle at position $\boldsymbol{x}$, with momentum $\boldsymbol{p}$, at time t and has units of number (dimensionless) per unit physical space volume (m^3), per unit momentum space volume $\left(kg \cdot m/s \right)^3$. The first term on the left hand side (LHS) of Eq. (6) is the unsteady term which accounts for the accumulation of particles. The second term is responsible for convecting particles through physical space at velocity, $\boldsymbol{v}(\boldsymbol{p})$, which is a function of only momentum. The third term on the LHS of Eq. (6) reflects changes in the number density due to an external force, $\boldsymbol{F}$, acting on the particle. The dot product of the external force with the momentum space gradient, ∇_p, means that the applied force seeks to increase the momentum of each particle in the direction of the applied force. The term on the right hand side (RHS) of Eq. (6) is the change of the number density due to any scattering event that a particle may encounter. Equation (6) is the BTE in its most general form. Modifications can be made to use the BTE for tracking specific particles by specifying the details of the scattering kernel.

The steady state phonon BTE is shown below [9]:

$$\nabla_{\boldsymbol{x}} \cdot \left(\boldsymbol{v} e''_p \left(\boldsymbol{x}, \boldsymbol{K} \right) \right) = \left(\frac{\partial e''_p \left(\boldsymbol{x}, \boldsymbol{K} \right)}{\partial t} \right)_{scattering} \tag{7}$$

$$e'' = \hbar \omega f''$$

where $\boldsymbol{v}$ is the phonon group velocity, *e"* is the non-equilibrium phonon energy density which is dependent on the polarization *p*, the spatial location, $\boldsymbol{x}$, and the wave vector, $\boldsymbol{K}$. The convective term on the left hand side is responsible for phonon free flight while the scattering term on the right hand side is responsible for energy exchange between phonon groups due to inter-phonon and phonon-carrier collisions. In its most complete form, this term couples every phonon's energy density directly to that of every other phonon, providing conservation rules are satisfied [43]. The phonon BTE in its full scattering form is shown below [47]:

$$\frac{\partial e''}{\partial t} + \boldsymbol{v} \cdot \nabla_{\boldsymbol{x}} e'' = \dot{E}_I + \dot{E}_{II} \tag{8}$$

Here, *e"* is the non-equilibrium energy density of the phonon at wave vector $\boldsymbol{K}$, polarization ε, and position $\boldsymbol{x}$. $\hbar$ is the reduced Planck's constant, and $\hbar\omega$ is the phonon energy associated with a phonon of frequency ω. For computation of thermal conductivity, the dominant phonon scattering mechanism is three phonon scattering [47], which is shown on the RHS of Eq. (8). The first term represents type I collisions whereby the phonon of interest at polarization ε interacts with a different phonon of polarization ε' to form a third phonon of polarization ε'' (and the reverse process). To calculate the total energy source from type I phonon interactions, an integration over all possible collisions is performed, as such [43]:

$$\dot{E}_I = \frac{\Omega\omega}{4\hbar\pi^2} \int f f' \left(f'' + 1 \right) \left| \Phi_{\boldsymbol{K},\boldsymbol{K}' \to \boldsymbol{K}''} \right|^2 \left| \boldsymbol{v}'_n \right|^{-1} dS_{\boldsymbol{K}'} \tag{9}$$

In this equation, f is the number density of the phonon in question, and f' and f'' are the number density of the two other participating phonons in the three phonon interaction. Φ is the matrix element taken from Fermi's Golden Rule which couples the three states via the third order derivative in the total crystal energy. Within the matrix element is the conservation of quasi-momentum, whereby Φ is zero if it is not. The velocity $\boldsymbol{v}_n' = \nabla_{\boldsymbol{K}''}\omega'' - \nabla_{\boldsymbol{K}'}\omega'$ is the difference in the group velocity of the other two interacting phonons. This integration is performed over the surface, $S_{\boldsymbol{K}'}$, in $\boldsymbol{K}$-space which satisfies energy conservation, $\omega+\omega'= \omega''$. Here, Ω is the volume of the Wigner-Seitz cell. A similar expression can be written for Type II collisions, which is the second term on the RHS. These occur when the phonon of interest at polarization ε decomposes into two phonons of polarization ε' and ε'' (and the reverse process):

$$\dot{E}_{II} = \frac{\Omega\omega}{4\hbar\pi^2}\int (f+1)(f'+1)f''\left|\Phi_{\boldsymbol{K}''\to\boldsymbol{K}',\boldsymbol{K}}\right|^2 \left|\boldsymbol{v}_n''\right|^{-1} dS_{\boldsymbol{K}''} \tag{10}$$

In this form, scattering involves large summations over the entire wave vector space which are very expensive [43]. A common simplification to the full scattering term is to use the single mode relaxation time (SMRT) approximation [9,44]. In this, it is assumed that a single phonon mode is perturbed from equilibrium and follows an exponential decay back to equilibrium. The characteristic time at which the phonon decays is called the relaxation time. The SMRT approximation is shown below:

$$\left(\frac{\partial e''}{\partial t}\right)_{scattering} = \frac{e^0 - e''}{\tau}$$
$$e^0 = \hbar\omega\left[\exp\left(\hbar\omega \big/ k_B T\right) - 1\right]^{-1} \tag{11}$$

where τ is the relaxation time and e^0 is the Bose-Einstein distribution function at temperature T, multiplied by the phonon energy. k_B is Boltzmann's constant. Holland was able to use the SMRT approximation to derive an expression for the bulk thermal conductivity of a crystal [46]. Assuming specific functional forms for the relaxation time based on theoretical considerations, it is possible to create curve fits for the relaxation time which match with experimental data. The relaxation time may also be calculated from molecular dynamics [50] and Fermi's Golden Rule [43].

BOUNDARY CONDITIONS

Two types of boundary conditions are considered in this paper: given-temperature and reflecting. Given-temperature boundaries are treated as diffusely emitting and completely absorbing. For a phonon whose group velocity vector points from the boundary into the domain, the boundary value is taken to be the equilibrium energy density at the boundary temperature. For a phonon whose group velocity vector points from the interior of the domain to the boundary, the phonon is assumed to be traveling ballistically out of the domain at the domain boundary. The given-temperature boundary condition may thus be written as

$$
\begin{aligned}
e''_{\boldsymbol{v}\cdot\boldsymbol{n}<0}\left(\boldsymbol{x}_b\right) &= e^0\left(T_{wall}\left(\boldsymbol{x}_b\right)\right) \\
e''_{\boldsymbol{v}\cdot\boldsymbol{n}>0}\left(\boldsymbol{x}_b\right) &= e''_{\boldsymbol{v}\cdot\boldsymbol{n}>0}\left(\boldsymbol{x}_b^-\right)
\end{aligned}
\tag{12}
$$

Here, $\boldsymbol{x}_b$ is the spatial location on the boundary, $\boldsymbol{n}$ is the outward pointing normal of the boundary, and $\boldsymbol{x}_b^-$ is a location in the domain interior just upwind of the boundary.

Reflecting boundaries may be either fully specular, fully diffuse, or partially specular/diffuse. A specular reflection is a mirror reflection, whereby all the energy of a phonon incident to the wall is reflected into a phonon with the same tangential wave vector component, but opposite normal wave vector component. On the other hand, a diffuse reflection requires that all energy of all phonons incident to the wall is returned equally to all out-going phonons. The reflecting boundary condition may be written as:

$$
\begin{aligned}
e''_{\boldsymbol{v}\cdot\boldsymbol{n}<0}\left(\boldsymbol{x}_b\right) &= p e''\left(\boldsymbol{x}_b^-, \boldsymbol{K}_{spec}\right) + \left(1-p\right) e^0\left(T_{diffuse}\right) \\
\boldsymbol{K}_{spec} &= \boldsymbol{K} - 2\left(\boldsymbol{K}\cdot\boldsymbol{n}\right)\boldsymbol{n} \\
e^0\left(T_{diffuse}\right) &= \frac{\hbar\omega}{\exp\left(\dfrac{\hbar\omega}{k_B T_{diffuse}}\right)-1}
\end{aligned}
\tag{13}
$$

where p is the specularity of the wall, a number between zero and one; a value of unity signals a perfectly specular wall. $\boldsymbol{K}_{spec}$ is the specular direction corresponding to the $\boldsymbol{K}$ vector of interest. $e^0(T_{diffuse})$ is the equilibrium distribution function at the equilibrium temperature corresponding to the incoming energy. The temperature, $T_{diffuse}$, is found through a non-linear solution of the following conservation equation:

$$\int_{\mathbf{v}\cdot\mathbf{n}<0} e^0\left(T_{diffuse}\right)\mathbf{v}\cdot\mathbf{n}d^3\mathbf{K} = \int_{\mathbf{v}\cdot\mathbf{n}>0} e'\mathbf{v}\cdot\mathbf{n}d^3\mathbf{K} \tag{14}$$

INTERFACE CONDITION

In this thesis it is assumed that phonon scattering at the interface is elastic and that the surface is rough enough to cause diffuse reflection and transmission. Under these assumptions, a phonon transmitted across the interface transfers energy to phonon of any wave vector and polarization with the same frequency. In addition, the group velocity vector must point into the material into which the phonon is being transmitted. The same assumptions govern reflection as well. Using these stipulations, we seek to determine the transmission and reflection coefficients for both materials.

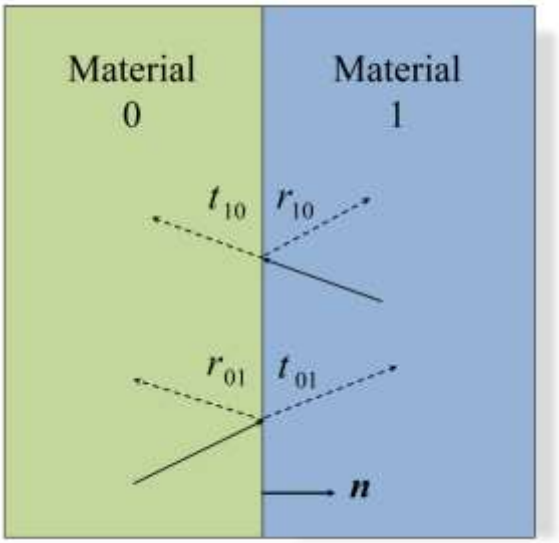

Figure 3: Transmissivity and reflectivity at a multi-material interface.

Following the convention in Fig. (3), we may write the following expressions for the transmissivity and reflectivity at the interface:

$$t_{01}(\omega)+r_{01}(\omega)=1 \tag{15}$$

$$t_{10}(\omega)+r_{10}(\omega)=1 \tag{16}$$

$$\left[\int_{\boldsymbol{v}\cdot\boldsymbol{n}>0} t_{01}(\omega)e^{0}(\omega,T)\boldsymbol{v}\cdot\boldsymbol{n}\delta(\omega)d^{3}\boldsymbol{K}\right]_{0} = -\left[\int_{\boldsymbol{v}\cdot\boldsymbol{n}<0} t_{10}(\omega)e^{0}(\omega,T)\boldsymbol{v}\cdot\boldsymbol{n}\delta(\omega)d^{3}\boldsymbol{K}\right]_{1} \tag{17}$$

Here, the subscript represents the direction of the incoming phonon. That is, t_{01} is the transmissivity of a phonon which is traveling from material 0 and being transmitted into material 1. Conversely, r_{10} is the reflectivity of a phonon which is traveling in material 1 and being reflected off material 0. Equations (15) and (16) result from the conservation of energy at the interface resulting from elastic interactions. Equation (17) results from enforcing detailed balance for phonons of frequency ω; this is accounted for by the Dirac delta function, $\delta(\omega)$ in Eq. (17). Since there are four unknowns, we must find one more relationship in order to determine the transmissivity and reflectivity. The final relationship is obtained from a model for the transmission process. A number of models have been published in the literature, including the diffuse mismatch model (DMM) [55], transmission coefficients using the atomistic Green's function (AGF) approach [60,61], or those obtained from molecular dynamics (MD).

In this thesis we use the DMM as the fourth relation in determining the transmissivity and reflectivity:

$$t_{01}(\omega) = r_{10}(\omega);\ t_{10}(\omega) = r_{01}(\omega) \tag{18}$$

Using Eqs. (17) and (18), we may solve for the transmissivity to obtain:

$$t_{01}(\omega) = \frac{-\left[\int_{\boldsymbol{v}\cdot\boldsymbol{n}<0} e^0(\omega,T)\boldsymbol{v}\cdot\boldsymbol{n}\delta(\omega)d^3\boldsymbol{K}\right]_1}{\left[\int_{\boldsymbol{v}\cdot\boldsymbol{n}>0} e^0(\omega,T)\boldsymbol{v}\cdot\boldsymbol{n}\delta(\omega)d^3\boldsymbol{K}\right]_0 - \left[\int_{\boldsymbol{v}\cdot\boldsymbol{n}<0} e^0(\omega,T)\boldsymbol{v}\cdot\boldsymbol{n}\delta(\omega)d^3\boldsymbol{K}\right]_1} \tag{19}$$

Using Eq. (19) it is possible to find the other three coefficients. In Eq. (19), the system is assumed to be in equilibrium which implies that the values of the equilibrium energy density at equal frequencies are the same, and may be cancelled out. This leads to an equation for the transmissivity which is dependent only on the dispersion relation of the two materials.

2.2 Discretization

The BTE is discretized using a standard finite volume procedure which is explained in previous publications [40,99,101]. It is briefly explained here for completeness. The physical domain is discretized into arbitrary unstructured convex polyhedra; the wave-vector space is also discretized into arbitrary control volumes. A schematic of the control volume in the physical and wave vector spaces is shown in Figs.

(4) and (5), respectively. We first integrate the BTE over both the physical and wave-vector control volumes (Eq. (20)) and apply the divergence theorem and discretize:

$$\int_{\Delta^3 \boldsymbol{K}} \int_{\Delta V} \left[\boldsymbol{v} \cdot \nabla_x e'' = \frac{e^0 - e''}{\tau_{eff}} \right] dV d^3\boldsymbol{K} \tag{20}$$

$$\sum_f e_f'' \boldsymbol{v} \cdot \Delta \boldsymbol{A}_f = \frac{e_c^0 - e_c''}{\tau_{eff}} \Delta V \tag{21}$$

$$\sum_{\boldsymbol{v} \cdot \Delta \boldsymbol{A}_f > 0} e_c'' \boldsymbol{v} \cdot \Delta \boldsymbol{A}_f + \sum_{\boldsymbol{v} \cdot \Delta \boldsymbol{A}_f < 0} e_{nb}'' \boldsymbol{v} \cdot \Delta \boldsymbol{A}_f = \frac{e_c^0 - e_c''}{\tau_{eff}} \Delta V \tag{22}$$

The subscript "*c*" corresponds to values associated with the cell centroid. ΔV is the volume of the control volume and $\Delta \boldsymbol{A}_f$ is the area vector associated with face *f*. The summation on the left hand side of Eq. (21) is over all of the faces *f* of the control volume. $\Delta^3 \boldsymbol{K}$ is the extent of the control volume in wave-vector space. In Eq. (21), second-order spatial approximations have been made in integrating in $\boldsymbol{K}$ space; the spatial integration schemes are the same as those previously published [41]. The face values in Eq. (21) can be computed using several different upwinding schemes. We use a first order upwinding scheme which results in the discrete equation, Eq. (22). The subscript "*nb*" refers to the neighboring cell which shares the face *f* with the cell of interest.

Because scattering is a re-distributive process, the net scattering term integrated over the Brillouin zone must be zero, leading to the energy conservation statement in each cell:

$$\sum_{\varepsilon}\int_{BZ}\frac{e_c^0 - e_c''}{\tau_{eff}}d^3\boldsymbol{K} = 0 \tag{23}$$

The above integral is over the entire Brillouin zone volume, summed over all polarizations, ε. Numerical integration yields the discrete equation:

$$\sum_{BZ}\frac{e_c^0}{\tau_{eff}}\Delta^3\boldsymbol{K} - \sum_{BZ}\frac{e_c''}{\tau_{eff}}\Delta^3\boldsymbol{K} = 0 \tag{24}$$

In Eq. (24), "*BZ*" is used to refer to a summation over the entire Brillouin zone and polarizations. The equilibrium phonon energy, e^0, which appears in Eq. (24) is the same as that shown in Eq. (22). Using Eq. (24), we can solve for a temperature which satisfies energy conservation.

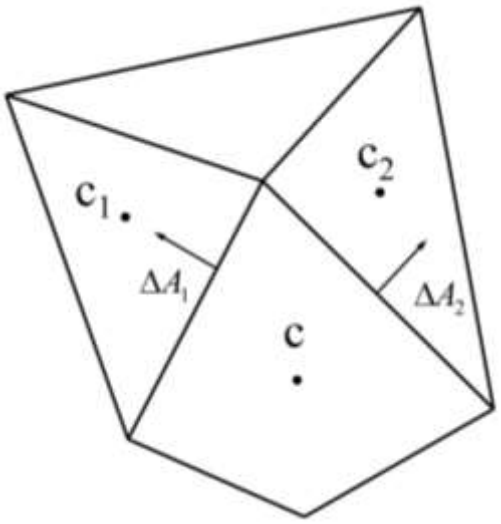

Figure 4: Discretized control volume in physical space.

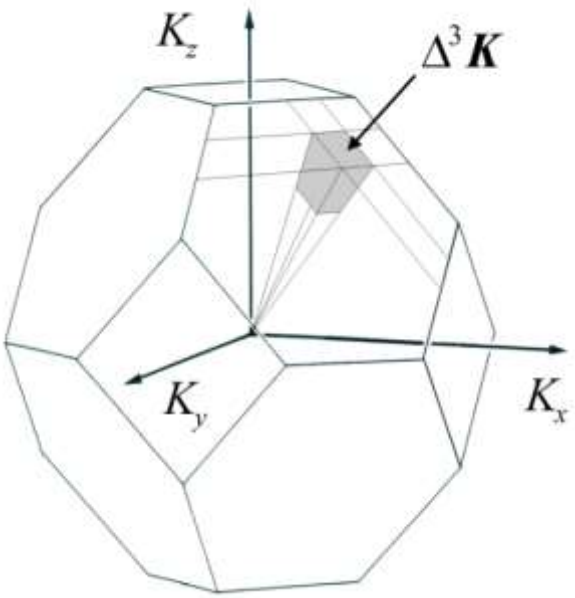

Figure 5: Schematic of a control volume in wave vector space. The Brillouin zone shown here is for a face centered cubic lattice, adapted from [9].

Our discrete equation set is thus comprised of Eq. (22) and (24). As alluded to earlier, the size of the entire equation set is N_cx$N_{\boldsymbol{K}}$xN_ε, where N_c is the number of physical space control volumes, $N_{\boldsymbol{K}}$ is the number of $\boldsymbol{K}$-space control volumes, and N_ε is the number of polarizations. To resolve three dimensional structures, the number of physical cells would typically be on the order of N_xxN_yxN_z=100x100x100=1,000,000 cells. The resolution necessary for $\boldsymbol{K}$-space need not be as fine as the spatial domain; roughly 500 to 1000 control volumes. Simple lattice structures with a single atom basis have only three polarizations (argon, krypton and other noble gasses). The most common three dimensional semiconductors, silicon and germanium, have a two atom basis and therefore have six polarizations. So, a common size for the equation set would have roughly $3\text{x}10^9$

equations. The size of this equation set renders a direct solution infeasible and leads one to resort to iterative solution procedures.

Equation (24) is only a function of ***K***-space, for all phonons at a particular location in physical space. This equation also gives the non-linear relation between the lattice temperature and the non-equilibrium energy densities. It is therefore difficult to directly incorporate Eq. (24) into Eq. (22). This implies that some iteration is required for these two equations to be solved.

The path to solution for Eqs. (22) and (24) will involve some type of iteration. Because this is a six dimensional equation, there are several different ways in which this iteration could be performed. However, as will be discussed in the next section, inter-equation coupling will give us insights as to what the optimal iteration strategy could be.

2.3 Dimensionless Parameters

The dimensionless BTE is shown below:

$$\nabla^*_{x^*} \cdot \left(\boldsymbol{s} f^*\right) = \frac{f^{0*} - f^*}{Kn}$$

$$Kn = \frac{\lambda}{L} = \frac{|\boldsymbol{v}|\tau}{L} \tag{25}$$

$$f^* = \frac{f - f_1^0}{f_2^0 - f_1^0}, \quad f^{0*} = \frac{f^0 - f_1^0}{f_2^0 - f_1^0}, \quad \boldsymbol{s} = \frac{\boldsymbol{v}}{|\boldsymbol{v}|}, \quad x^* = \frac{x}{L}, \quad \nabla^* = L\nabla$$

Here, the asterisks denote dimensionless quantities. The dimensionless quantities f^{0*} and f^* are non-dimensionalized using the maximum and minimum boundary values f_2 and f_1. $\boldsymbol{s}$ is the unit vector in the direction of the phonon group velocity. The Knudsen number, Kn, is defined as the phonon mean free path, λ, divided by the characteristic

length of the domain. We may define the mean free path as the product of the phonon group velocity magnitude multiplied by the phonon relaxation time.

Looking at the equation above, we can see that there exists intra-phonon coupling on the left hand side through the convective operator. By this we mean that the number density of a phonon of polarization ε and wave vector $\boldsymbol{K}$ at any given location is influenced by the number density of phonons of the same type upstream of the location. On the right hand side is the inter-phonon coupling which is manifested in the scattering kernel. Here, the number density of phonons of polarization ε and wave vector $\boldsymbol{K}$ at any given location is influenced by phonons of other polarization and wave vectors at the same physical location. The relative strength of these couplings is measured by the Knudsen number. For large Knudsen numbers, the right hand side of Eq. (25) is small and intra-phonon coupling dominates. In this regime, phonons of different types are effectively decoupled from each other and more-or-less travel unimpeded by other phonons. Solving the BTE as a set of decoupled convection equations (one for each polarization and discrete wave vector) becomes an effective strategy in this regime. When the Knudsen number becomes small, then the right hand side has a strong influence and the value of f^* approaches f^{0*}. In this regime, inter-phonon coupling dominates, and coupling in physical space is very weak. In the limit as Knudsen reaches 0, the domain is in equilibrium and the value of f^* is identically f^{0*}.

If the specific heat is assumed constant, the energy conservation equation in dimensionless form is as follows:

$$\sum_{\varepsilon} \int_{BZ} \frac{C\left(T_L - T\right)}{\tau_{eff}} d^3\boldsymbol{K} = 0 \tag{26}$$

The specific heat, C, is that of the individual phonon mode. T_L is the lattice temperature and is the same for all phonons, whereas T is the individual phonon temperature. We can separate the integral and rewrite as follows:

$$T_L \sum_{\varepsilon} \int_{BZ} \frac{C}{\tau_{eff}} d^3\boldsymbol{K} = \sum_{\varepsilon} \int_{BZ} \frac{C}{\tau_{eff}} T d^3\boldsymbol{K} \tag{27}$$

Above, we have recognized that the lattice temperature may be removed from inside the integral, as it only varies in physical space, and not $\boldsymbol{K}$-space. From here, we may non-dimensionalize the energy conservation equation:

$$\sum_i T_i^* \eta_i = T_L^*$$

$$\eta_i = \frac{C_i/\tau_i}{\sum_j C_j/\tau_j}, \quad T_L^* = \frac{T_L - T_{L,1}}{T_{L,2} - T_{L,1}}, \quad T = \frac{T - T_{L,1}}{T_{L,2} - T_{L,1}} \tag{28}$$

The summations are over the entire Brillouin zone and all polarizations. T^*_L is the dimensionless lattice temperature and T^*_i is the dimensionless temperature of the i^{th} phonon. The dimensionless parameter, η, will be referred to as the lattice ratio. In Eq. (28), we can see that the lattice temperature is a weighted average of all the phonons in the Brillouin zone. Each phonon is weighted by its heat capacity and the rate with which it scatters to the lattice. The lattice ratio will always lie between 0 and 1.

2.4 Closure

In this chapter, the details of the BTE were discussed. An overview of the boundary and interface conditions was given. The BTE was then discretized using the finite volume method. It was shown that the resulting equation set has a non-linear

dependence on the lattice temperature. At every particular point in physical space, all phonons coupled through an energy conservation equation. Because the equation set involves discretizing in six dimensions, the problem size quickly becomes too large for a direct solution. After a discussion of the dimensionless parameters, we have identified regimes in which inter-equation coupling may hinder convergence in an iterative solution procedure. The next chapter will discuss the sequential solution procedure and its strengths and weaknesses. An alternative solution procedure, COMET, will also be introduce and discussed in great detail. Comparisons between the two procedures will be made. Scaling results for COMET on parallel architecture will also be discussed.

3. THE COUPLED ORDINATES METHOD

The BTE involves two different spaces which must be discretized: physical space, and $\boldsymbol{K}$-space (momentum). After discretization, coupling in physical space arises from a convective operator on the LHS of the BTE. $\boldsymbol{K}$-space coupling occurs through the scattering kernel, which connects each $\boldsymbol{K}$-space control volume to an equilibrium energy density. The equilibrium energy density is calculated by forcing the scattering kernel to conserve energy. Overall, for each $\boldsymbol{K}$-space control volume, there is connectivity amongst immediate physical space neighbors (within the same $\boldsymbol{K}$-space volume), and amongst all other $\boldsymbol{K}$-space control volumes (within the same physical space control volume).

Solving this equation set by means of a direct method is virtually impossible due to the extremely large memory requirement, as well as the computational complexity. Iterative solution procedures have been a mainstay in solving the BTE, but suffer from convergence issues when inter-equation coupling in $\boldsymbol{K}$-space becomes strong. This suggests that there would be large performance gains by treating physical space coupling explicitly, instead of treating the $\boldsymbol{K}$-space coupling explicitly. What is not apparent in this strategy is that tight $\boldsymbol{K}$-space coupling implies weak physical space coupling. A Gauss-Seidel smoothing procedure would then yield slow convergence. To create an efficient solution procedure, coupling in $\boldsymbol{K}$-space as well as physical space must be addressed simultaneously.

Mathur and Murthy [103] developed the coupled ordinates method (COMET) for the solution of the radiative transport equation (RTE). COMET for the RTE achieved success in accelerating convergence rates by performing a direct solve of all equations in angular space for one cell in physical space. Each cell was visited in a Gauss-Seidel type

fashion. By doing this, slow convergence due to tight coupling in angular space is eliminated. However, the RTE suffers the same drawback as the BTE, in that tight angular coupling leads to weak spatial coupling. To address this issue, this Gauss-Siedel smoothing operator was imbedded in a geometric multigrid. Being a mature technique that has been the focus of many studies, the use of a multigrid is very effective in promoting tight coupling in physical space.

This chapter will discuss the sequential solution procedure in detail and elucidate exactly why a hindrance in solution convergence occurs. COMET will be modified from its original formulation in [103], to solve the phonon BTE. A thorough comparison between the two methods will be given. Following this, COMET will be shown to perform well on parallel architectures.

3.1 The Sequential Procedure

A number of papers have been published in the literature which solve the phonon BTE using a sequential solution procedure [40,41,98]. Here we provide a brief description. A flow chart of the sequential procedure is shown again in Fig. (6). Once the wave vector space and physical space are discretized and initialized, a polarization and a control volume in wave vector space are chosen. Equation (22) is then solved for all of physical space. The equilibrium energy density, e^0, is calculated using the prevailing value for the lattice temperature. Once satisfactory convergence is achieved, another control volume in wave vector space is chosen, and Eq. (22) is solved for all physical space, again with the same prevailing temperature to calculate e^0. This procedure is repeated until all polarizations and control volumes in wave vector space have been visited. The lattice temperature at each physical location is then calculated

using Eq. (24). In general, this is a non-linear equation because of the non-linear dependence of the Bose-Einstein distribution on temperature, and is solved using Newton iteration. This constitutes one iteration of the sequential solution procedure.

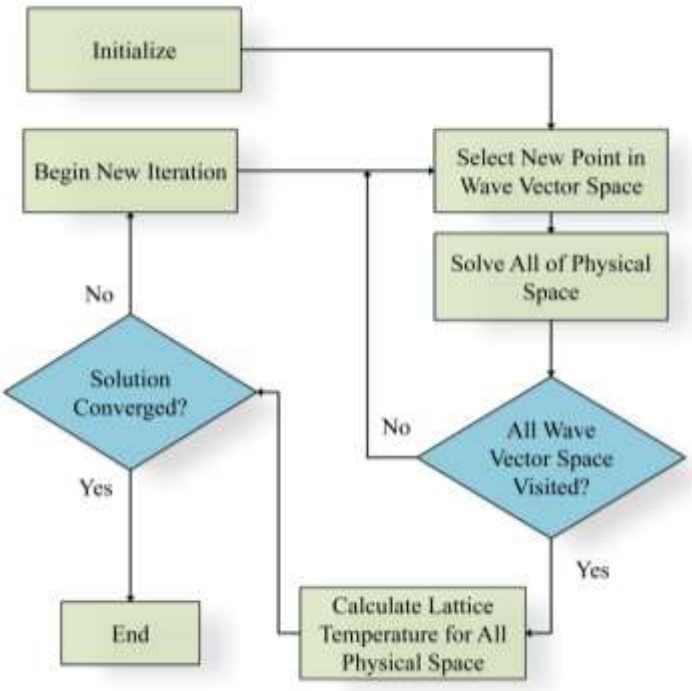

Figure 6: Flow chart for sequential solution procedure.

While the sequential procedure requires little memory compared to a full storage solution, there is a very important shortcoming. To see this, we will revisit the dimensionless BTE, but in its discretized form:

$$Kn_j \sum_{faces} f_{i,j}^{*} \boldsymbol{s}_j \cdot \Delta \boldsymbol{A}_i^{*} + f_{c,j}^{*} \Delta V_c^{*} = f_{c,j}^{0*,prev} \Delta V_c^{*} \tag{29}$$

The above equation is for the j^{th} phonon at the cell with centroid c. The superscript "*prev*" denotes quantities which are held to prevailing values. In this form, it is easy to see that the terms on the LHS of Eq. (29) are treated implicitly and the terms on the RHS are treated explicitly. When the Knudsen number is large, the first term on the LHS of Eq. (29) is large, implying that there is strong spatial coupling and the new value of f^{*} is strongly influenced by its spatial neighbors, which are treated implicitly. The influence of the explicit equilibrium distribution function is small. At high-enough Knudsen number, a sequential solution procedure converges with little difficulty. However, at low Knudsen number, the first term on the LHS of Eq. (29) is small, implying the influence of the spatial neighbors becomes small and the value of f^{*} becomes strongly coupled to the value of f^{0*}. Because f^{0*} is treated explicitly, this leads to poor convergence rates.

3.2 COMET

The low Knudsen number downfall of the sequential solution procedure is a direct result of treating ***K***-space coupling explicitly. This was in turn a result of choosing to solve all of physical space for one ***K***-space control volume. An obvious solution is to simply switch this order of iteration: solve all of ***K***-space for one physical space control volume. Though a step in the right direction, one would still suffer convergence issues at low Knudsen numbers because concurrent with tight ***K***-space is weak spatial coupling, which slows convergence of typical spatial smoothers [104].

COMET will couple equations in ***K***-space by performing a direct solve of all ***K***-space equations for a particular physical space cell. Each physical cell will be visited in turn, creating a Gauss-Seidel smoothing procedure. Physical space will be coupled by imbedding this smoothing procedure into a geometric multigrid.

It should be emphasized that COMET is only a change in the path-to-solution of the BTE. When using COMET or the sequential procedure, the same result will be reached, within the prescribed convergence tolerance.

POINT COUPLED MATRIX

Following the methodology in [103], a direct point-coupled solution for all of the phonon energies and the lattice temperature is performed at each physical cell, *c*. To make the implementation more straightforward, we cast all the equations in a delta form wherein we solve for a correction to the current solution approximation. Thus, Eq. (22) is cast in the form:

$$\sum_{\boldsymbol{v}\cdot\Delta\boldsymbol{A}_f>0}\Delta e_c''\boldsymbol{v}\cdot\Delta\boldsymbol{A}_f-\frac{\Delta e_c^0-\Delta e_c''}{\tau_{eff}}\Delta V= -\left[\sum_{\boldsymbol{v}\cdot\Delta\boldsymbol{A}_f>0}e_c''\boldsymbol{v}\cdot\Delta\boldsymbol{A}_f+\sum_{\boldsymbol{v}\cdot\Delta\boldsymbol{A}_f<0}e_{nb}''\boldsymbol{v}\cdot\Delta\boldsymbol{A}_f-\frac{e_c^0-e_c''}{\tau_{eff}}\Delta V\right]^{prev}=-R \tag{30}$$

Here, *Δe"* and Δe^0 are the corrections to the current solution approximation. The superscript for the square brackets "*prev*" refers to the values at the previous iteration. When in this form, it is easy to see that the left hand side contains the solution variables. On the right hand is the residual, *R*, of the current solution approximation. It is important to note that the neighbor values are not being corrected in Eq. (30), as their influence is

treated explicitly. The corresponding energy conservation statement cast in correction form is given by:

$$\sum_{BZ} \frac{\Delta e_c^0}{\tau_{eff}} \Delta^3 \boldsymbol{K} - \sum_{BZ} \frac{\Delta e_c''}{\tau_{eff}} \Delta^3 \boldsymbol{K} = -\left[\sum_{BZ} \frac{e_c^0}{\tau_{eff}} \Delta^3 \boldsymbol{K} - \sum_{BZ} \frac{e_c''}{\tau_{eff}} \Delta^3 \boldsymbol{K} \right]^{prev} = -R_L \tag{31}$$

As with Eq. (30), the left hand side contains the solution variables and the right hand side is the residual, R_L, of the current solution approximation.

Equations (30) and (31) contain a correction to the equilibrium energy density, Δe^0. We may perform a Taylor series expansion in temperature about the prevailing temperature:

$$\Delta e^0 \approx \left(\frac{\partial e^0}{\partial T} \right)^{prev} \Delta T \tag{32}$$

At a particular physical cell, each phonon mode shares the same equilibrium lattice temperature, so ΔT, the correction to the current temperature, is invariant in wave vector space. We may rewrite Eq. (30) as:

$$\sum_{\boldsymbol{v} \cdot \Delta \boldsymbol{A}_f > 0} \Delta e_c'' \boldsymbol{v} \cdot \Delta \boldsymbol{A}_f + \Delta e_c'' \frac{\Delta V}{\tau_{eff}} - \Delta T_c \left(\frac{\partial e^0}{\partial T} \right)^{prev} \frac{\Delta V}{\tau_{eff}} = -R \tag{33}$$

The energy conservation statement may be re-written as follows:

$$\Delta T_c \sum_{BZ} \left[\left(\frac{\partial e^0}{\partial T} \right)^{prev} \frac{\Delta^3 \boldsymbol{K}}{\tau_{eff}} \right] - \sum_{BZ} \Delta e_c'' \frac{\Delta^3 \boldsymbol{K}}{\tau_{eff}} = -R_L \tag{34}$$

In their new forms, the BTE and the energy conservation statement relate the lattice temperature *T* and the phonon energy density *e''* to each other. With this, the point-coupled linear system may be written as:

$$\begin{bmatrix} \left(\sum_{\boldsymbol{v}\cdot\Delta\boldsymbol{A}_f>0} \boldsymbol{v}\cdot\Delta\boldsymbol{A}_f + \frac{\Delta V}{\tau_{eff}} \right)_1 & & & \left(-\frac{\partial e^0}{\partial T}\frac{\Delta V}{\tau_{eff}} \right)_1 \\ & \left(\sum_{\boldsymbol{v}\cdot\Delta\boldsymbol{A}_f>0} \boldsymbol{v}\cdot\Delta\boldsymbol{A}_f + \frac{\Delta V}{\tau_{eff}} \right)_2 & & \left(-\frac{\partial e^0}{\partial T}\frac{\Delta V}{\tau_{eff}} \right)_2 \\ & & \ddots & \vdots \\ & & \left(\sum_{\boldsymbol{v}\cdot\Delta\boldsymbol{A}_f>0} \boldsymbol{v}\cdot\Delta\boldsymbol{A}_f + \frac{\Delta V}{\tau_{eff}} \right)_n & \left(-\frac{\partial e^0}{\partial T}\frac{\Delta V}{\tau_{eff}} \right)_n \\ \left(-\frac{\Delta^3 \boldsymbol{K}}{\tau_{eff}} \right)_1 & \left(-\frac{\Delta^3 \boldsymbol{K}}{\tau_{eff}} \right)_2 & \cdots \left(-\frac{\Delta^3 \boldsymbol{K}}{\tau_{eff}} \right)_n & \sum_{BZ} \left[\left(\frac{\partial e^0}{\partial T} \right) \frac{\Delta^3 \boldsymbol{K}}{\tau_{eff}} \right] \end{bmatrix} \begin{bmatrix} \Delta e_1'' \\ \Delta e_2'' \\ \vdots \\ \Delta e_n'' \\ \Delta T \end{bmatrix} = - \begin{bmatrix} R_1 \\ R_2 \\ \vdots \\ R_n \\ R_L \end{bmatrix}$$

(35)

Here *n+1* is the total number of equations to be solved at each cell, and is equal to the number of wave vector control volumes multiplied by the number of polarizations plus an extra equation for energy conservation. *R* is the residual to the current solution approximation.

The "arrowhead" structure of the point coupled matrix, also called the Jacobian matrix, in Eq. (35) is engineered deliberately and is critically important in obtaining efficient solutions. It is obtained in the following way. The diagonal entries, excluding

the last diagonal, include terms which couple a phonon's energy to itself, i.e., a portion of the convection and scattering terms. Terms involving *e"* of the neighbor cells are included in the residual *R*. The coefficients in the bottom row represent the energy conservation statement and couple the lattice temperature to all other phonons. The terms in the last column couple a phonon to the lattice temperature. The relegation of neighbor-cell terms to *R*, and the presence of scattering term combine to create an "arrowhead" structured linear system, which may be solved in *O(n)* operations. The Jacobian matrix in Eq. (35) is in general non-linear because of the non-linear dependence of the Bose-Einstein distribution on the lattice temperature (the entire last column). Consequently, several direct solutions of Eq. (35) must be performed, each time updating the last column.

At reflecting boundaries, the energy being emitted from the wall is entirely a function of the phonon energy incident on the wall. Thus, emitted phonons are coupled to one or more incident phonons. For diffuse reflections, the emitted phonons are coupled to *all* incident phonons, while for specular reflections there is a one-to-one coupling between an emitted and an incident phonon. In the COMET procedure, this may be accounted for through a point-coupled matrix with off-diagonal elements (not in the last row or last column). Though such coupling would improve convergence rates, an arrowhead matrix structure such as that in Eq. (35) is no longer obtained. Instead, the matrix would have a general dense structure depending on boundary orientation, and the complexity of a point-coupled inversion would scale as $O(n^3)$. To avoid this computational cost, we retain the arrowhead structure for the Jacobian even at reflecting

boundaries. The terms that do not conform to this structure are treated explicitly, and are moved to the right-hand side of the discrete algebraic equation set. This makes the linear solution procedure iterative even for linear problems (constant specific heat), but we have found that the overall computational cost is lower than that for solving the fully-dense matrix for problem sizes of practical interest. At a boundary cell, once the linear system is solved, the point values are corrected, and the phonon boundary energies are recalculated for the reflecting wall. The residual is checked, and the decision to repeat or move on is made.

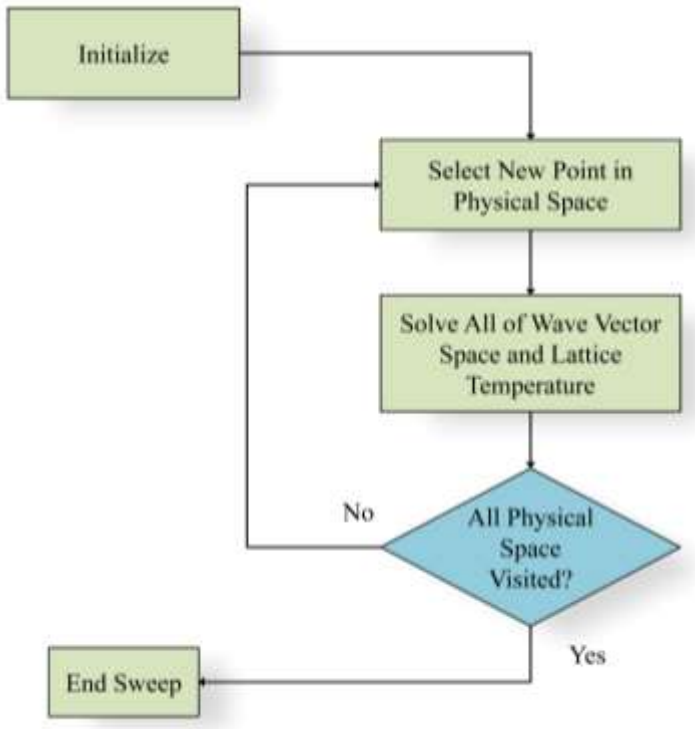

Figure 7: Flow chart for one relaxation sweep for COMET.

Above is a flow chart showing one relaxation sweep for the COMET solution procedure. One sweep for COMET involves an outer loop over all points in physical space, each point requiring a direct solve of Eq. (35). Once all points in physical space have been visited, convergence is checked and the choice to continue sweeping is made. This relaxation sweep is embedded in a geometric multigrid procedure to ensure strong spatial coupling, as described below.

GEOMETRIC MULTIGRID

The point-coupled procedure described above promotes coupling in wave-vector space. To promote coupling in physical space, a full approximation storage (FAS) [105] geometric multigrid method is used, with the point-coupled Gauss-Seidel scheme as a relaxation sweep.

In typical geometric multigrid methods, new grids are created at each multigrid level, independent of their finer-level counterparts. To avoid this inconvenience, we create coarser-level grids by agglomerating cells from the next finer level. Agglomeration is carried out by visiting each fine level cell and merging it with the neighbor cell that shares the largest face. Coefficients are then created by discretizing the governing equations directly on the coarse mesh geometry. A first-order discretization of convective operators is employed on all levels. Because no diffusion operators need be discretized, the non-convexity of coarse-level meshes is not a concern [106].

To demonstrate the procedure used in the FAS scheme, we consider a setup with M levels. The fine level equation to be solved is:

$$L_0\left(e'',T\right)=0 \tag{36}$$

Here L_0 represents the solution to the phonon BTE (Eq. (22)) and the calculation of the lattice temperature (Eq. (24)). First, pre-sweeps of the point-coupled Gauss-Seidel procedure are performed on the fine level. After the k^{th} iteration, the residual is:

$$L_0\left(e''^k,T^k\right)=R_0^k \tag{37}$$

The current solution approximation and the current residual are then interpolated to the next coarsest level. The interpolation of the current solution approximation is done by taking the volume average of the constituent fine cells as the value for the coarse cell as shown below.

$$\Re_l^{l+1}\left(e''\right)=\left.\frac{\sum_{j\in J} e''_j\,\Delta V_j}{\sum_{j\in J}\Delta V_j}\right|_{J=0}^{N_{cells}^{l+1}} \tag{38}$$

The above restriction operator projects the current solution value at level l to the next coarse level $l+1$. The summations are over all fine level cells j which comprise the coarse level J. This is performed on all cells in the level $l+1$, N_{cells}^{l+1}. We denote the interpolated fine level solution by e''^0 and T^0. The residual is interpolated by using the summed residual of the constituent fine cells as the coarse cell value as shown below.

$$\Re_l^{l+1}(R) = \sum_{j \in J} R_j \Big|_{J=0}^{N_{cells}^{l+1}} \tag{39}$$

At a coarse level, we solve the same governing equations with an added source term to account for the discrepancy between discretizations, in keeping with the FAS framework. The coarse level equation to be solved is as follows:

$$L_{l \neq 0}(e'', T) = R_{l-1}^{k} + L_{l \neq 0}\left(e''^{0}_{l-1}, T_{l-1}^{0}\right) \tag{40}$$

$L_{l \neq 0}$ represents a coarse level BTE which solves for a coarse level approximation to the non-equilibrium energy density and equilibrium temperature. This equation holds for any arbitrary level l which is not equal to zero. The first term on the right hand side is the interpolated residual and the second term on the right hand side is the residual computed using the interpolated solution. The process of performing pre-sweeps and interpolating solutions/residuals is applied to all coarse grids until we have reached the coarsest level. After k iterations on the coarsest level, we apply a correction to the next finer level:

$$\Delta e''_{M-1} = P_M^{M-1}\left(e''^{k}_{M} - \Re_{M-1}^{M}\left(e''^{0}_{M-1}\right)\right) \tag{41}$$

where

$$P_l^{l-1}(e'') = e''_J\big|_{j \in J} \tag{42}$$

is the prolongation operator which interpolates values from a level *l* to the next finer level *l-1*. The prolongation operator sets the value of all cells *j* on level *l-1* to the value of cell *J* on level *l*, where the cells *j* make up the coarse level cell *J*.

At convergence, the fine level residual is zero, implying that the solution interpolated to the next coarser level will satisfy the coarse level operator. Thus, at convergence no correction is applied and the final solution on the finest mesh is independent of the coarse-mesh solutions, as desired. A standard V-cycle with one pre-sweep and two post-sweeps is used [105] for the work presented here, though any of the numerous published multigrid cycling schemes may be used as well.

3.3 Verification

To verify our algorithm, we compare our results with the exact solution of the radiative transport equation (RTE) for a gray isotropically scattering medium bounded by walls at prescribed temperatures. The exact solution as a function of Knudsen number has been given by Heaslet and Warming [107]. Because the sequential solution procedure and the COMET procedure solve the exact same equations, at convergence the dimensionless solution should be the same for both, within the prescribed tolerance. However, we only present the verification of the COMET procedure for the sake of brevity.

We use the exact solutions provided by Heaslet and Warming [107,108] for thermal radiation and adapt it to 1D gray phonon transport. Pictured in the inset is the domain to be used. The spatial domain is discretized equally into N_x finite control

volumes. An isotropic Brillouin zone (a sphere in wave vector space) and discretized into N_θxN_ϕ finite solid angles in the octant. The error is defined as the average deviation from the exact solution:

$$error = \frac{1}{N_x}\sum_{cells}\left|T - T_{HW}\right| \tag{43}$$

Above, T is the solution produced by COMET and T_{HW} is the exact solution as found from Heaslet and Warming. Volume averaging is not necessary, as all cells are the same size. Figure (8) shows the convergence rates for the spatial and angular discretization for Kn=1. The order of convergence is found to be first order in physical space and second order in wave-vector space, as expected.

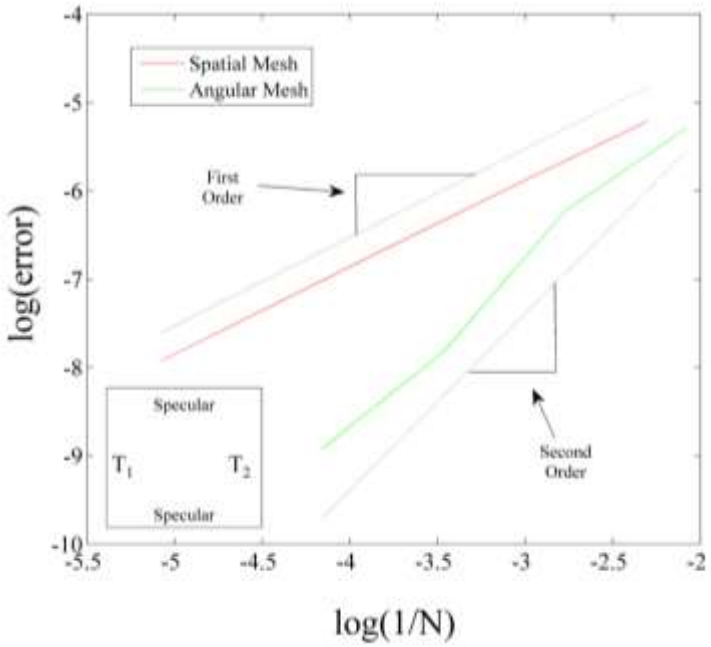

Figure 8: Convergence rates for the angular and spatial discretization. On the abscissa, N refers to N_x for the spatial mesh, and N_θ for the angular mesh. The error is defined as the average deviation from [107].

3.4 Comparison with the Sequential Procedure

The performance of the COMET algorithm is tested for the case of steady heat conduction in the domain shown in Fig. (9). A square domain of side L has two boundaries held at temperature T_1 and two at temperature T_2, as shown. The objective is to compute the lattice temperature field and heat flux in the domain, and benchmark the performance of COMET against the sequential solution procedure across a range of domain Knudsen numbers between 0.01 and 10. All computations are performed on the supercomputing cluster Hansen at Purdue University's Rosen Center for Advanced Computing (http://www.rcac.purdue.edu/userinfo/resources/hansen/). The specific processor used is a 2.3 GHz AMD Opteron 6176 with 96 GB of RAM.

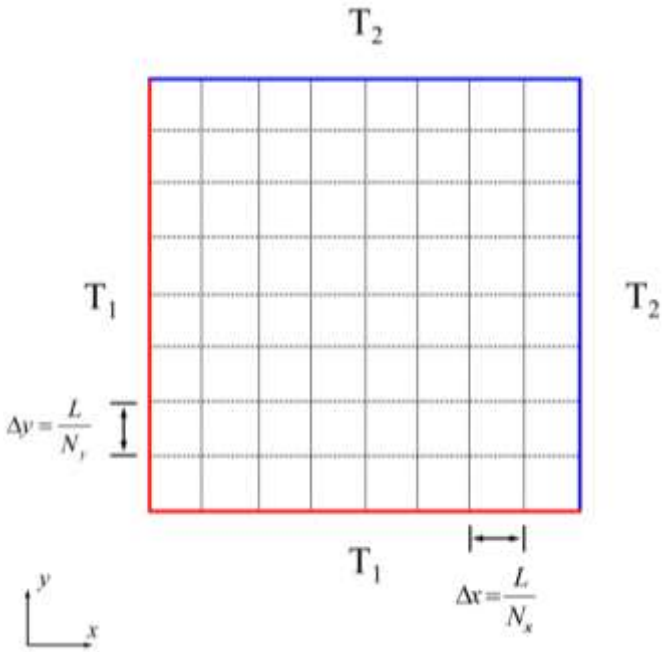

Figure 9: Computational domain used for benchmarking COMET.

The sequential and COMET procedures are assumed converged when two criteria are met simultaneously. The first criterion requires that the relative residual falls below 10^{-5}. The relative residual is defined as the current scaled residual divided by the largest scaled residual encountered in the first five iterations. The scaled residual for COMET is defined as:

$$R_{scaled} = \frac{\sum_{cells}\sum |R|}{\sum_{cells} tr(A)} \tag{44}$$

Here, *tr(A)* is the trace of the arrowhead matrix in Eq. (35). The second summation in the numerator refers to the summation over all residuals found in the right hand side vector in Eq. (35). The summation in the denominator and the first summation in the numerator is the summation over all spatial cells in the domain.

The second criterion, which is the limiting criterion, requires that the absolute value of the relative heat balance falls below 10^{-8}. The relative heat balance is defined as:

$$\left(\sum q\right)_{relative} = \frac{q_{left} + q_{right} + q_{top} + q_{bottom}}{q_{left}} \tag{45}$$

GRAY APPROXIMATION

Benchmarking of the COMET algorithm is performed for four Knudsen numbers: 10, 1, 0.1, and 0.01, three angular discretizations: 2x2, 4x4, and 8x8 (in the octant), and

three values for N_x (=N_y): 50, 100, 200. The performance of the COMET algorithm relative to that of the sequential solver is shown in Figs. (10) and (11).

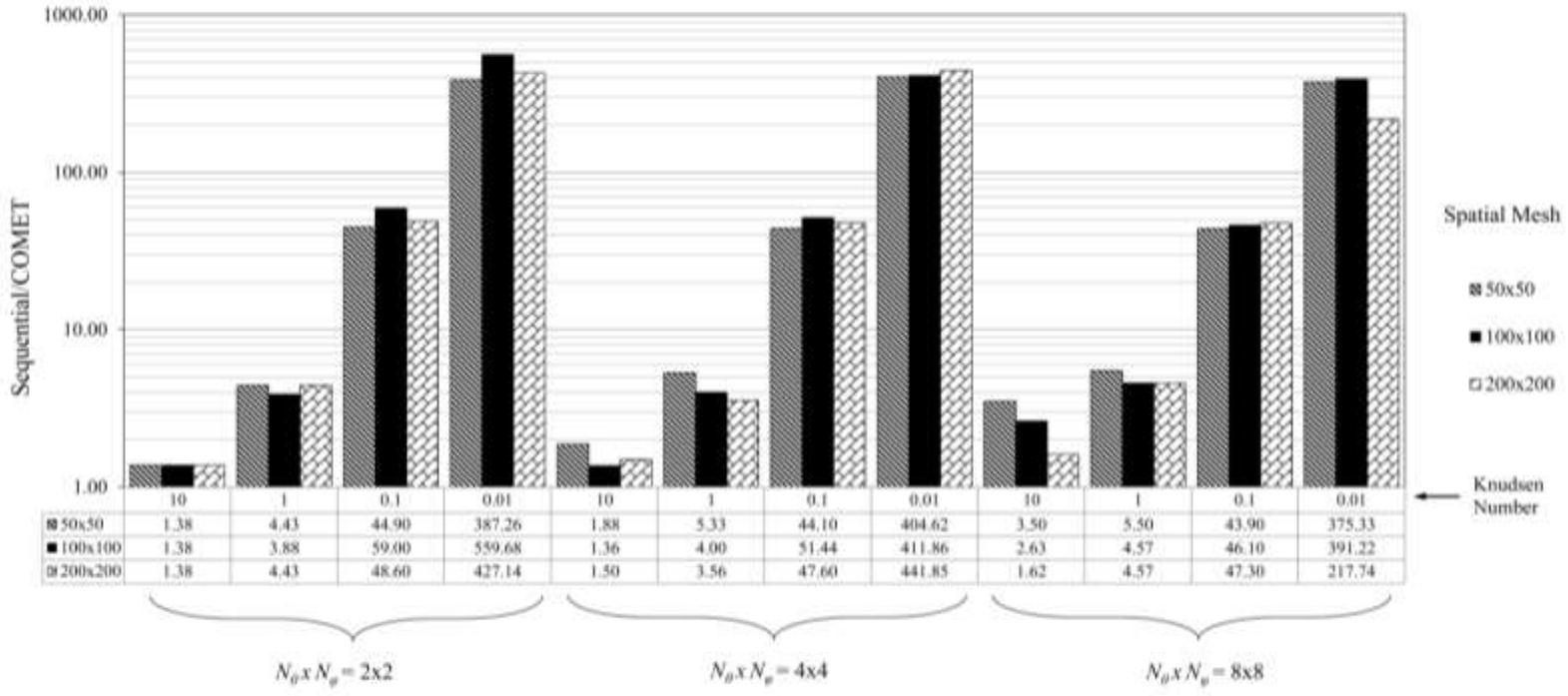

	10	1	0.1	0.01	10	1	0.1	0.01	10	1	0.1	0.01
50x50	1.38	4.43	44.90	387.26	1.88	5.33	44.10	404.62	3.50	5.50	43.90	375.33
100x100	1.38	3.88	59.00	559.68	1.36	4.00	51.44	411.86	2.63	4.57	46.10	391.22
200x200	1.38	4.43	48.60	427.14	1.50	3.56	47.60	441.85	1.62	4.57	47.30	217.74

Figure 10: Ratio of the iteration count for the sequential and COMET procedures. In the table below the chart are the numerical values for each column. Horizontal brackets group similar angular space discretizations. Within a bracket, moving horizontally traverses the Knudsen numbers, whereas moving vertically traverses the mesh sizes.

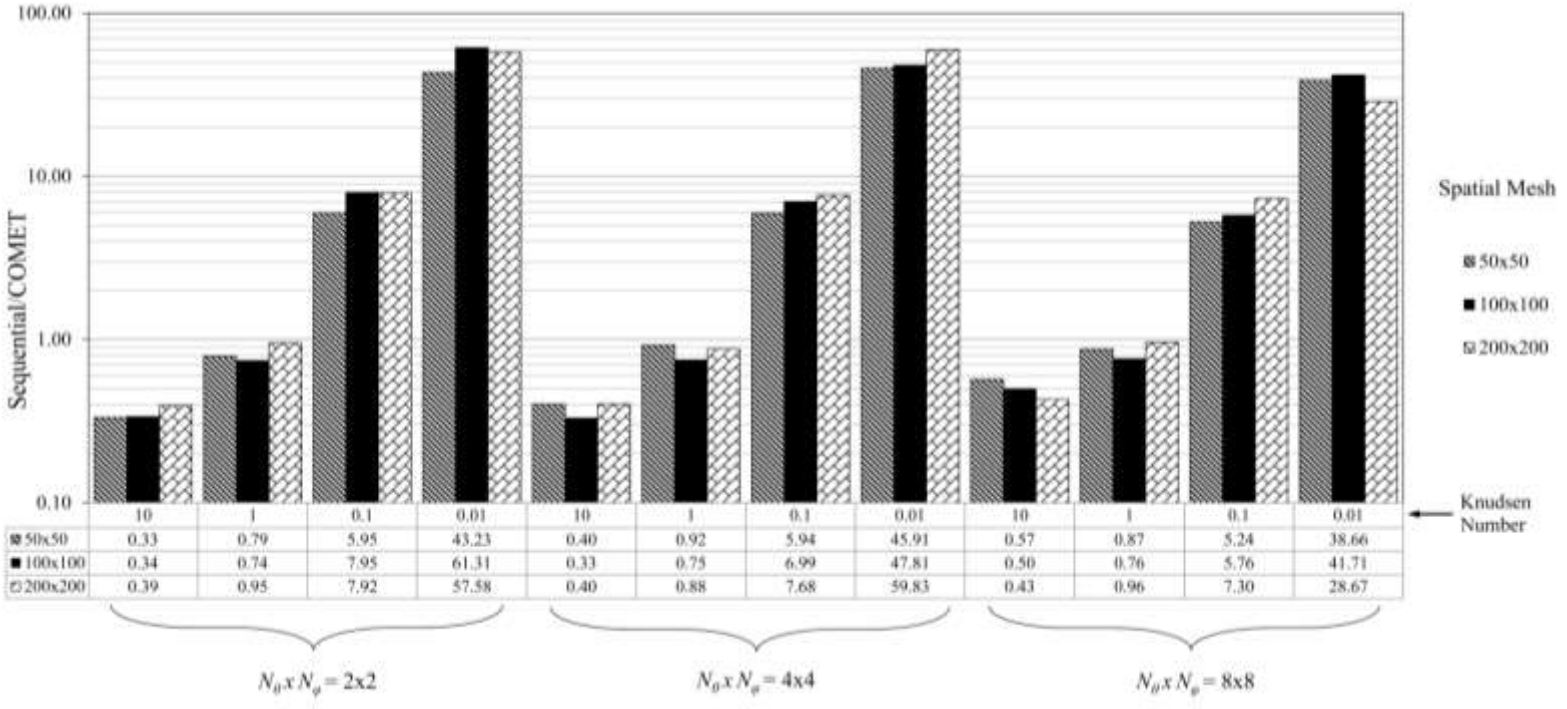

	10	1	0.1	0.01	10	1	0.1	0.01	10	1	0.1	0.01
50x50	0.33	0.79	5.95	43.23	0.40	0.92	5.94	45.91	0.57	0.87	5.24	38.66
100x100	0.34	0.74	7.95	61.31	0.33	0.75	6.99	47.81	0.50	0.76	5.76	41.71
200x200	0.39	0.95	7.92	57.58	0.40	0.88	7.68	59.83	0.43	0.96	7.30	28.67

Figure 11: Ratio of the total time taken for sequential and COMET procedures. In the table below the chart are the numerical values for each column. Horizontal brackets group similar angular space discretizations. Within a bracket, moving horizontally traverses the Knudsen numbers, whereas moving vertically traverses the mesh sizes.

Figure (10) shows the ratio of the iteration counts for the two procedures. In all cases, the sequential procedure requires more iterations than COMET, by as much as a factor of 560. In general, COMET outperforms the sequential solver across the range of Knudsen number, and significant iteration acceleration is obtained for $Kn<1.0$. It should also be noted that the iteration count ratio is relatively invariant with angular and spatial discretization for the same Knudsen number.

Figure (11) shows the ratio of the total solution time for the two procedures. COMET outperforms the sequential procedure for moderate to low Knudsen numbers, by a factor of 5-40 times. However, for Knudsen numbers at or above 1, COMET is slower than the sequential solution procedure. This is because the COMET procedure requires more time per iteration than the sequential procedure. The extra time results from the cost of creating coefficients on the fly in the geometric multigrid procedure. It is found that COMET requires 3-9 times more time per iteration than the sequential procedure. Therefore, we do not see a gain from using COMET until the Knudsen number is below 1. However, this is not of great concern since the absolute computational time for either procedure is very low for high Knudsen numbers. Again, relative performance is relatively invariant with angular and spatial discretizations.

Table 1 shows the absolute computational time and iterations to convergence for the two procedures for a spatial mesh of 200x200 cells and an angular discretization of 8x8 in the octant. Significant gains in computational efficiency are found for $Kn>1$.

Table 1: Iteration count and total time for N_xxN_y=200x200 and N_θxN_ϕ=8x8.

Kn	10		1		0.1		0.01	
Procedure	COMET	Sequential	COMET	Sequential	COMET	Sequential	COMET	Sequential
Total Time (min)	34.03	14.61	19.41	18.63	25.48	186.01	155.56	4459.52
Iteration Count	13	21	7	32	10	473	66	14371

K-RESOLVED PHONON TRANSPORT SIMULATIONS

We now examine the solution acceleration obtained when considering ***K***-resolved phonon transport. We consider thermal transport in silicon assuming an isotropic spherical Brillouin zone. The dispersion curves used are shown in Fig. (12), and correspond to the [100] crystal directions in bulk silicon. Because we are using an isotropic Brillouin zone, its orientation with respect to the physical directions is only important from a numeric standpoint. That is, with a solution that is not yet independent of the Brillouin zone discretization, different results may be obtained by arbitrarily changing the axis orientation. With a solution which has been discretized enough to be independent of Brillouin zone discretization, the solution will change only within the specified convergence tolerance. Nonetheless, we note that $\boldsymbol{K}_x$, $\boldsymbol{K}_y$, and $\boldsymbol{K}_z$ are oriented along the *x*, *y*, and *z* directions. Four polarizations are shown, corresponding to the longitudinal acoustic (LA), transverse acoustic (TA), longitudinal optical (LO) and transverse optical (TO) modes. The two transverse modes are degenerate in this high symmetry direction [109].

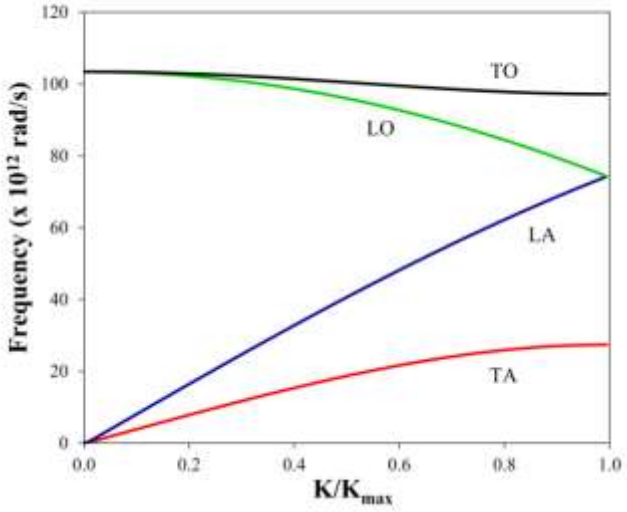

Figure 12: Dispersion relation for silicon in the [100] direction at 300 K using the environment dependent interatomic potential (EDIP) [42].

The dispersion relation is found by using the environment-dependent interatomic potential (EDIP) [42] for bulk silicon. In addition to the discretization in angular space, the wave vector magnitude is discretized equally into N_k = 1, 2, 4, and 8 segments. A schematic of the discretization of the Brillouin zone is shown in Fig. (13).

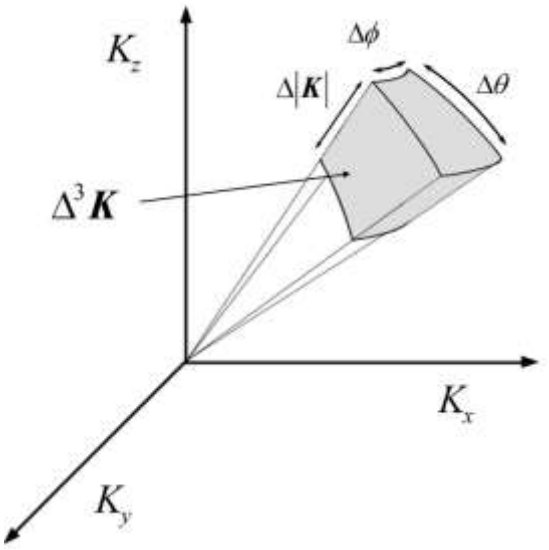

Figure 13: Discretization of the Brillouin zone for a non-gray dispersion relation.

The relaxation times are found from curve-fits to bulk experimental data [110]:

$$\tau_{im}^{-1} = A\omega^4$$
$$\tau_u^{-1} = BT\omega^2 e^{-C/T} \tag{46}$$

Here, τ_{im} is the relaxation time for impurity scattering and τ_u is that for Umklapp scattering. Mattheissen's rule [46] is used to obtain the effective relaxation time:

$$\tau_{eff}^{-1} = \tau_{im}^{-1} + \tau_u^{-1} \tag{47}$$

The constants *A*, *B*, and *C* are 1.32 x10^{-45} s^3, 1.73 x10^{-19} s/K, and 137.36 K, respectively. For this paper, the relaxation times are held constant with temperature and are evaluated at 300 K. This restriction is not necessary. However, a temperature-dependent relaxation time implies a spatially-variable Knudsen number which we avoid for the sake of clarity

in benchmarking. Using the above relaxation times and the dispersion relation in Fig. (12), the spread in phonon mean free paths may be plotted as a function of frequency, as shown in Fig. (14).

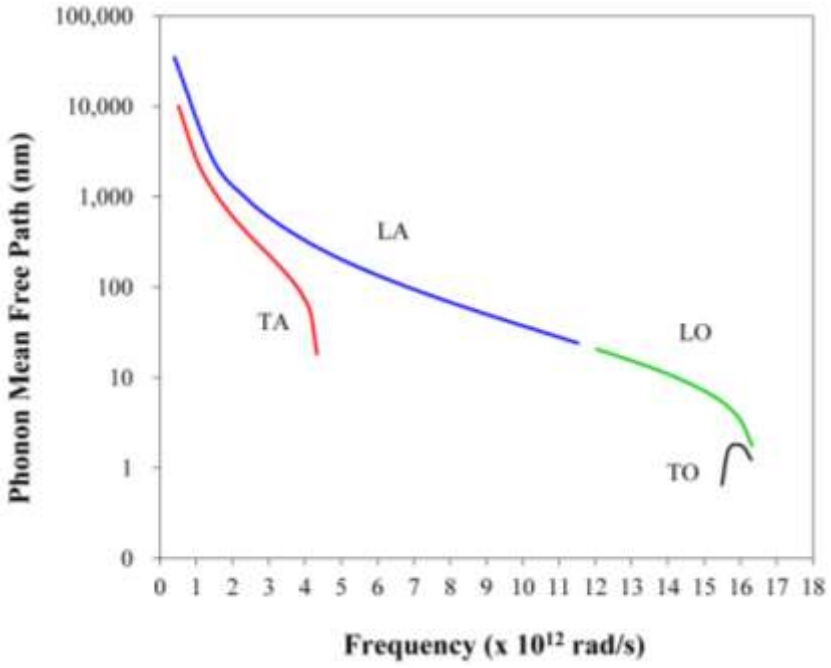

Figure 14: Phonon mean free path as a function of polarization and frequency for bulk silicon.

For this test case, each discrete control volume in ***K*** space is characterized by a separate Knudsen number. We report results in terms of an average Knudsen number, defined as:

$$Kn = \frac{1}{L} \frac{\sum_{p} \sum_{BZ} |\boldsymbol{v}| \tau_{eff} \Delta^3 \boldsymbol{K}}{\sum_{p} \sum_{BZ} \Delta^3 \boldsymbol{K}} \tag{48}$$

Figure (15) shows the ratio of the iteration count for the two procedures. The results are shown for varying discretizations of the wave vector magnitude, and varying the average Knudsen number. The spatial discretization is held constant at N_xxN_y=50x50, and the angular discretization at N_θxN_ϕ=2x2 in the octant. From Fig. (15), the ratio of the iteration count is seen to dramatically favor COMET across the range of average Knudsen number, regardless of the discretization of wave vector magnitude. It is particularly dramatic at average *Kn* values of 0.1 or higher, with COMET requiring far fewer iterations to convergence; factors between 200-2000 are obtained. This is because there is a large range of Knudsen numbers for the different ***K***-space discretizations corresponding to the average *Kn* defined by Eq. (48). This variation may be as large as 2-5 orders of magnitude. The largest and smallest mean free paths for the different discretizations of wave vector magnitude are shown in Table 2. With finer discretizations of ***K*** magnitude, the spread in mean free path becomes much wider (only 2 orders of magnitude for N_k=1 versus 5 orders of magnitude for N_k=8). However, just as with the angular and spatial discretization, we see almost no dependence on the iteration ratio for different discretizations in wave vector magnitude. In some instances (for example, *Kn*=0.01 and N_k =8), the sequential procedure does not converge to a solution after 200 hours of computation, and therefore the result is not reported in Fig. (15). As with the

previous results, the solution acceleration is found to be relatively invariant with angular and spatial discretization (not shown).

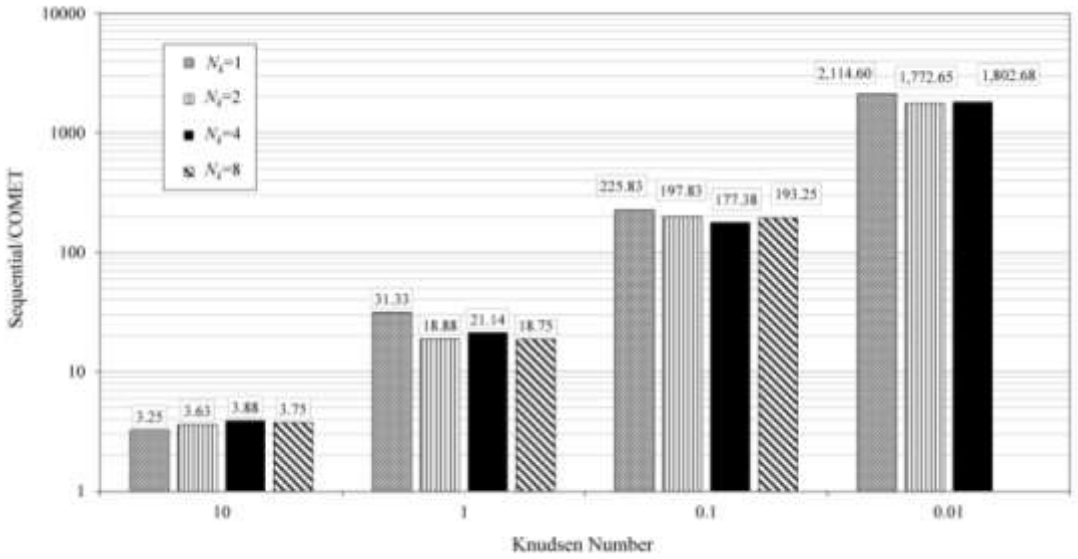

Figure 15: Ratio of the iteration count for the sequential and COMET procedures. The spatial and angular discretizations used are N_xxNy=50x50 and N_θ xN_ϕ=2x2 in the octant, respectively.

Table 2: Spread in phonon mean free path for different discretizations of wave vector magnitude.

	Mean Free Path (m)			
N_k	1	2	4	8
Minimum	1.3×10^{-9}	1.2×10^{-9}	8.0×10^{-10}	4.0×10^{-10}
Maximum	2.8×10^{-7}	8.0×10^{-7}	3.3×10^{-6}	1.5×10^{-5}

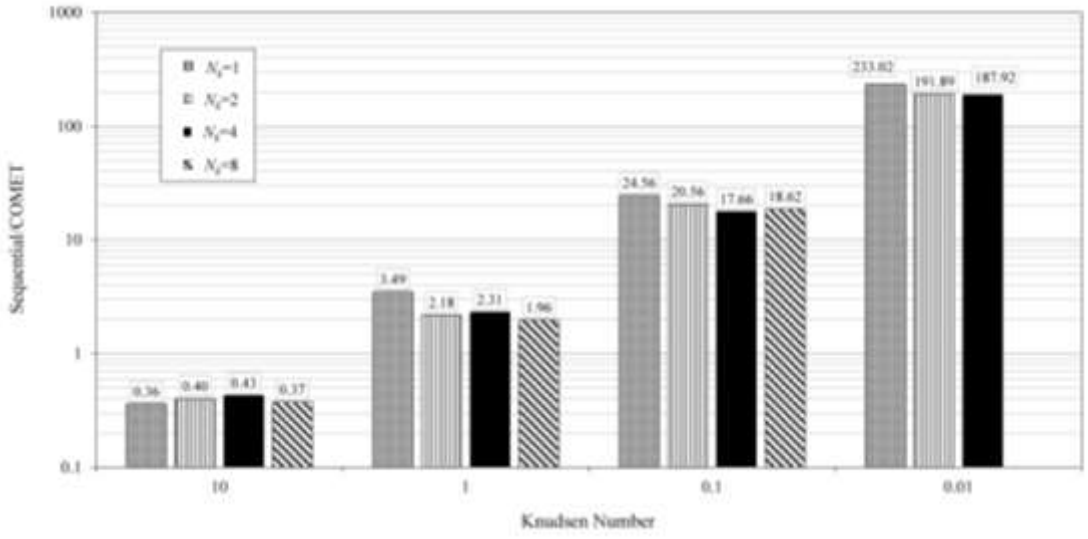

Figure 16: Ratio of the total time for the sequential and COMET procedures. The spatial and angular discretizations used are N_xxN_y=50x50 and N_θxN_ϕ=2x2 in the octant, respectively.

Table 3: Iteration count and total time for N_xxN_y=50x50, N_θxN_ϕ=2x2, and N_k=4.

Kn	10		1		0.1		0.01	
Procedure	COMET	Sequential	COMET	Sequential	COMET	Sequential	COMET	Sequential
Total Time (min)	1.11	0.47	0.95	2.19	1.80	31.82	4.53	851.92
Iteration Count	8	31	7	148	13	2306	34	61291

Figure (16) shows the ratio of the total time for the sequential and COMET procedures. Dramatic gains in computational speed with respect to the sequential procedures are obtained with COMET for average *Kn* values of unity or lower; acceleration factors of 3-200 are obtained. Again, this is a result of the wide range of ***K***-dependent Knudsen numbers corresponding to the average *Kn* value in Table 2. For these non-gray simulations, COMET requires approximately 9 times more time per iteration than the

sequential procedure. Stronger inter-***K*** coupling in the non-gray case gives COMET a significant enough advantage over the sequential procedure and allows it to overcome the disadvantage due to increased time per iteration.

Table 3 shows the iteration count and total time for a case with $N_x x N_y$=50x50, $N_\theta x N_\phi$=2x2, and N_k=4. Solution acceleration is obtained using COMET for *Kn=1* or higher; the upper limit on *Kn* for acceleration is higher than for the gray case. The iteration count is seen to be relatively constant for COMET, with a modest increase at *Kn*=0.01 because the stronger ***K***-space coupling makes it more difficult for spatial coupling to influence the calculation. The iteration count for the sequential solution procedure, on the other hand, increases by roughly an order or magnitude or more with every order-of-magnitude decrease in Knudsen number. For *Kn=0.01*, COMET requires 4.53 mins of computation, while the sequential procedure requires 14.2 hours of computation to meet the same convergence criterion.

3.5 Parallel Scaling

As mentioned earlier, the parallel performance of the COMET algorithm is expected to be very good because of the high data locality and the point coupled nature of the calculations. This section highlights the parallel performance of the COMET algorithm. Parallelization is accomplished by using domain decomposition. Each processor is given a portion of the mesh and computations are performed using explicit values of ghost cells. When the computation is complete, the ghost cells are updated

using a message passing interface. The partitioning software ParMETIS [111] is used to decompose the domain.

STRONG SCALING

To show the scalability of the COMET solution procedure for the phonon BTE, we use the same domain shown in Fig. (9). The specific heat is not assumed to be constant, which requires multiple iterations of Eq. (35) for each cell. We also use a Brillouin zone which is assumed isotropic, but resolved in the wave vector magnitude just as in Figs. (12) and (13), using Eqs. (46) and (47) for the relaxation times. As before, the orientation of $\boldsymbol{K}_x$, $\boldsymbol{K}_y$, and $\boldsymbol{K}_z$ are along the x, y, and z directions. The resolution of the wave vector space is N_θxN_ϕx$N_{\boldsymbol{K}}$ = 4x4x2 in the octant. Since we are simulating a two-dimensional domain, only the top half of the Brillouin zone need be considered. This yields 512 discrete wave vector control volumes, or 513 equations in the point linear system at each cell. Figure (17) shows strong scaling results for three different domain sizes.

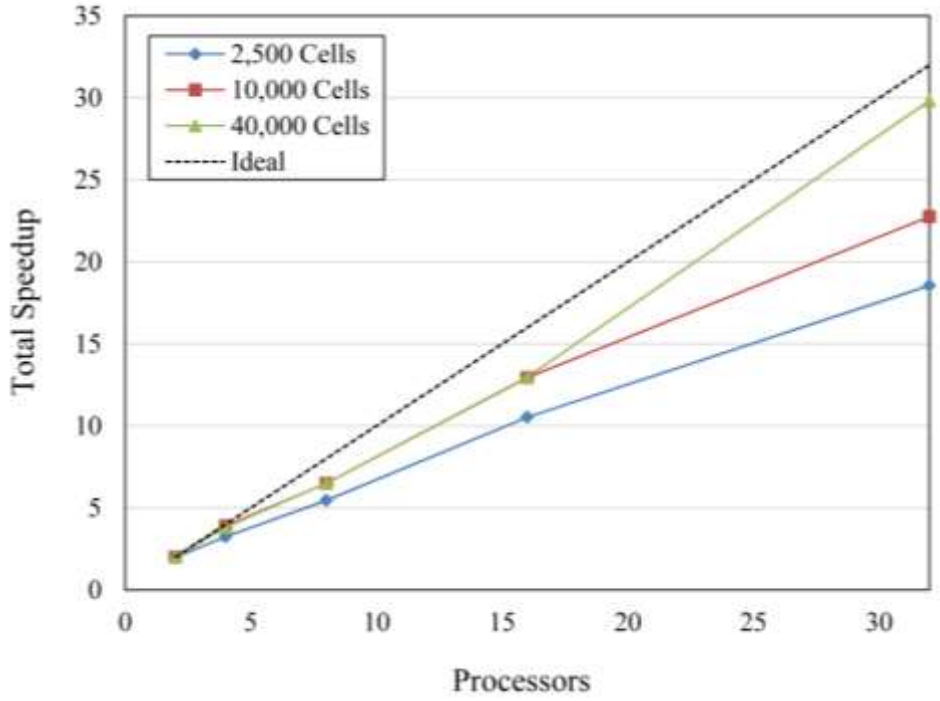

Figure 17: Strong scaling of COMET for the phonon BTE for different physical mesh sizes.

In Fig. (17), we can see that COMET shows excellent scaling, even up to 32 processors; the finest mesh had only 1250 cells per processor, while the coarsest mesh had about 78 cells per processor. For the three mesh sizes, the number of coarse levels was chosen such that for each mesh the number of coarsest level cells was approximately 80.

As the number of processors is increased, the total iteration count increases slightly because of the explicit nature of domain decomposition. Figure (18) shows the strong scaling of COMET for the time taken per iteration. This gives a better estimation of the raw scalability of COMET.

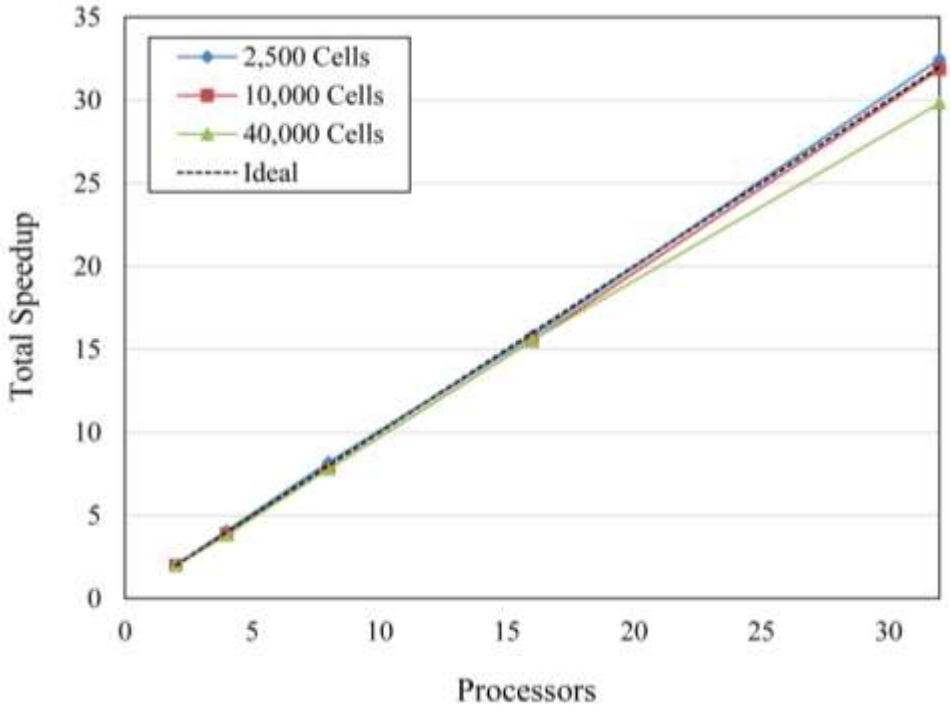

Figure 18: Time per iteration strong scaling of COMET for the phonon BTE for different physical mesh sizes.

The difference between Fig. (17) and (18) shows that the main culprit for sub-linear scaling is the increase in iteration count as the domain is decomposed. Despite the slight increase in iteration count, the parallel efficiency is excellent as shown in Fig. (19).

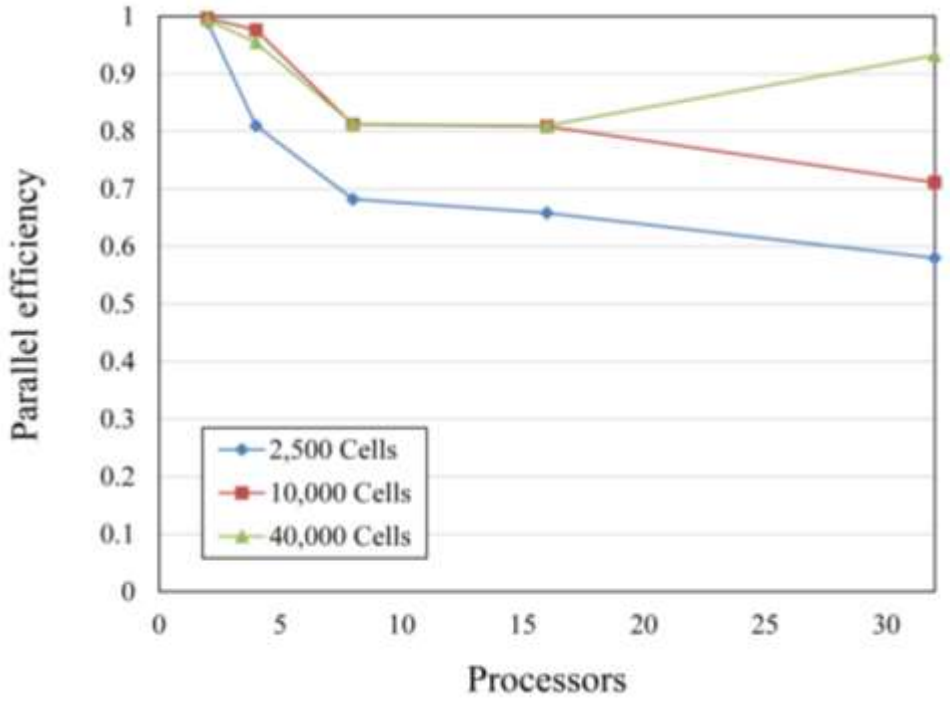

Figure 19: Parallel efficiency of COMET for the phonon BTE.

Finally, we show the strong scaling of COMET for different discretizations of the wave vector space. This is important to discuss given that the success of COMET's scalability is credited to the point-coupled nature of the computations. However, an increase in point computations (by refining the wave vector discretization) may not necessarily lead to better scaling. Refining the wave vector space is in fact a double edged sword: more refinement means more computations, but also means more data must be passed for each ghost cell. Therefore, it is important to see the impact of these competing factors.

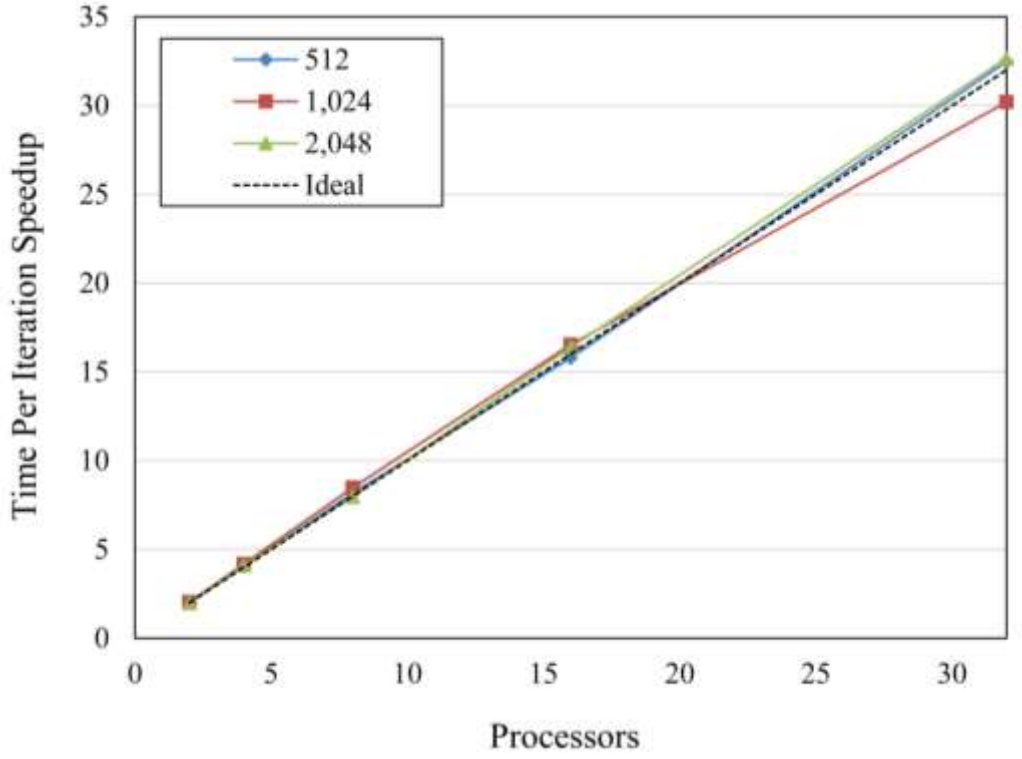

Figure 20: Strong scaling of COMET for the phonon BTE for different discretizations of wave vector space. A spatial mesh of 2,500 cells is used.

From Fig. (20), we can see that COMET shows excellent scaling, regardless of the discretization of the wave-vector space.

WEAK SCALING

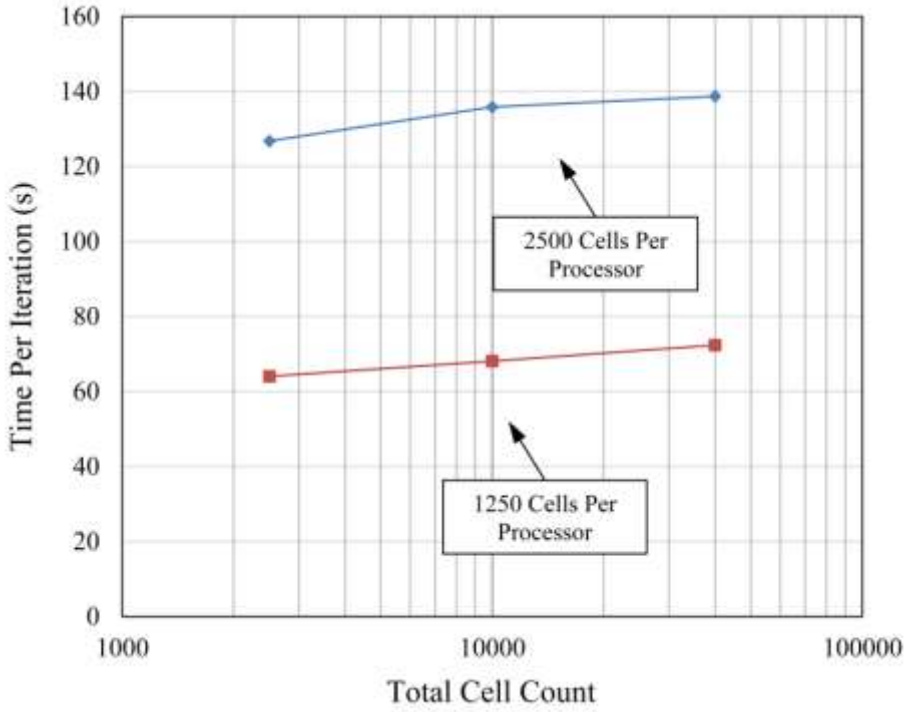

Figure 21: Weak scaling of COMET for the phonon BTE.

We now examine the weak-scaling behavior of COMET. Figure (21) shows the time taken per iteration when the problem size is increased over all, but the problem size per processor stays the same. As the number of cells in the domain increases, the time per iteration increases only slightly, further demonstrating the scalability of COMET.

3.6 Closure

This chapter reviewed the sequential solution procedure and discussed its drawbacks. By analyzing the sequential procedure, it was found that a successful solution procedure must be have the means to resolve tight coupling in ***K***-space as well as

weak coupling in physical space. With this in mind, COMET, which was developed for the solution of the RTE, was identified as an ideal solution procedure for solving the phonon BTE. As with the RTE, COMET achieved excellent solution acceleration because of the complimentary use of a point coupled solution to implicitly treat $\boldsymbol{K}$-space coupling and a geometric multigrid to implicitly treat physical space coupling. Solution speedup relative to the sequential procedure was measured to be as high as 233 times on a single core. Parallel scaling indicated that COMET maintained excellent efficiency for a relatively small amount of physical cells per core.

In the next chapter, we will extend COMET to include phonon transport across interfaces. It will be seen that because of the point coupled procedure, COMET serves as an ideal framework for simulating transport across interfaces. Benchmarking against the sequential procedure is discussed as well.

4. COMET ALGORITHM FOR PHONON TRANSPORT ACROSS HETEROGENEOUS INTERFACES

The previous chapter addressed the application of COMET for simulating phonon transport in single material domains. COMET's novel solution procedure is successful because of its ability to resolve strong coupling between ***K***-space control volumes. This coupling occurred because of volumetric scattering, which becomes strong when the Knudsen number is small.

This chapter will extend COMET to incorporate phonon transport across heterogeneous material interfaces on a single processor. When a phonon encounters an interface, a portion of its energy is transmitted across the interface into another ***K***-space control volume, and a portion of its energy is reflected off the interface into another ***K***-space control volume. Because of the physics at any interface, ***K***-space coupling occurs not only within a given interface cell, but across the interface as well.

Chapter 1 discussed several methods for obtaining interface transmission coefficients. Early models include the acoustic mismatch model (AMM) [52,53] and the diffuse mismatch model (DMM) [55,112] which make simplifying assumptions about the nature of the interface and the impinging phonons. Newer models, such as the atomistic Greens function (AGF) [60], wave packet dynamics [54], and molecular dynamics simulations [113], strive to eliminate simplifying assumptions by performing more advanced, system level calculations. For simplicity, we consider transmission coefficients obtained from the DMM. This way, the method is not obfuscated by details of more complex transmission models. It should be noted however, that as far as the method is concerned there is no preference to which transmission model is used.

As mentioned earlier, our motivation for this extension is rooted in nanocomposite materials for thermoelectric applications. In these materials, interfaces

become an important scattering mechanism due large interfacial density. COMET has already been shown to confer significant acceleration when volumetric scattering is dominant, so it is important to separate the effects of these two mechanisms. With this in mind, we will first benchmark COMET against the sequential solution procedure for three simple one dimensional test cases in the absence of volumetric scattering. The first test case will have one material interface; the second test case will have two material interfaces; the third test case will four material interfaces.

With COMET measured against the sequential procedure for several simple scenarios, we will establish solution acceleration using a domain which is similar to a nanoparticle composite. We use CT scans of a micron scale sintered copper bed and meshing software to create a realistic domain. The mesh is then scaled to obtain a domain Knudsen number of 1 and 10. Phonon transport for this domain will include volumetric scattering as well.

4.1 Calculating Interface Heat Flux

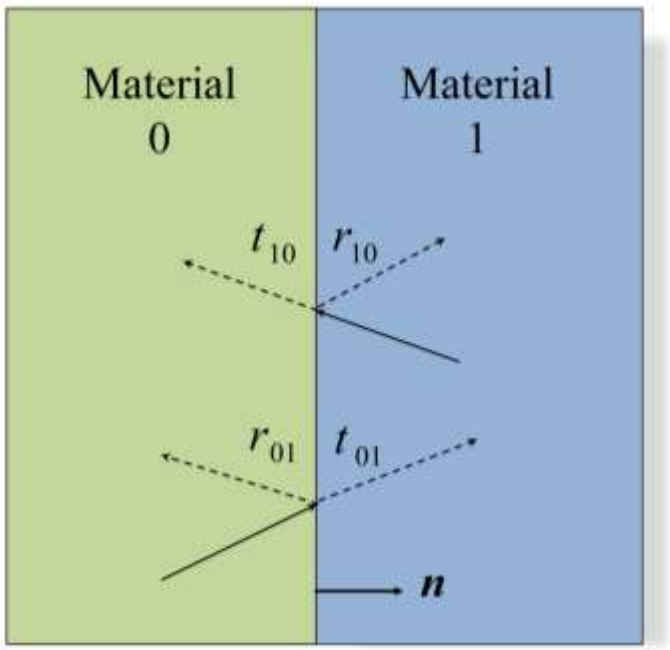

Figure 22: A schematic of a heterogeneous material interface. Arrows are used to represent the direction of reflection and transmission from one side to another.

We consider here an interface between two materials, as shown in Fig. (22). A common combination of materials would be silicon and germanium. The consequence of a material interface is an abrupt change in the dispersion relation of the solid. Two materials will allow for a different range of vibrational frequencies, as well as different group velocities.

The DMM involves purely elastic phonon transmission across interfaces, which requires a phonon to maintain the same frequency during transmission or reflection. As a result of the discretization in ***K***-space, we must be forced to allow dissimilar frequencies to interact. To accomplish this, we first separate the wave vector space into frequency

bins. In doing this, we effectively approximate the delta function in Eq. (17) as a step function for the j^{th} frequency bin. It is equal to 1 when the frequency is between $\omega_{j,high}$ and $\omega_{j,low}$ and 0 everywhere else. Figure (23) shows the dispersion relation for silicon in the [100] direction with typical frequency bins marked as dotted lines. Typical wave vector control volume centroids are marked with black squares.

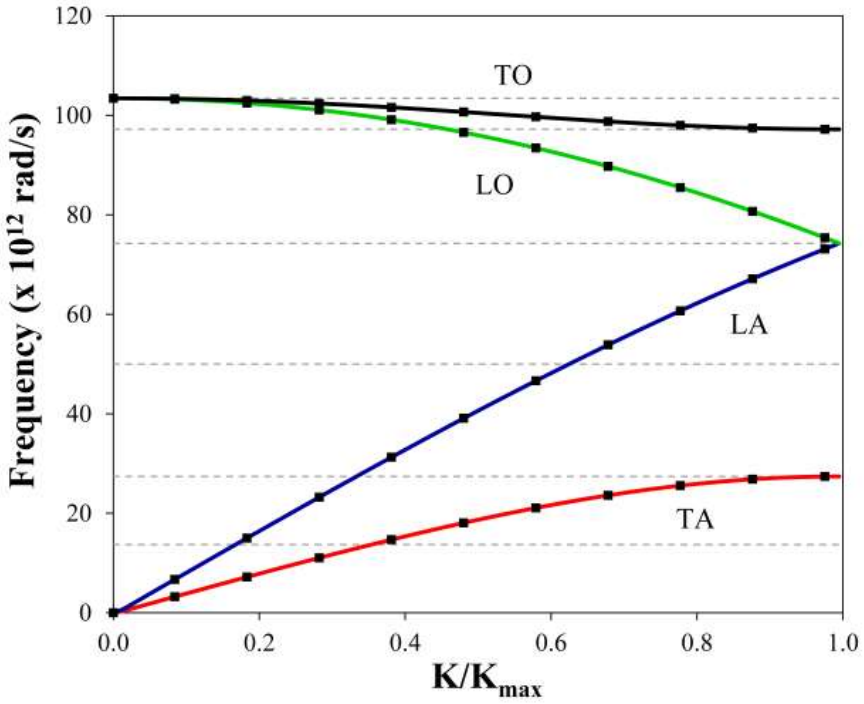

Figure 23: Dispersion relation for silicon in the [100] direction using the environment dependent interatomic potential (EDIP) [42]. The square symbols represent the discrete wave vectors K whose frequencies fall into the discrete frequency bins (shown by dotted lines). Phonon BTE computations are carried out at discrete $\boldsymbol{K}$ values.

If only small temperature differences occur in the problem, a constant specific heat may be assumed and the equilibrium energy density may then be written as:

$$e^0 \approx \left(\frac{\partial e^0}{\partial T}\right)_{ref} \left(T - T_{ref}\right) \tag{49}$$

We may insert Eq. (49) into Eq. (17) to obtain the transmission coefficient:

$$t_{01,j} = \frac{-\left[\sum_{i=1}^{N_{1,j}} \left(\frac{\partial e^0}{\partial T}\right)_{i,ref} \boldsymbol{v}_i \cdot \boldsymbol{n}\Delta^3 \boldsymbol{K}_i\right]_1}{\left[\sum_{i=1}^{N_{0,j}} \left(\frac{\partial e^0}{\partial T}\right)_{i,ref} \boldsymbol{v}_i \cdot \boldsymbol{n}\Delta^3 \boldsymbol{K}_i\right]_0 - \left[\sum_{i=1}^{N_{1,j}} \left(\frac{\partial e^0}{\partial T}\right)_{i,ref} \boldsymbol{v}_i \cdot \boldsymbol{n}\Delta^3 \boldsymbol{K}_i\right]_1} \tag{50}$$

Above, the temperature dependence is cancelled out because all phonons use the same reference temperature to calculate the specific heat. Here, $\boldsymbol{n}$ is the normal of the interfaces and points from material 0 to material 1.

We calculate the heat flux, $q''_{int,1,j}$ leaving the interface and entering material 1 in the j^{th} frequency band [114] as follows:

$$q''_{int,1,j} = \left[t_{01,j} \sum_{i=1}^{N_{0,j}} e_i'' \boldsymbol{v}_i \cdot \boldsymbol{n}\Delta^3 \boldsymbol{K}_i\right]_0 - \left[r_{10,j} \sum_{i=1}^{N_{1,j}} e_i'' \boldsymbol{v}_i \cdot \boldsymbol{n}\Delta^3 \boldsymbol{K}_i\right]_1 \tag{51}$$

Knowing the heat flux for the j^{th} frequency bin, we determine the values for each e'' within the j^{th} bin in material 1 which have $\boldsymbol{v}\cdot\boldsymbol{n}>0$. Because there may be several different frequencies in the frequency bin, the heat flux must be distributed, so to speak, into each discrete $\boldsymbol{K}$-space control volume such that the temperature is appropriate.

We distribute the phonon energy which is emitted from the interface in the j^{th} frequency bin into material 1 according to the following rule:

$$e_i'' = w_{i,1} q''_{int,1,j}$$
$$w_{i,1} = \left[\frac{\left(\frac{\partial e^0}{\partial T} \right)_{i,ref}}{\sum_{i=1}^{N'_{1,j}} \left(\frac{\partial e^0}{\partial T} \right)_{i,ref} \boldsymbol{v} \cdot \boldsymbol{n} \Delta^3 \boldsymbol{K}_i} \right]_1 \tag{52}$$

which is the expression found in [114]. It should be noted that these weights will not add up to unity unless it is multiplied by $\boldsymbol{v}\cdot\boldsymbol{n}$ (and the $\boldsymbol{K}$-space volume). The summation of w by itself (with the wave vector volume) will give the inverse of the specific heat weighted average group velocity.

4.2 Interface Treatment in COMET

Within the COMET framework, it is useful to think of the phonon energy at a spatial location as a vector quantity. Every entry within the vector is a value of the non-equilibrium energy density for a particular $\boldsymbol{K}$-space volume and polarization. The interface operator projects the phonon energy onto either a different material represented by a different vector space, or the same material represented by the same vector space. All the details of the interface model are encapsulated in the structure of the interface operator. Using these interface operators, the interface condition may be written as:

$$\begin{aligned} \vec{E}''_{i,1} &= \mathfrak{I}_{01} \vec{E}''_0 + \mathfrak{R}_{10} \vec{E}''_1 \\ \vec{E}''_{i,0} &= \mathfrak{I}_{10} \vec{E}''_1 + \mathfrak{R}_{01} \vec{E}''_0 \end{aligned} \tag{53}$$

Here $\mathfrak{T}_{01}$ ($\mathfrak{T}_{10}$) is the transmission operator for phonons in material 0 (1) being transmitted to material 1 (0) and $\mathfrak{R}_{10}$ ($\mathfrak{R}_{01}$) is the reflection operator for phonons in material 1 (0) being reflected off an interface with material 0 (1). $\vec{E}''_{i,1}$ $\left(\vec{E}''_{i,0}\right)$ is the vector of phonon energy which is being emitted from the interface into material 1 (0).

Using Eqs. (51), and (52), the transmission operator from material 0 to 1 may be written as:

$$\left[\mathfrak{I}_{01}\right]_{i,k} = w_{i,1} t_{01} \boldsymbol{v}_k \cdot \boldsymbol{n} \Delta^3 \boldsymbol{K}_k H\left(\boldsymbol{v}_k \cdot \boldsymbol{n}\right) H\left(\boldsymbol{v}_i \cdot \boldsymbol{n}\right) \tag{54}$$

In the equation above, *i* refers to the row index of the transmission operator which is also the index of the outgoing phonon in material 1. The i^{th} row of the transmission operator maps the i^{th} phonon to all the incoming phonons in the opposite material. The index *k* refers to the column of the transmission operator which is also the index of the phonon incident to the interface in material 0. The k^{th} column in the transmission operator will give a map of all phonons to which the k^{th} phonon in material 1 transmits energy to the phonons in material 0. The transmission coefficient t_{01} belongs to the frequency band to which the phonons *i* and *k* belong (if they are in different frequency bands the coefficient is zero). *H* is the Heaviside step function. A similar expression can be written for the reflection operator:

$$\left[\mathfrak{R}_{10}\right]_{i,k} = w_{i,1} r_{10} \boldsymbol{v}_k \cdot \boldsymbol{n} \Delta^3 \boldsymbol{K}_k H\left(-\boldsymbol{v}_k \cdot \boldsymbol{n}\right) H\left(\boldsymbol{v}_i \cdot \boldsymbol{n}\right) \tag{55}$$

The i^{th} row of the reflection operator gives a list of all phonons which reflect energy into the i^{th} phonon. The k^{th} column gives a list of all phonons to which the k^{th} phonon reflects energy.

All reflection operators are square matrices, whereas a transmission operator need not be. The actual structure of the interface is dependent on the orientation of the interface normal. Each operator will have a density of approximately 25%. This can be seen from the Heaviside step functions in Eqs. (54) and (55). For each interface face, four interface operators must be created and stored.

FACE AGGLOMERATION

Crucial to the COMET solution procedure is the use of a FAS geometric multigrid. In order to accelerate convergence of the point-coupled procedure described in the previous chapter, a series of coarse meshes is created; solutions obtained on these coarse meshes provide corrections to finer mesh levels to accelerate convergence [105].

Coarse level meshes are created by agglomerating fine level cells together. During mesh creation, for computational efficiency, when two fine-level cells are agglomerated, new coarse faces are created by summing fine level faces which have common coarse level cells.

Because of the Heaviside step functions in Eqs. (54) and (55), the number of non-zero elements in both operators is ~25%. For a practical problem, the number of discrete ***K***-space control volumes can range from a few hundred to a few thousand. Since we must create four interface operators per interface face, there is computational gain in minimizing the number of interface faces at all mesh levels. Furthermore, an effective

transmission/reflection operator must be defined at all multigrid mesh levels. In this paper, the equivalent interface operator (for both reflection and transmission) is written as:

$$\mathfrak{I}_{I,01} = \sum_{i \in I} \frac{\Delta \boldsymbol{A}_I \cdot \Delta \boldsymbol{A}_i}{\Delta \boldsymbol{A}_I \cdot \Delta \boldsymbol{A}_I} \mathfrak{I}_{i,01}$$
$$\Delta \boldsymbol{A}_I = \sum_{i \in I} \Delta \boldsymbol{A}_i \tag{56}$$

Here, the summations are over all finer level faces, *i*, which make up the coarse level face, *I*.

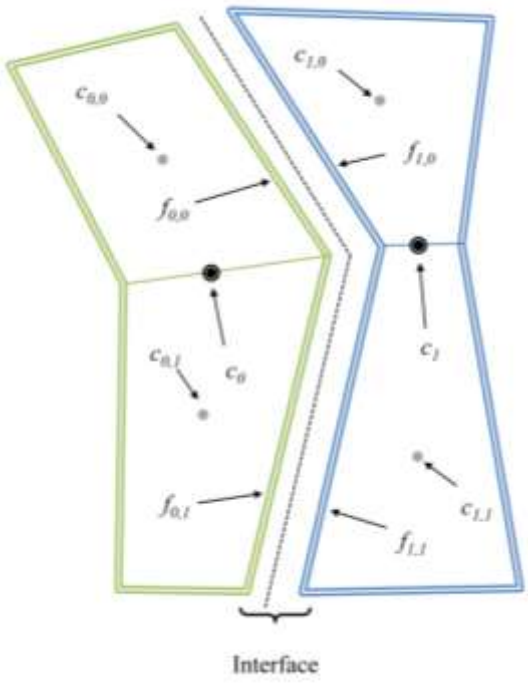

Figure 24: Schematic of the interface face agglomeration.

For example, using Fig. (24), let us say that fine level cells $c_{0,0}$ and cell $c_{0,1}$ combine to make a coarse level cell c_0. Correspondingly, cell $c_{1,1}$ and cell $c_{1,1}$ combine to make a coarse cell c_1. We can then combine faces $f_{0,1}$ and $f_{0,0}$ to make a coarse level face and combine faces $f_{1,0}$ and $f_{1,1}$ to make a coarse level face. When writing the transmission or reflection operator for cell c_0, the summation would be over faces $f_{0,0}$ and $f_{0,1}$. When finding the transmission or reflection operator for c_1, the summations would be over face $f_{1,0}$ and $f_{1,1}$.

PARTIALLY IMPLICIT TREATMENT

At any mesh level, for a given cell which is on an interface, Eq. (53) has a phonon energy contribution from the neighboring cell on the other side of the interface, and a component from the current cell of interest. Because of this dependence, the solution at any interface cell may be treated in a partially implicit manner. This treatment is similar to the way boundary conditions are handled in [115]. At a cell which lies on an interface (or boundary), the non-linear iteration procedure is outlined in the flowchart below.

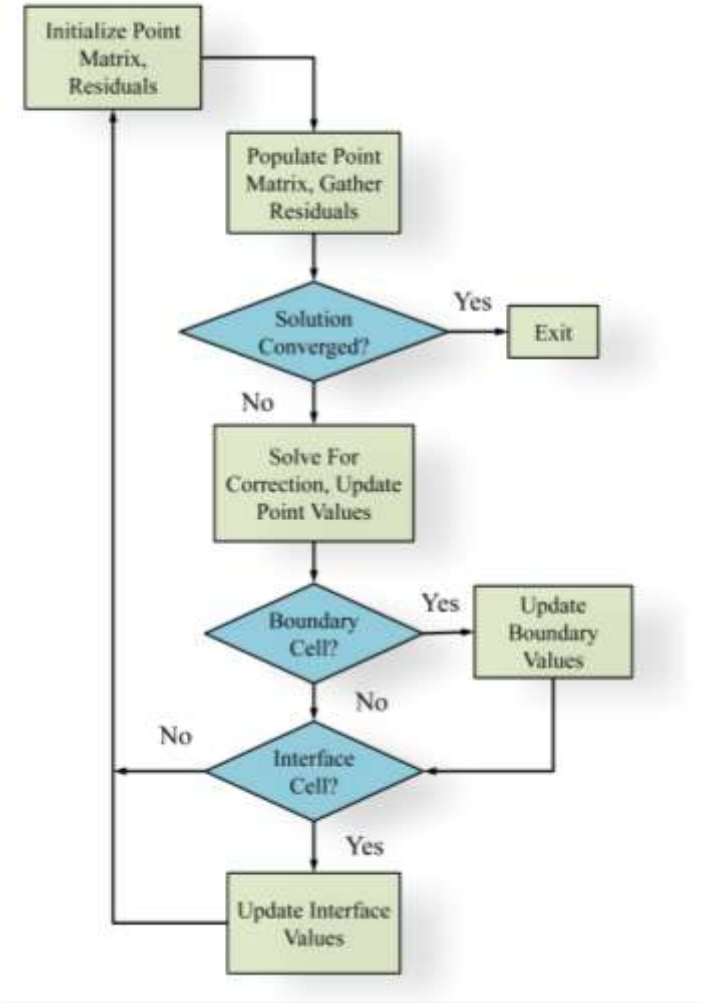

Figure 25: Flow chart for the non-linear point coupled solution procedure which includes interface and boundary cell treatment.

Iteration begins by initializing the point matrix and the residual array. The linear system is then constructed and residuals are gathered. Convergence is then judged with the newly acquired residuals. If the solution is not converged, the point coupled linear system is solved and the correction to the current solution approximation is found. If the cell in question is on a reflecting boundary, the boundary values are then updated. If the cell in question is on an interface, then the interface values are updated. The procedure

begins again by reinitializing the residuals and the point matrix, then repopulating them, and determining whether the solution is converged.

Within the framework of the code, different materials are relegated to separate meshes. We therefore perform a predetermined amount of Gauss-Seidel sweeps for a particular mesh (for this thesis, we will use two) using the above treatment at interface/boundary cells. With the updated values in the mesh, the interface conditions for all neighboring meshes are updated. The next mesh is selected and the process is repeated. This continues until all meshes have been visited. A global residual is then calculated and the decision to continue or exit is made.

4.3 Sequential Interface Treatment

In the sequential procedure, all inter-phonon coupling is treated explicitly. A consequence of this is the requirement that all of the interface conditions be treated explicitly as well. Interface conditions are updated at the same time the lattice temperature is calculated. A flow chart for the solution procedure is shown below.

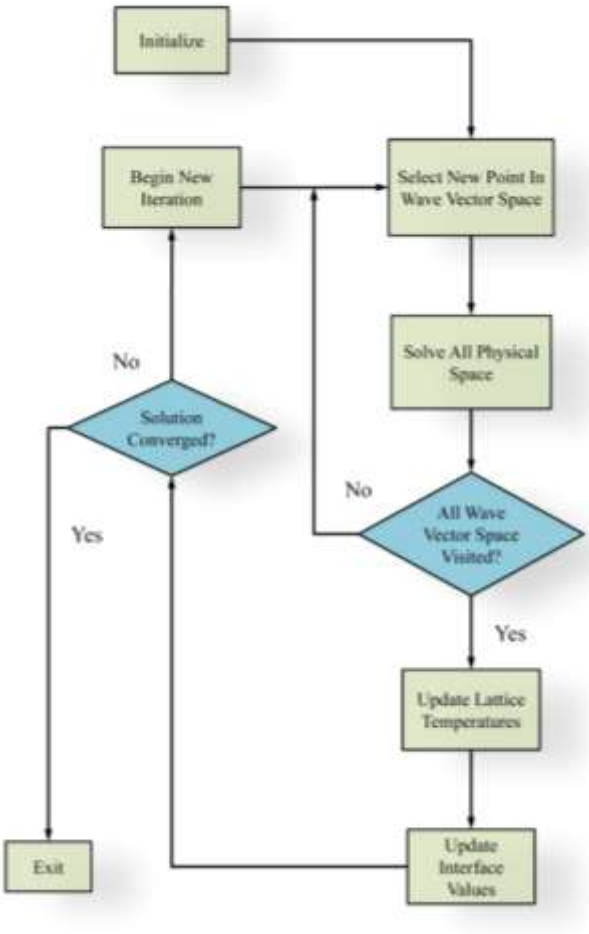

Figure 26: Flow chart for the sequential solution procedure with interface treatment included.

The simulation starts out by initializing the domain. As was discussed in Chapter 3, all of physical space is solved for each volume in ***K***-space in turn. Once all of K-space has been visited, energy conservation is enforced, and the lattice temperature is calculated. The interface conditions are then updated, and the decision to continue with the simulation or exit is made.

This flow chart clearly shows that the treatment of the interface conditions is just as explicit as the treatment of volumetric coupling from the scattering kernel.

4.4 Ballistic Comparison

To get an accurate comparison between the two methods, we first consider only ballistic transport in gray mediums. Choosing the ballistic limit eliminates COMET acceleration obtained due to more efficient treatment of bulk scattering, as described in [115]. Thus, solution acceleration due only to the interface treatment may be gauged. We consider several one-dimensional domains, as shown in Fig. (27). The number of interfaces is varied to examine its influence on convergence. The total number of cells in all three domains is set to 640. In keeping with a gray approximation, a spherical Brillouin zone is employed and discretized using spherical coordinates [99]. In the angular space, a discretization of N_θxN_ϕ=4x4 in the octant is used; here θ is the polar angle and ϕ is the azimuthal angle, as described in [115]. In these problems, only one multigrid level was needed to reach convergence in one iteration, or adding levels beyond 2 caused a slower time to convergence. Therefore we report timing for 1 level, but also show iteration count and total solution time for different multigrid levels. A standard V-cycle was used for all results [105].

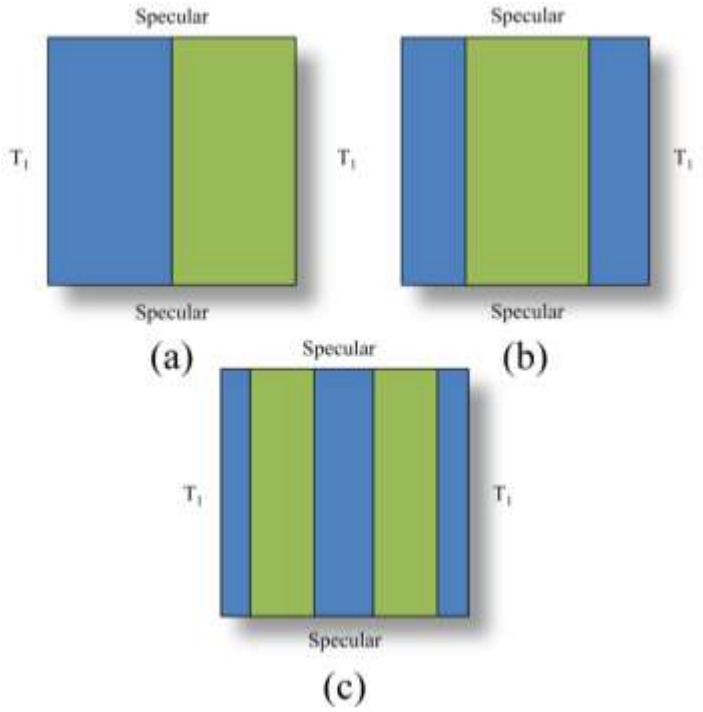

Figure 27: Different one dimensional domains used for comparison. The total number of cells for all three domains is 640.

For the following simulations, we assume a constant specific heat. The solution is initialized to T_i=301 K. The boundary conditions on the left and right are set at T_1=300 K. The solution is considered converged when the dimensionless temperature, defined as

$$\theta = \frac{T - T_1}{T_i - T_1} \tag{57}$$

falls below 10^{-6}. This criterion was used for both COMET and the sequential procedure.

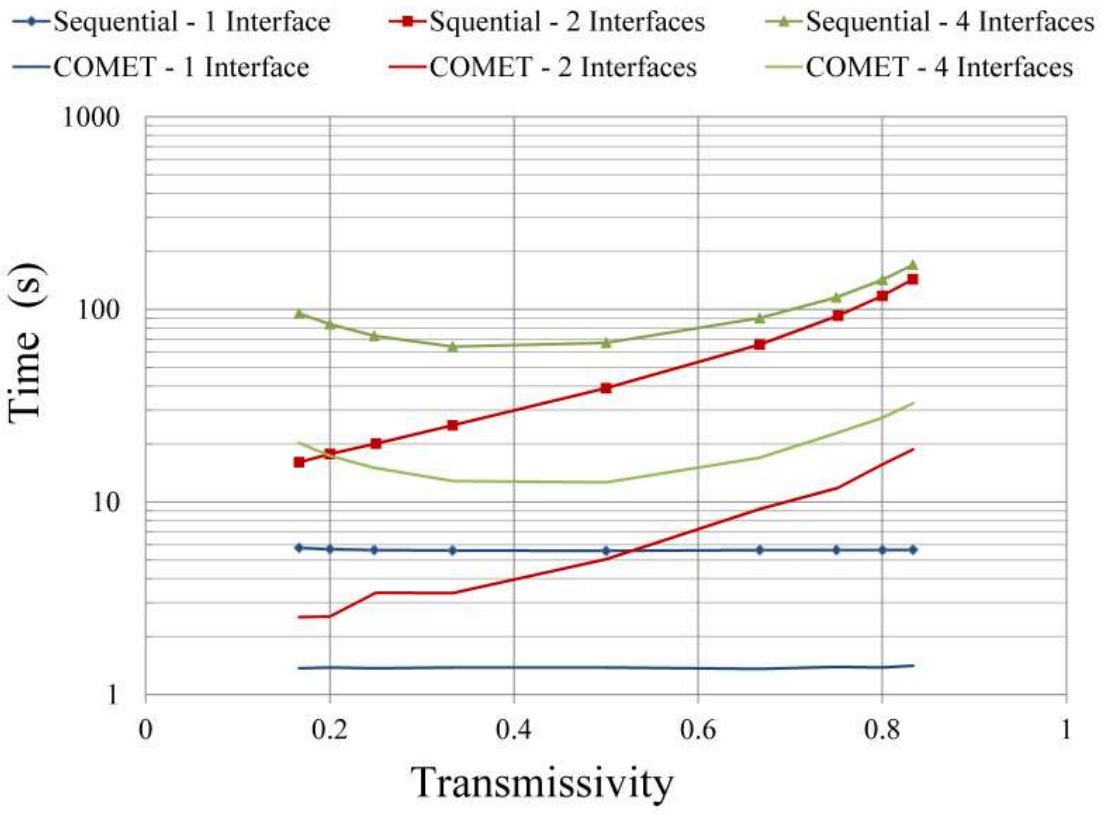

Figure 28: Total solution time for COMET and the sequential procedure for the domains pictured in Fig. (27).

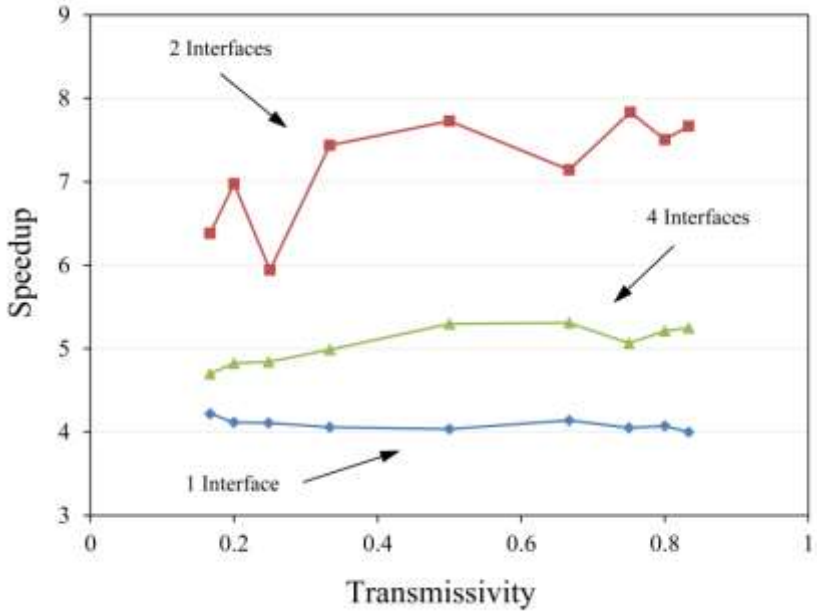

Figure 29: CPU Speedup of COMET over the sequential procedure attained for the domains shown in Fig. (27).

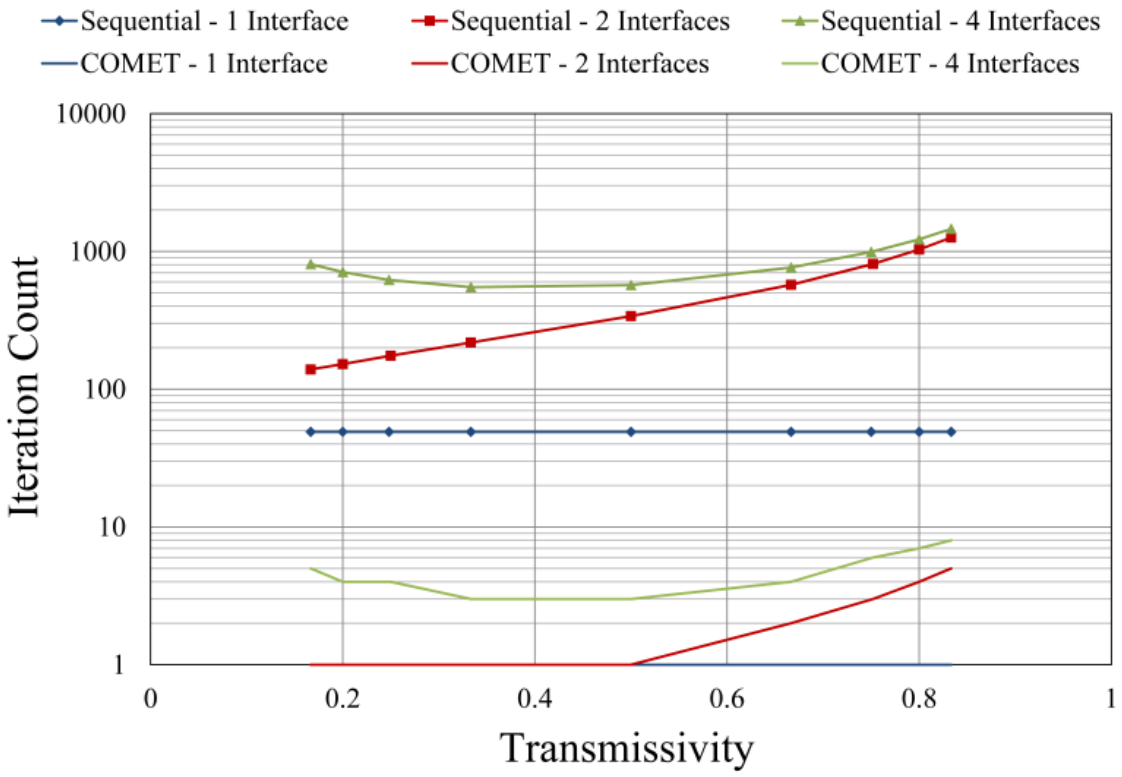

Figure 30: Iteration count for COMET and the sequential procedure as a function of transmissivity for the different domains pictured in Fig. (27).

Figures (28)-(30) summarize the results by showing the total solution time for COMET and the sequential procedure, the speedup in total solution time of COMET compared to the sequential procedure, and the iteration count for COMET and the sequential procedure, respectively, as a function of transmissivity for different number of interfaces. By eliminating spatial coupling, we can see that indeed, because of the implicit treatment at the interfaces, the COMET procedure outperforms the sequential procedure for all cases, delivering an acceleration factor in CPU time of 4-8. When only

one interface is in the domain (Fig (27a)), the sequential procedure performance is not hindered to a large degree. This is why we see the lowest speedup here. Adding a second interface hinders the sequential procedure more so because the middle material is completely isolated from a boundary. At four interfaces, the speedup drops to approximately 5, however. The reason pertains to the cost of computing the interface values. It was found that for Figs. (27b) and (27c), adding multigrid levels decreased the iteration count, but did not reduce the total compute time. Because this is a 1-dimensional domain, each interface represents 1 face. With this setup, it is not possible to reduce the number of interface faces for subsequent coarse levels, which leads to a higher cost per coarse level. A plot of the total solution time as a function of transmissivity for different multigrid levels is shown in Fig. (28). For one interface, the solution time increases because only one iteration is needed for the solution to converge with one level.

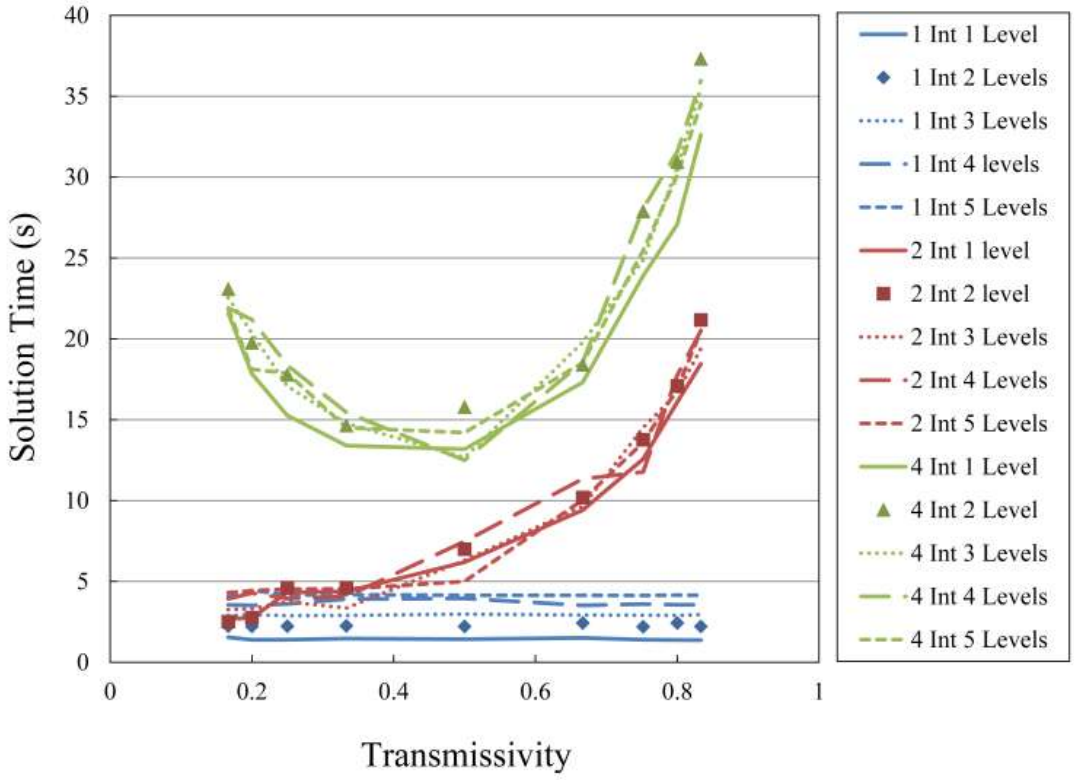

Figure 31: Total solution time taken for COMET as a function of transmissivity for varying domains pictured in Fig. (27) and different multigrid levels.

It should be noted that the domains pictured Fig. (27) represent the worst case scenario for convergence. This is because all phonons must be transmitted across the interface, and there are no pathways between the boundaries that do not encounter the interface. Thus the bottlenecks to convergence because of the interface treatment are the worst for this problem.

4.5 2-D Nano-composite – Gray

MESH DESCRIPTION

Next, we consider phonon transport in a two-dimensional particle composite, shown below.

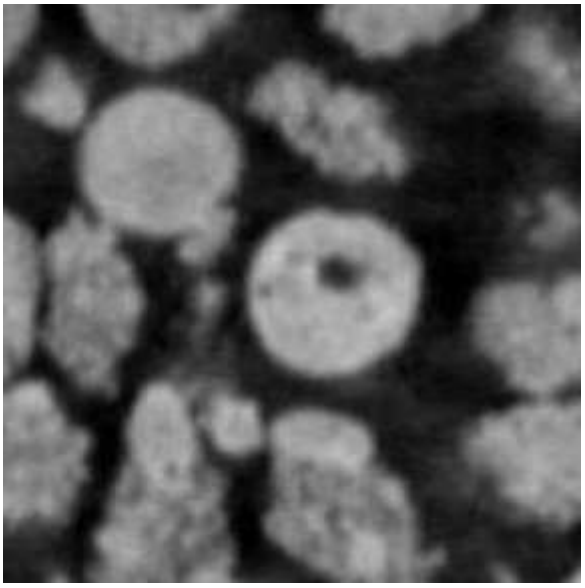

Figure 32: X-ray CT Scanned image of nanoparticle composite.

The actual composite consists of copper particles with air as a separator, used in heat pipe wicks. We employ this geometry to test our algorithm. The diameter of the particles in the composite is approximately 250 micrometers. The volume fraction of the particles (ratio of total particle volume to total volume) is 51.2%.

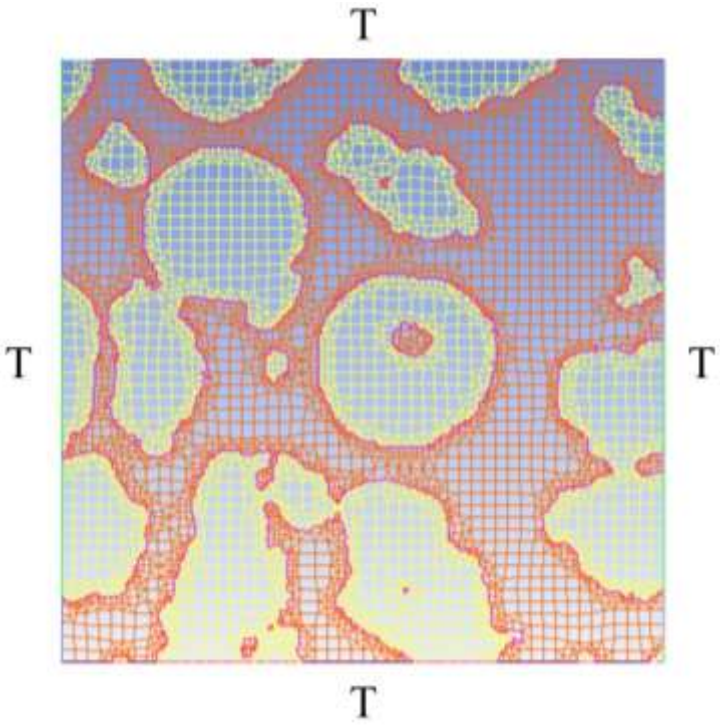

Figure 33: Mesh generated for image shown in Fig. (32).

The geometry of the particle composite is obtained as a 2D image using x-ray micro-CT scanning. Figure (32) shows a representative scan. The differential absorptivity of x-rays by different materials leads to difference in the grayscale intensities of the scanned image. The first step is to partition the image into different sub regions so that respective properties of the constituent materials can be assigned. This process is called segmentation and is carried out using the open source software package OOF2 [116]. OOF2 also has image processing capabilities like noise removal, thresholding, and downsampling that are used to process the image. Once the image is segmented, OOF2 can generate finite volume meshes. Figure (33) shows the finite volume mesh for the image shown in Fig. (32). The actual size of the image taken is 400x400 μm, but the

domain is scaled to obtain the desired Knudsen number. The mesh contains 8,194 finite volume cells; a mixture of quadrilaterals and triangles is used. Though the mesh was not created using an actual semiconducting nanoparticle composite, the image appears to have the same qualities as those shown in the literature [30,31].

We will first benchmark against the sequential procedure using a gray dispersion relation. Since this is a simple problem mean to simply benchmark our algorithm, we need only specify the domain Knudsen number and the transmissivities of the two materials. A T_1=300 K boundary condition on all walls will be used with an initial guess of T_i=301 K. The convergence criteria described in Eq. (57) will also be used for both COMET and the sequential procedure. After the method is benchmarked against the sequential procedure, we will examine the particle composite using realistic dispersions for silicon and germanium.

AGGLOMERATION CONSIDERATIONS

Strategies for agglomeration of interface faces play a critical role in convergence acceleration. As mentioned earlier, in creating coarse levels in the geometric multigrid procedure, in addition to agglomerating fine-level cells, fine-level interfaces in the mesh must be agglomerated as well, and the corresponding effective interface transmission operators created at each mesh level. To demonstrate the importance of this effective operator, we first consider a scenario in which, at each coarse level, no care is taken to preferentially agglomerate interface cells together. With this strategy, minimal interface agglomeration occurs at each coarse level, so that the number of interfaces at coarse levels does not decreases by the factor of two enforced on the volumetric cells. Thus, the

coarse-level interface faces impose a penalty on solution time which may overshadow the overall decrease in iteration count that the multigrid procedure can deliver.

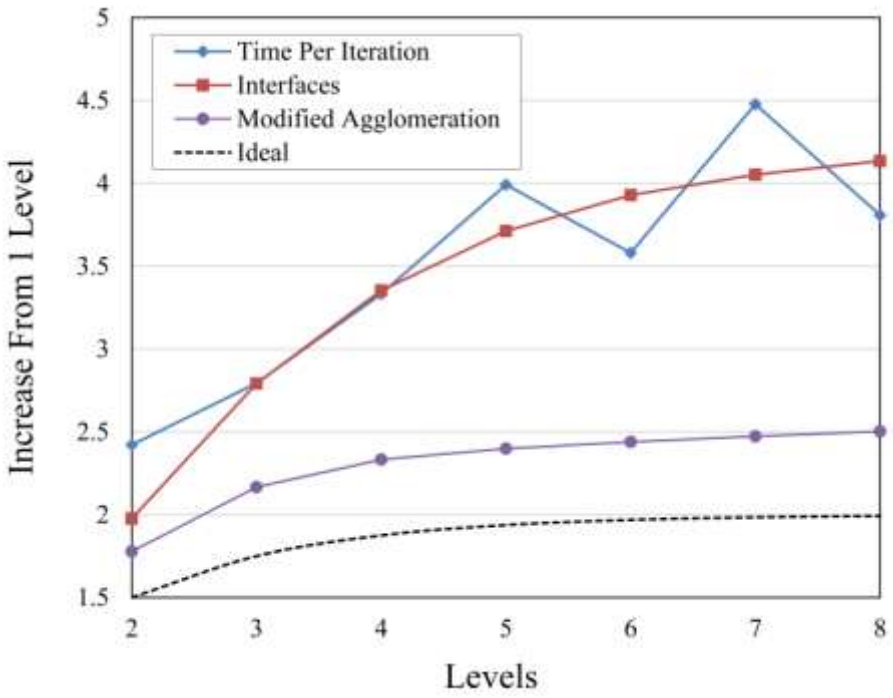

Figure 34: Increase in the time taken per COMET iteration and the increase in the number of total interfaces.

Figure (34) shows the increase in time per COMET iteration for each additional coarse level relative to a single fine level iteration. In the ideal scenario, the additional effort for each additional multigrid level should follow closely to the dashed line in Fig. (34). This line was found by assuming that an additional level carries an additional cost which is half that of the previous level. The red curve in Fig. (34) shows the additional number of *total* interface faces in the simulation (summation over all levels). The solid blue curve is the time per iteration of COMET. We can see that the solid blue and red

curves follow one another closely; COMET cost is dominated in this problem by the cost of interface computation, and thus scales approximately as the total number of interfaces summed over all mesh levels. Significant computational gains may be had by reducing the number of interface faces at the coarse mesh levels.

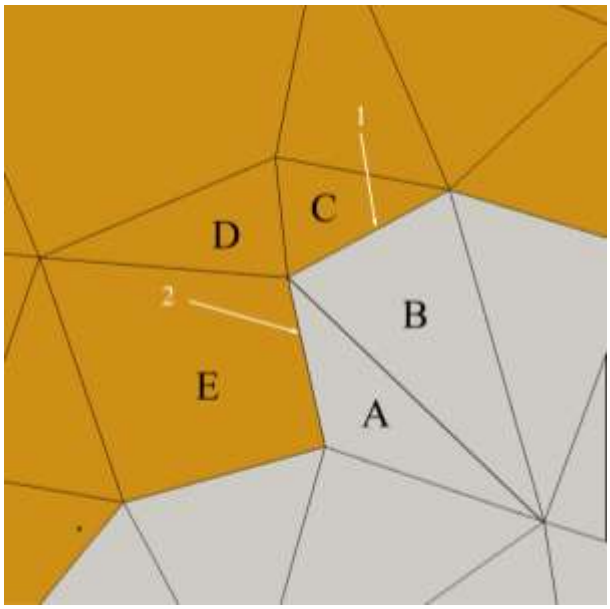

Figure 35: Close up of the mesh shown in Fig. (33) at an interface.

It was found that a successful agglomeration strategy must aggressively target interface faces to agglomerate before any interior cell agglomeration occurred. Of particular importance is the scenario pictured in Fig. (35). Here, the two different materials are shown, one in orange and one in gray. If cells A and B were chosen to be agglomerated together, in order to agglomerate faces 1 and 2 cells C, D, and E would need to have also been selected for agglomeration. This cannot be left to chance, so a

successful agglomeration strategy must also find "bridge" cells (cell D in this case) which would allow more interface agglomeration. We have explored heuristically a number of interface agglomeration strategies. One such strategy, which achieves face agglomeration by an approximate factor of two, is explored in Fig. (34). We see that the ideal number of total interface faces must saturate at two as the number of coarse levels increases (black dashed line). The modified agglomeration strategy (violet circles) does not quite achieve this ideal limit, but is substantially more effective than a random agglomeration strategy.

COMPARISON WITH SEQUENTIAL

For comparison with the sequential procedure we will again use a gray BTE and vary the transmissivity. In contrast to the previous problem, we will include the effect of volumetric scattering. We consider the particle mesh shown in Fig. (33), with 8,194 cells, and 1412 interface faces. The dimensionless parameters governing the problem are the domain Knudsen number, which is the mean free path divided by the domain length, the particle Knudsen number which is the mean free path divided by the largest particle size ($Kn_p \sim 3.4Kn$), and the interface transmissivity. We consider two domain Knudsen numbers, $Kn = 1$ and 10. Both materials will have the same Knudsen number (same group velocity and relaxation time), whereas we will change the specific heat to obtain the desired transmissivity. The interface transmissivity is varied and the performance of COMET is compared with that of the sequential procedure. We will continue to use the DMM, which allows us to specify one transmissivity.

The results of the comparison are summarized in Fig. (36). The dashed lines denote the acceleration obtained by COMET over the sequential procedure for a domain with no interfaces, but the same domain Knudsen number. We see that in the absence of interfaces, COMET outperforms the sequential solver for the lower Knudsen number (Kn=0.1), but incurs a performance penalty for Kn = 1.0, as discussed in the previous chapter. Here we seek to compare COMET performance with that of the sequential procedure in the presence of complex interfaces as in the particle composite in Fig. (33).

For the lower Knudsen number, Kn=0.1, we see that acceleration in CPU time is obtained using the COMET procedure for all transmissivities considered. COMET acceleration factors exceed those for the case with no interfaces. This is because interface coupling of phonons in $\boldsymbol{K}$ space is more effectively handled by the point-coupled nature of COMET. However, the acceleration factor obtained in the presence of interfaces depends on the interface transmissivity. For the higher Knudsen number, Kn=1.0, CPU time acceleration is not obtained for all transmissivities, but even so, better performance than the no-interface case is obtained in all cases.

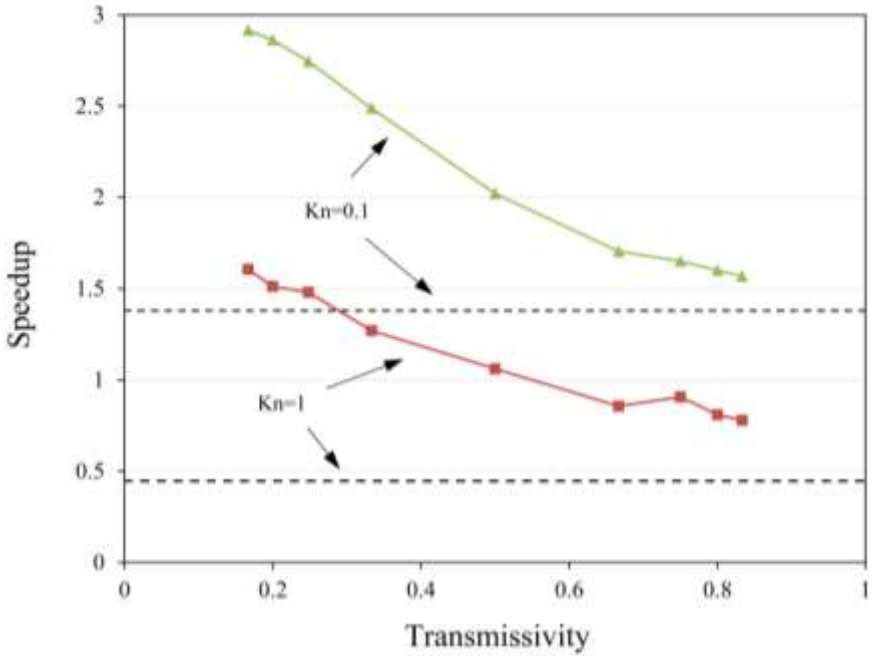

Figure 36: Speedup in CPU time attained for varying transmissivity and Knudsen number. Dashed lines represent speedup attained when no interface is present.

4.6 Closure

In this chapter, COMET was extended to include phonon transport across complex heterogeneous interfaces. COMET was compared against the sequential procedure for three ballistic test cases. These test cases illuminated COMET's ability to effectively couple phonon groups at the interface. We then used CT scans of a copper particle bed to create a realistic computational domain to benchmark our results. By including volumetric scattering, it was shown that for a range of transmissivities solution acceleration was attained with the inclusion of interfaces for bulk Knudsen numbers which previously did not see solution acceleration.

The following chapter will utilize COMET's ability to resolve complex material interfaces to analyze phonon transport through realistic nanoparticle composites. Realistic dispersion relations are used to extract frequency, and mean free path dependent transport.

5. *K*-RESOLVED TRANSPORT IN A 2-D NANO-COMPOSITE

In this chapter we use COMET to examine phonon transport in geometrically realistic nanoparticle composites using realistic dispersion relations for silicon and germanium. The contributions of the different phonon groups are analyzed as a function of temperature and particle size.

Because of their simplicity, periodic nanocomposites have received a lot of attention in the literature. Chen [117] predicted the thermal conductivity of periodic thin films in the direction parallel to the films. This paper also found that resolving frequency dependent phonon properties, as opposed to assuming gray transport, achieved results closer to experiment. Yang and Chen [118] simulate phonon transport in 2-dimensional periodic nanocomposites using a gray dispersion relation for silicon and germanium and a deterministic solution procedure. Later a Monte Carlo method was developed and used to simulate phonon transport in particle composites [81,119]. In both papers, a gray dispersion relation was used to model the material properties. In [81], 3-dimensional periodic structures were simulated. Random particle disbursement was approximated by randomly placing particles within a periodic cell. In [119], Tian and Yang used the same code was used to simulate compacted nanowire composites, whereby the composite was simplified as a periodic arrangement of nanowires imbedded in a host matrix. Tian and Yang, again with the same code, randomly positioning nanowires in a square lattice for different nanowire sizes to study the effect of phonon percolation in composite materials [120]. Hsieh and Yang [121] examined the effect of the nanowire shape in period nanowire composites by developing a solver for the gray phonon BTE. Singh, *et al.* used

a finite volume solution to the non-gray BTE to study the effects of dispersion on silicon/germanium interfaces for a variety of 2-dimensional domains [114].

The previous work on modeling phonon transport in nanocomposites makes at least one of two simplifications: on geometry, or on dispersion. The first simplification involves an abstraction of the realistic geometry. In the case of periodic superlattices, this simplification poses no threat to the fidelity of the results. However, realistic domains have yet to be simulated which are not periodic. The second simplification comes as an approximation of the dispersion relations of the constituent materials, generally via gray phonon transport. In ballistic and diffusive regimes, this approximation can give meaningful results. However, in intermediate domain sizes frequency dependent behavior becomes important [122].

In this chapter, phonon transport will be simulated using realistic phonon dispersion relations and realistic nanoparticle composite geometry. Two domains are used to represent the nanoparticle composite: that which was used in the previous chapter, as well as a larger domain with similar particle size. The particle size is chosen to mimic those found in already fabricated nanocomposites [30,123]. We therefore use domain sizes of 316 nm and 850 nm (sometimes referred to as the small domain and the large domain, respectively). In addition, several auxiliary domains will be simulated to give context to the nanoparticle composites. These are: single material silicon, single material germanium, a Si-Ge composite with a single vertical interface, and nanoporous silicon. More details about these domains are given later.

5.1 Simulation Details

BRILLOUIN ZONE AND TRANSMISSIVITY

The dispersion relation and relaxation times for silicon are those which have already been mentioned in Chapter 3. For germanium, we used the Harrison potential [124] to obtain the dispersion relation. The same functional form used in the silicon relaxation time is also used in germanium and curve fit to data [125], where the constants A, B, and C are $2.4\text{x}10^{-44}$ s^3, $3.35\text{x}10^{-19}$ s/K, and 57.6 K, respectively. The Brillouin zone for both materials is assumed isotropic with a discretization of $N_\theta \text{x} N_\phi \text{x} N_k$ = 2x2x8 in the octant. The $\boldsymbol{K}$-space coordinates are oriented with $\boldsymbol{K}_x$, $\boldsymbol{K}_y$, and $\boldsymbol{K}_z$ along the x, y, and z spatial coordinate axis. We use the DMM to calculate the transmissivities. Four equally space frequency bins, which span from 0 rad/sec to the germanium cutoff frequency of 5.65 x 10^{13} rad/sec are used, as well as a single frequency bin above the germanium cutoff frequency to the silicon cutoff frequency of 1.03 x 10^{14} rad/sec. The calculated transmissivities from silicon to germanium are shown in Table 4.

Table 4: Transmissivities for the frequency bands used in the nanocomposites simulation.

	Band 1	Band 2	Band 3	Band 4	Band 5
Transmis-sivity	0.774	0.359	0.86	0.382	0

AUXILIARY DOMAINS

The geometry of the nanoparticle composites that are simulated in this chapter are rather complex. In an effort to contextualize the results of these simulations, we use several other domains for comparison. The first domain is pictured below.

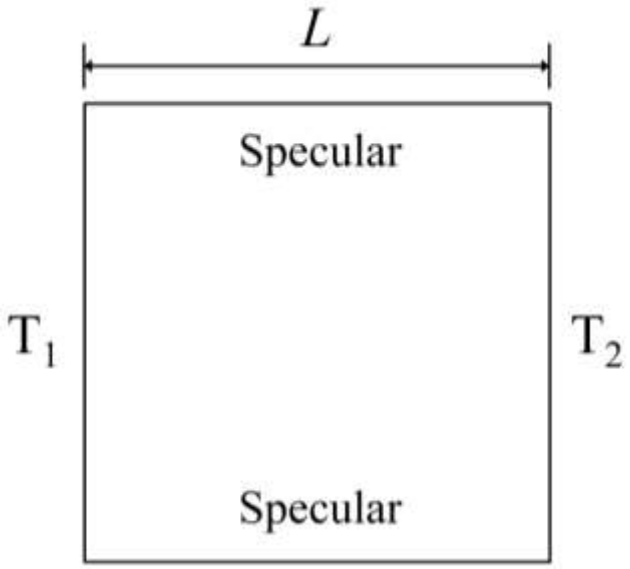

Figure 37: One dimensional domain for a single material simulation. This domain is used for simulating transport in silicon and germanium for both small and large domain sizes.

The above domain simulates one dimensional phonon transport along a finite length. Because the thermal conductivity scales with the length of the domain, this simulation puts in to context the reduction of thermal conductivity due to the length scale. Both silicon and germanium are simulated using this domain.

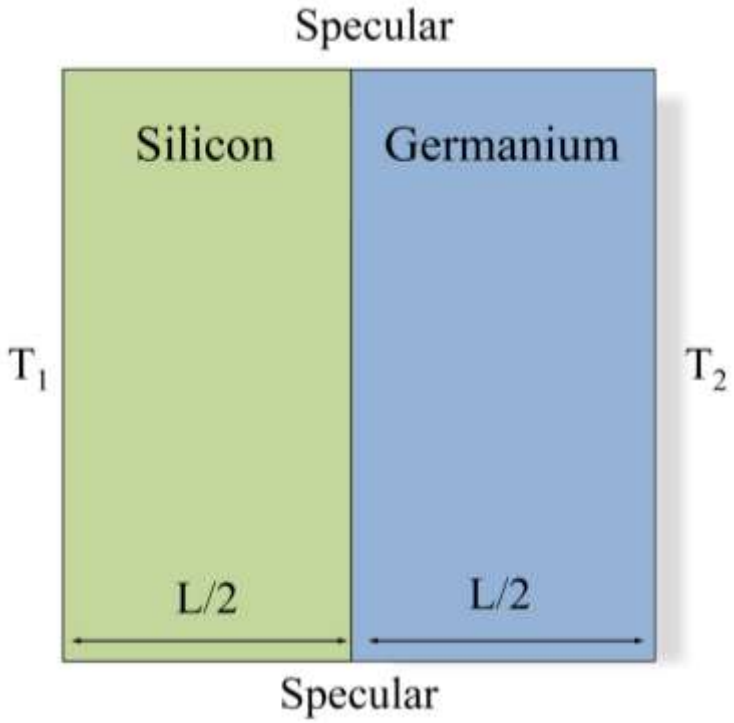

Figure 38: One dimensional domain with a single Si-Ge interface. This is used in both the small and large domains.

Pictured above is the second auxiliary domain. It consists of one dimensional phonon transport across a single Si-Ge interface. This geometry gives us a simplistic view of phonon transport with the inclusion of an interface. With the interface, we have effectively reduced the limiting length scale to L/2, the effects of which will be discussed later. In addition, a phonon travelling through this domain is guaranteed to encounter an interface. That is to say, there is no possible path from one boundary to the other which does not cross an interface.

The final auxiliary domain is exactly the same as that of the composite, with the exception that germanium is be replaced with a vacuum. In effect, this creates nanoporous silicon. From this domain, we will establish the lower limit of the thermal conductivity, for the given geometry. This is because all of the interfaces are replaced

with diffusely reflecting walls, which is identical to a transmissivity of 0 from silicon to germanium.

KNUDSEN NUMBER CALCULATION

In Chapter 2, we discussed the relevant dimensionless parameters. Of particular importance is the Knudsen number, which is defined as the phonon mean free path divided by the characteristic length of the domain. It is therefore important to establish what length we are using to calculate the Knudsen number for these complex geometries.

The fundamental understanding gained from the Knudsen number is the ratio of the intrinsic crystal mean free path (three-phonon scattering), and the geometrically limiting distance. In this thesis, we will interpret the geometrically limiting distance in the following ways. For the single material domain, the entire domain length is used as the characteristic length of the domain. In the single interface domain, half of the total domain length is used as the limiting distance. The nanoparticle composite and the nanoporous silicon will use the same limiting distance. This is because we attempt maintain the same average particle size of roughly 90 nm for both the large and small domain sizes. We therefore will use a limiting domain length of 90 nm for the nanoporous silicon and the nanoparticle composite for both the large and small domain sizes.

THERMAL CONDUCTIVITY ANALYSIS

To calculate the thermal conductivity of all the aforementioned domains, we will apply a 1 K temperature difference. The calculated the flux at the end of the simulation is used in the following equation for the thermal conductivity:

$$K_{eff} = \frac{q''L}{\Delta TA} \tag{58}$$

Here, q'' is the calculated heat flux, ΔT is the temperature difference (1 K), L is the domain length, and A is the area which is calculated by assuming a length of unity in the direction into the paper.

At the boundaries of the nanoparticle composite, there is energy entering/exiting the domain via both silicon and germanium. To help our analysis, we will present all of the frequency and mean free path dependent data in terms of the normalized heat rate for the individual materials. In Particular, these data will be presented as the normalized accumulation of the heat rate on the right boundary.

5.2 Small Domain Size

The realistic nanoparticle composite that was used in the previous chapter is also used here. Because we are primarily interested in transport through the composite, the boundary conditions are modified and shown in Fig. (39). This is referred to as the small domain size.

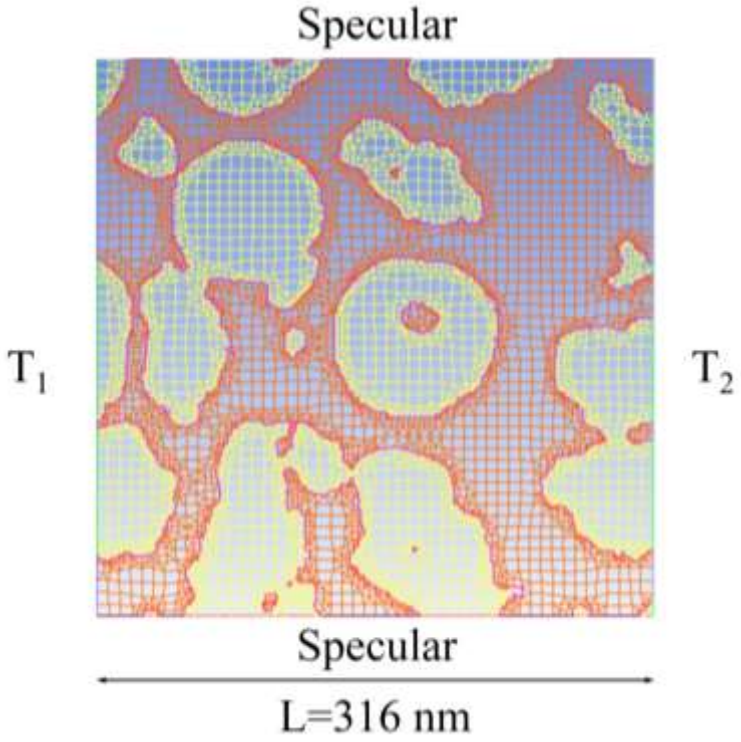

Figure 39: Simulation domain for the small domain size nanoparticle composite.

The domain is scaled to a length of 316 nm, which gives a particle size of approximately 90 nm.

Figure (40) shows a plot of the thermal conductivity for the nanoparticle composite as well as the auxiliary domains, all of which have the same domain length of 316 nm.

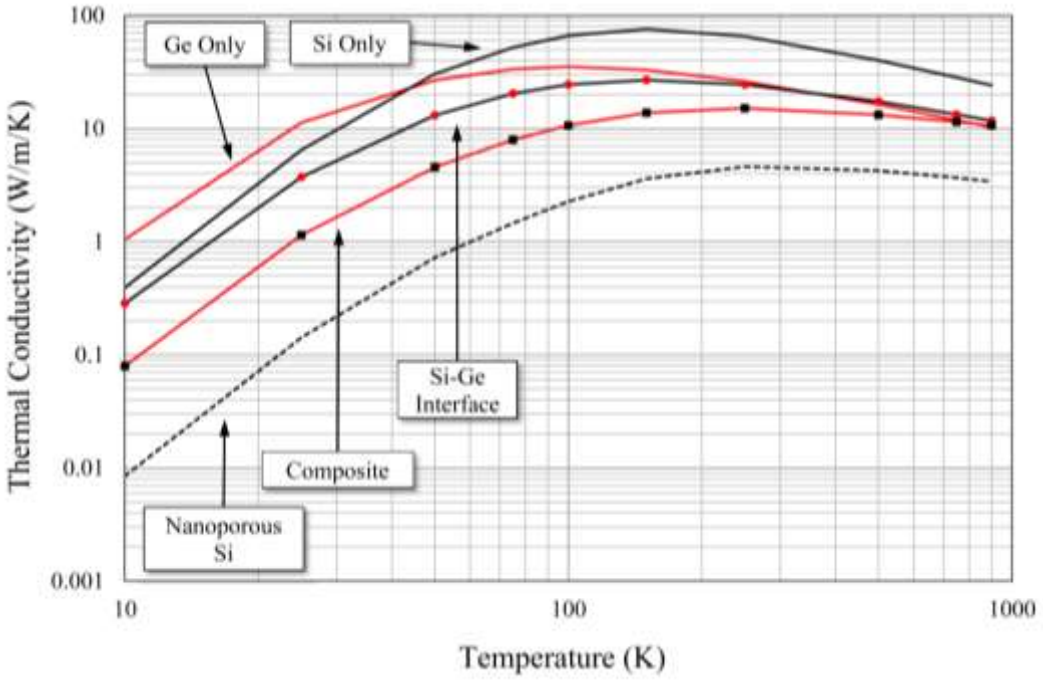

Figure 40: Thermal conductivity as a function of temperature for the domains listed above with a domain length of 316 nm.

In the single material domain for germanium and silicon, we see an increase in thermal conductivity at low temperatures. The increase occurs because the intrinsic phonon mean free path is much larger than the domain size. In this regime, an increase in temperature serves to only increase the amount of phonons which are activated. At low temperatures, phonon-phonon scattering is not prevalent enough to reduce the hinder conduction. As the temperature increases further, a maximum thermal conductivity is reached. Once the maximum is reached, this implies that phonon-phonon scattering is occurring enough to counter the increasing phonon population with increasing temperature. Past the temperature at which the maximum thermal conductivity occurs, we see a decrease in the thermal conductivity. It is important to note that the maximum temperature in only germanium and only silicon occurs at a larger temperature than in

their bulk counterparts [125]. This is because the small domain length of 316 nm delays the onset of substantial phonon-phonon scattering within the domain, whereas in a bulk material the domain is much larger.

In the domain with a single interface we see a similar trend. There is an increase in the thermal conductivity as the temperature is increased corresponding to more phonons being activated without substantial phonon-phonon scattering occurring in the domain. The peak in the thermal conductivity occurs after that of germanium, and roughly at the same temperature as silicon. This indicates that by introducing an interface, we delay the onset substantial phonon-phonon scattering on the germanium side of the interface. Once the germanium side of the interface experiences sufficient enough phonon-phonon scattering to begin to impede heat flow we begin to see a decrease in the thermal conductivity.

The nanoparticle composite shows similar, albeit flatter behavior. When the temperature is increased, the onset of the maximum thermal conductivity occurs at a temperature higher than that of the three previous scenarios. This occurs because interface scattering is the dominant scattering mechanism for a larger temperature range. The effective mean free path due to the interface density is much smaller than the intrinsic mean free path of the crystal. Though the peak is at a higher temperature than that of the single interface domain, the amount by which is not substantial. This is because the limiting domain length in the single material is 158 nm which is very close to the limiting domain length in the nanoparticle composite of 90 nm.

As mentioned earlier, the nanoporous silicon is expected to produce the lowest values of thermal conductivity for all temperatures. This is seen to be true. By replacing the interfaces between silicon and germanium with diffusely reflecting walls, we are effectively replacing germanium with a non-conducting material. Where phonon energy

may have been partially transmitted in the nanocomposite, it is entirely reflected in nanoporous silicon.

We further examine the relationship between the nanocomposite and nanoporous silicon in Fig. (41), where we have plotted the ratio of their conductivities.

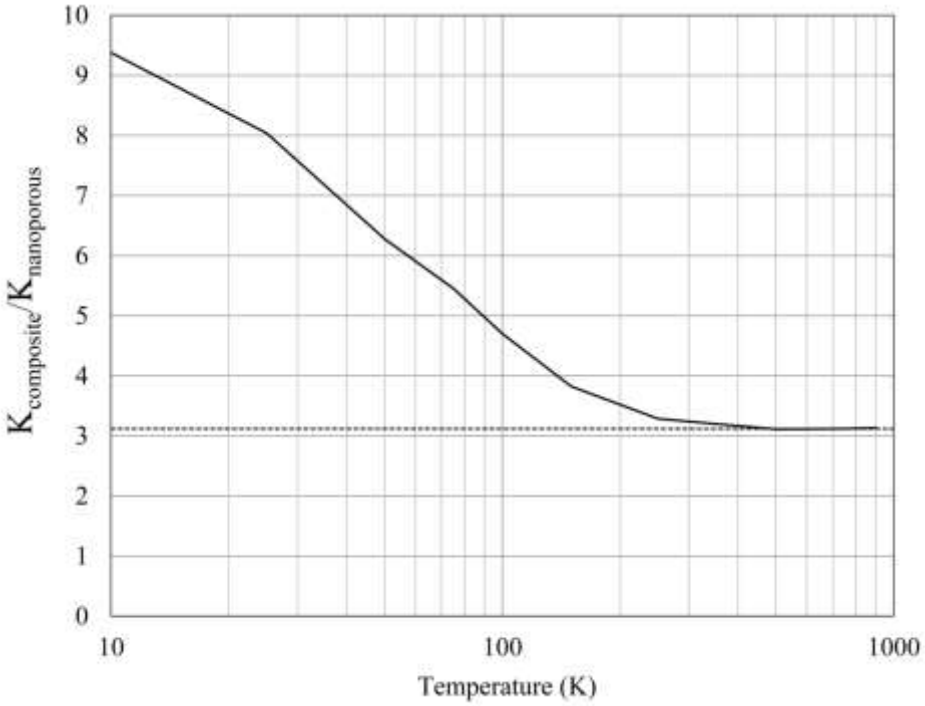

Figure 41: A plot of the composite conductivity divided by the nanoporous silicon conductivity as a function of temperature.

For low temperatures, the conductivity of the composite is about 10 times larger than that of nanoporous silicon. As the temperature increases, this factor decreases and eventually asymptotes to approximately 3 times the nanoporous silicon value. The reason for this trend may be found by examining the frequency signature of the heat rate on a boundary of the domain, shown in Fig. (42). Since the boundary has both silicon and germanium, we will look at the normalized cumulative heat rate as a function of frequency, whereby each material is normalized by its individual heat rate. Therefore, all

of the curves terminate at a value of unity. It was found that these curves did not change significantly when looking at the left boundary versus the right boundary.

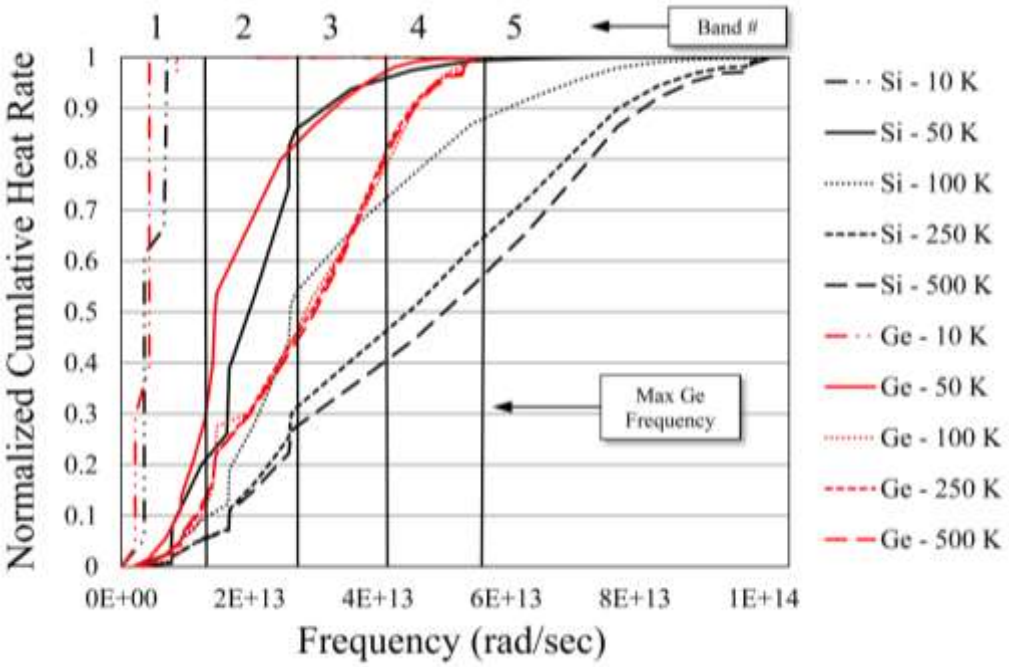

Figure 42: Normalized cumulative heat rate of silicon and germanium in the nanocomposite as a function of temperature. Each material's heat rate is normalized by its own contribution to the total heat rate. Horizontal lines represent frequency bins where transmission coefficients are calculated.

As mentioned before, the thermal conductivity of nanoporous silicon is the lowest possible value in a nanoparticle composite of a given matrix material; it is as if the transmissivity from the matrix to the particle were zero. In the nanoparticle composite, the transmissivity from silicon to germanium is zero for all frequencies above the germanium cutoff frequency. This suggests that the more phonons in band 5 that contribute to conduction, the more like nanoporous silicon the composite becomes. From the graph above, we can see that at 10 K, 100% of the heat rate in silicon is carried by phonons of frequency below the germanium cutoff. Moreover, nearly all phonons at this

temperature are in the first frequency band; this band has a very high transmissivity, approximately 0.77, and thus has the largest difference with respect to nanoporous silicon. As the temperature increases, the spectrum of participating phonons increases, spilling into other bands. In germanium, the heat rate accumulation function remains relatively invariant after roughly 100 K. This is because the material has a smaller overall frequency range and therefore does not require a large temperature to activate all phonon modes. In contrast, the spectrum of contributing frequencies in silicon continues to broaden beyond 100 K. In particular, band 5 contributes about 12% of the heat rate at 100 K, and increases its contribution to about 42% at 500 K. Beyond 500 K, the frequency signature does not change noticeably, which is expected as this is approaching the Debye temperature (660 K) in silicon. Since the frequency signature in silicon remains approximately fixed after 500 K, the ratio between the nanoporous silicon and the composite remains fixed.

In the nanocomposite, we can further examine the onset of intrinsic scattering. To do this, we show a plot of the normalized accumulation of the heat rate at the left boundary as a function of the effective mean free path. The effective mean free path is defined as [35]:

$$\lambda_{eff} = \frac{\lambda}{1 + \frac{4}{3}\left(\frac{\lambda}{L}\right)} \tag{59}$$

Here the length, L, being used is the average particle length of 90 nm. As in Fig. (42), we look at the normalized heat rate of silicon and germanium whereby each material is normalized by its own individual heat rate. At the lowest temperature, the mean free paths contributing to heat flow are those limited only by the particle length. As the

temperature increases, the range of mean free paths contributing increases. When the temperature reaches 500 K, roughly 90% of the heat flow in silicon and roughly 95% of the heat flow in germanium is from phonons with an effective mean free path below that which corresponds to a Knudsen number of 0.5. With this, it is safe to assume that volumetric scattering is a very large contributor to overall scattering above 500 K. In this regime, the composites begin to act in more of a volume averaged sense. In Fig. (40), the thermal conductivity of germanium falls below the Si-Ge single interface domain at approximately 400 K and falls slightly below the composite at 900 K. This is because in the Si-Ge single interface, the limiting length scale is large enough at 400 K that we begin to see a thermal conductivity value which is expected in the Fourier limit, which is a harmonic average of the silicon and germanium conductivities. In the composite, there are much more interfaces which hinders the onset of volumetric behavior much longer.

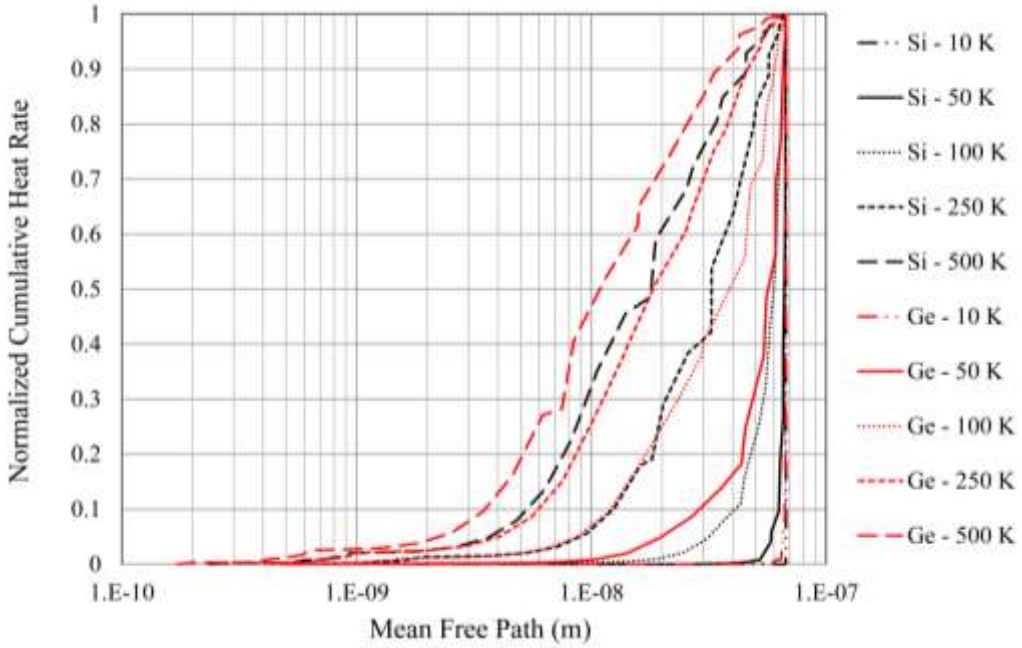

Figure 43: Normalized cumulative heat rate as a function of the effective phonon mean free path. Each material is normalized by their individual contribution to the total heat rate, making all curves terminate at 1.

5.3 Large Domain Size

We now discuss phonon transport in a larger square domain of side 850 nm, but with approximately the same particle size as the sample used in the previous section. The same procedure that was used to produce the mesh created in the previous section is used here.

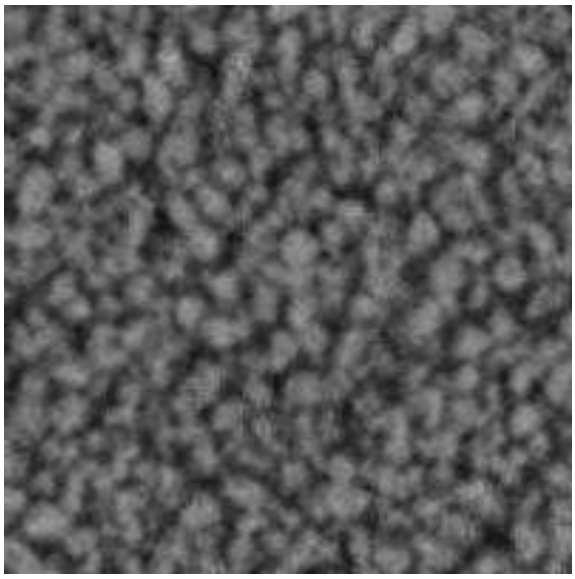

Figure 44: CT scan of a particulate nanocomposite for domain size of 850 nm.

The mesh that was generated from the above scan is shown below. A total of 19,568 cells are used with 5,517 interface faces. The same boundary conditions which were used in the previous section are also used here.

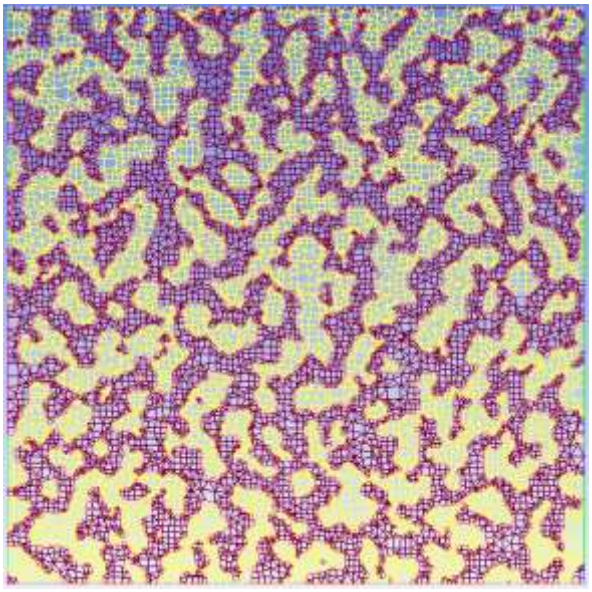

Figure 45: Mesh created from the scan in Fig. (44). The mesh contains 19,568 cells and 5,517 interface faces. The volume fraction is 50.5%. For all simulations the red cells are silicon and the yellow cells are germanium.

In Fig. (46) we show the thermal conductivity as a function of temperature. We can see the same trends which were observed in the previous section. The single material domains show a higher conductivity that that of the small domain at low temperatures. This is because the conductivity is proportional to the domain length in the ballistic regime. Also in the large domain, we see a slight shift to the left of the peak conductivity, indicating an earlier onset of extensive phonon-phonon scattering. The single interface domain also experiences higher conductivity than the small domain as well as an earlier peak in the conductivity. For these simplistic domains, the earlier onset of the peak conductivity points to a move toward bulk behavior.

The peak conductivity for the composite occurs at the same temperature, which is expected because the critical length (i. e., particle size) is approximately the same. With this very similar trend, we can infer that bulk like behavior is attained even at such small domain sizes because of extensive interface scattering. As we saw with in the small

domain, at high temperatures when the frequency signature becomes fixed, the composite takes the same shape as the nanoporous silicon. We also see the same trend for the large domain size. The conductivity curve of the nanocomposite is nearly identical in shape to the previous section. However, the conductivity is slightly lower at the peak for this domain size, 11.85 W/m/K as opposed to 15.12 W/m/K. This is contrary to the typical behavior of thin films whereby the conductivity should increase with increasing domain size. Though an attempt was made to keep the approximate particle size the same for both domains, slight differences in the interface density caused this discrepancy.

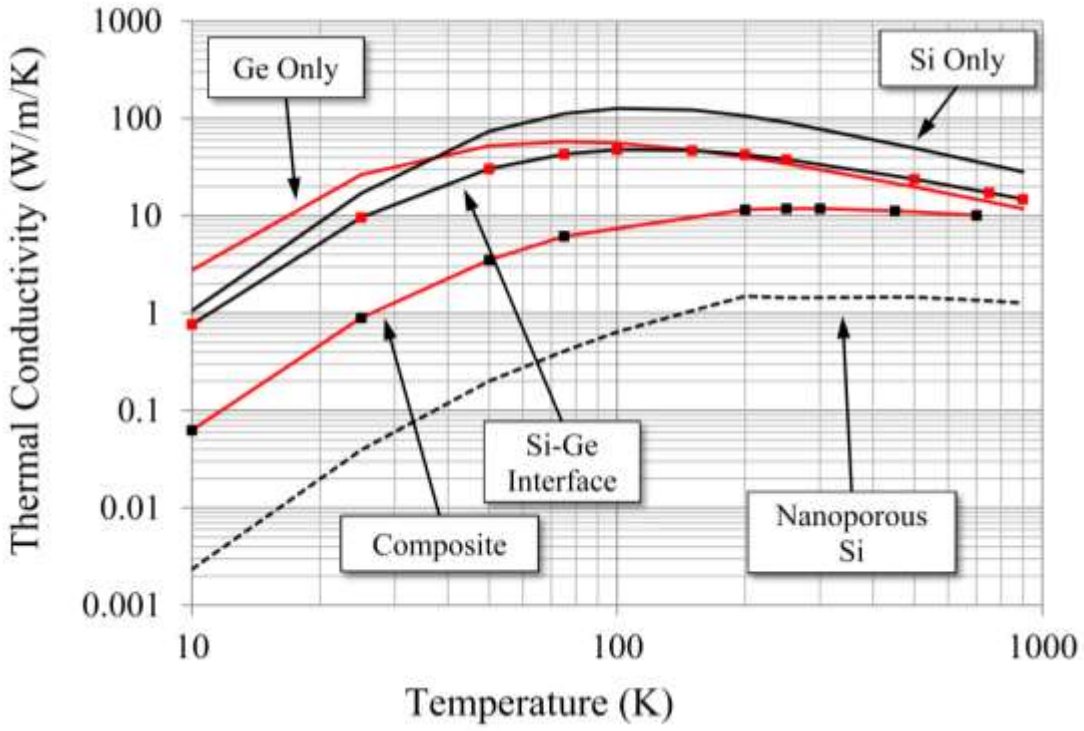

Figure 46: Thermal conductivity as a function of temperature for the large domain nanoparticle composite and the auxiliary domains with a length of 850 nm.

We have established that at low temperatures, the main scattering mechanism is that due to interfaces. It is therefore logical to conjecture that the strength of scattering

depends on the interface area per unit volume: essentially, we may view the composite as a bulk medium with a volumetric scattering rate proportional to the interface surface area per unit volume. From this perspective, the corresponding characteristic length scale is the ratio of the total volume of the domain to the interface surface area. This ratio essentially gives the distance a phonon travels, for a given volume, before it scatters with an interface. In this sense, it is analogous to the phonon mean free path used in kinetic theory. The mesh used in the previous section has a ratio of 27 nm whereas the mesh in this section has a ratio of 20 nm. The effect of this difference strongly evidenced in Fig. (47) where the conductivity of the composite at both domain sizes is plotted. Also on Fig. (47) is the curve $K(T)=K(T)_{850nm}*\lambda_{316nm}/\lambda_{850nm}$, where K is the conductivity plotted by the dashed line, $K(T)_{850nm}$ is the conductivity of the 850 nm domain, and λ_{850nm} and λ_{316nm} are volume divided by the interface surface area for the 850 nm and 316 nm domain, respectively. The conductivity of the dashed line lies nearly on top of the conductivity calculated for the domain at 316 nm. From kinetic theory, the conductivity of a phonon is given by the following:

$$K = \frac{1}{3} C v \lambda \tag{60}$$

C is the phonon specific heat and v is the phonon group velocity. λ is the phonon mean free path, which, for ballistic transport in the composite, is the total volume divided by the interface surface area. A deviation occurs at higher temperatures because the interfaces are no longer the major contributor to phonon scattering. In fact, this deviation occurs at the peak value for the thermal conductivity when the volumetric scattering begins to decrease the thermal conductivity.

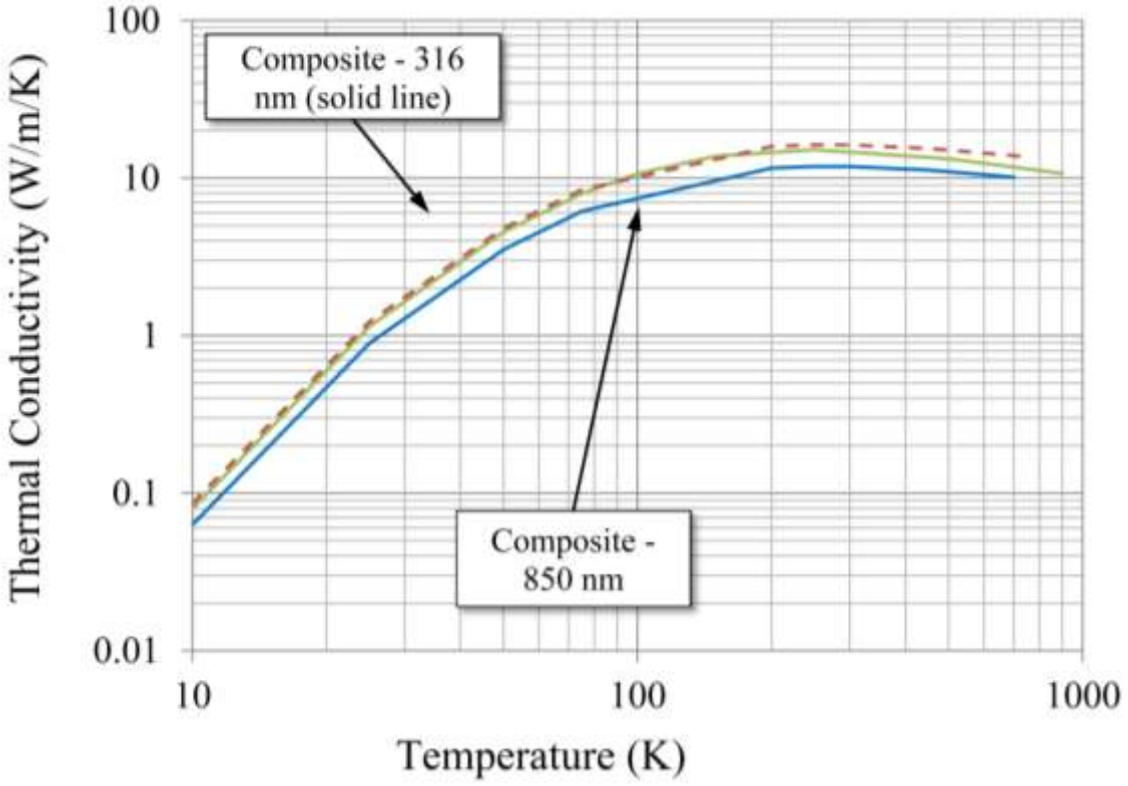

Figure 47: Conductivity of the 316 nm composite and the 850 nm composite (solid lines) and the conductivity of the 850 nm composite multiplied by the ratio of the surface to volume ratios for the two domains.

5.4 Closure

In this chapter we utilized COMET to analyze phonon transport in nanoparticle composites. To gain a better understanding of the competing physics, concurrent simulations of more simplified geometries were also performed. These geometries included one dimensional phonon transport in silicon and germanium, one dimensional phonon transport in a domain with a single Si-Ge interface, and nanoporous silicon. In addition, two domain lengths were used: 316 nm and 850 nm.

From our analysis, it was seen that by shrinking the length of the domain for a single material can cause a shift in the maximum thermal conductivity to higher

temperatures. This effect is also seen for the single interface domain. However, for the nanoparticle composites, the maximum thermal conductivity remained at the same temperature. From this we can deduce that with enough interfaces, interfacial scattering remains dominant regardless of domain size. In this sense, we may understand this scattering analogous to volumetric scattering. The length scale associated with this volumetric scattering is proportional to the interfacial density.

6. SUMMARY AND FUTURE WORK

In this chapter, we summarize the main contributions of the thesis and make suggestions for future work.

6.1 Main Contributions of the Thesis

The central focus of this thesis is the development of efficient computational methods to simulate micro- and nanoscale thermal transport in semi-conductors and dielectrics. These methods are critical to analyzing, understanding and optimizing micro and nanodevices with applications in microelectronics and energy conversion. A particle approach to phonon transport was adopted, whereby phonon wave effects were ignored and phonons were treated as discrete particles. In this limit, the phonon Boltzmann transport equation is a useful framework within which sub-micron heat conduction can be analyzed.

This thesis developed a new method for solving the phonon Boltzmann transport equation under the relaxation time approximation. The method, named COMET, showed excellent convergence rates on a large range of Knudsen numbers by introducing a point coupled solution procedure in tandem with a geometric multigrid. By doing this, the strong coupling in wave vector space and physical space was addressed in a more efficient manner when compared to the conventional sequential solution procedure. For Knudsen numbers greater than unity, COMET was found to outperform the sequential procedure by as much as 60 times for gray problems, and 233 times for non-gray problems. It was found that at high Knudsen numbers, the sequential solution procedure

outperformed COMET. However, such simulations take a relatively short amount of time and are not the main bottle neck for simulating phonon transport. COMET was parallelized using domain decomposition and was shown to have excellent scaling or parallel platforms even for modest spatial domain sizes.

COMET was then extended to include phonon transport across material interfaces. To do this, a generic interface operator was introduced which projects phonon energy density from one wave vector space to another, as would occur during reflection and transmission at an interface. The diffuse mismatch model was used at the interfaces, though other models for interface transmissivity are easily accommodated by the algorithm. It was found that interface face agglomeration was a substantial bottle neck in the computation and therefore an effective interface agglomeration strategy was derived to optimize the number of interface faces during multigrid agglomeration. With the inclusion of interfaces, COMET was seen to speed up over the sequential procedure computations even for Knudsen numbers greater than unity; this emphasizes the difficulty sequential procedures have in addressing interface transport.

To demonstrate the utility of COMET, phonon transport was analyzed in 2-D nanoparticle composite materials made of silicon and germanium. It was found that as the temperature approaches the Debye temperature in silicon roughly half of the thermal conductivity in silicon can be attributed to phonons at frequency greater that the cutoff frequency in germanium. This leads to a thermal conductivity which is close to that of nanoporous silicon (the same nanocomposite, but with vacuum instead of germanium) which is the lower limit for thermal conductivity in the given geometry. By comparing

the nanoparticle composite with nanoporous silicon, we developed a quantitative way to capture the effectiveness of a particular material combination in reducing the thermal conductivity of the composite. The results suggest that an ideal combination of materials for reducing the lattice conductivity of a composite would have very dissimilar Debye temperatures and very dissimilar cutoff frequencies. It was also found that the overall size of the nanoparticle composite has little effect on the conductivity. This is due to the substantial effect that interfaces have in reducing the thermal conductivity. We showed that the major determining factor for the reduction of thermal conductivity is the volume to surface area ratio. This ratio can be thought of as a distance per unit volume that a phonon must travel to scatter on an interface. Kinetic theory was used to explain the difference in thermal conductivity between domains with interface surface area per unit volume.

6.2 Future Work

A number of interesting directions may be pursued in the future to extend the work done in this thesis. These are described below.

SCATTERING KERNEL

The COMET algorithm developed in this thesis assumed that phonon scattering could be described by the relaxation time approximation. For three dimensional materials, this approximation is acceptable. Lower dimensional materials, because of the increased importance of Normal scattering events, require the use of the full scattering kernel to produce accurate results [76]. With the recent interest in lower dimensional

materials such as graphene, incorporating the full scattering kernel is necessary if COMET is to be a valuable simulation tool.

The full scattering term for three-phonon interactions is given as the summation of energy gained or lost from type I scattering events and type II scattering events. These source terms are defined as follows:

$$\dot{E}_I = \frac{\Omega\omega}{4\hbar\pi^2}\int f f'\left(f''+1\right)\left|\Phi_{\boldsymbol{K},\boldsymbol{K}'\to\boldsymbol{K}''}\right|^2\left|\boldsymbol{v}_n'\right|^{-1} dS_{\boldsymbol{K}'}$$
$$\dot{E}_{II} = \frac{\Omega\omega}{4\hbar\pi^2}\int\left(f+1\right)\left(f'+1\right)f''\left|\Phi_{\boldsymbol{K}''\to\boldsymbol{K}',\boldsymbol{K}}\right|^2\left|\boldsymbol{v}_n''\right|^{-1} dS_{\boldsymbol{K}''} \quad (61)$$

Here, Ω is the volume of the Wigner-Seitz cell, ω is the phonon frequency, $\hbar$ is the reduced Planck's constant, f is the number density of the participating phonons, Φ is the matrix element taken from Fermi's Golden Rule, $\boldsymbol{v}_n'$ is the velocity normal to the surface of constant energy $S_{\boldsymbol{K}}$.

A number of challenges must be overcome in order to implement this scattering term in COMET successfully. We must first compute the list of three-phonon interactions which satisfy energy and momentum conservation. From a numerical standpoint this is inherently inexact when dealing with a discrete wave vector space. Because of this, the full scattering kernel is not guaranteed to conserve energy unless extra steps are taken to do so. From a computational standpoint, for a three dimensional material the size of the wave vector space can easily approach several thousand $\boldsymbol{K}$-space control volumes to obtain the granularity necessary for accurate calculations. The number of operations necessary to compute the source term for all phonons at one particular spatial location is $O(N^2)$, if N is the number of phonon groups being resolved. Such scaling can easily lead to computations which approach the limit of current CPU

power. However, the calculation is extremely parallelizable, suggesting that significant computational gains may be had by using GPUs or other parallel platforms for the source term calculation.

Another challenge is how to develop a COMET algorithm for the specific form of the scattering term in Eq. (61). We saw earlier that the point coupled algorithm becomes very expensive computationally when the point matrix is dense, or if its structure makes it difficult to invert. Inexpensive strategies for this point inversion must be developed.

IMPROVED SIMULATION OF NANOCOMPOSITES.

The previous chapter studied the transport of phonons through nanoparticle composites at various temperatures, and at two different domain sizes. Two main simplifications were made: two dimensional transport and small temperature differences. Though our 2D simulations yield the expected qualitative trends, the topological connectivity of two- and three-dimensional networks is quite different, and moving to three dimensions is critical for making quantitative predictions. In addition, it was found that the main parameter of interest in reducing the thermal conductivity is the surface area to volume ratio. Depending on the size, shape, and spacing between particles, this ratio can be several times larger in three dimensions than it is in two dimensions. Thus, to get an accurate representation of real nanoparticle composites, a fully three dimensional domain must be considered. Given that a thermoelectric device is simply a solid state heat engine, greater efficiency is achieved when the difference between the hot and cold reservoir is increased. These devices will be operating with temperature differences which are much larger than 1 K. We must therefore explore phonon transport under conditions of variable specific heat, and possibly variable transmission coefficients, if anharmonic effects are appreciable.

SIMULATIONS OF THERMOELECTRIC PERFORMANCE.

In Chapter 5, we simulated phonon transport in nanoparticle composites because of their recent appearance in the thermoelectric materials design. As was mentioned earlier, the thermoelectric figure of merit, $ZT=S^2\sigma T/k$, is also largely dependent on the transport of electrons in the nanocomposite. Often times, electron and phonon transport may not be treated as decoupled physics, and accurate simulation must include coupling. As an example, high optical phonon populations may reduce electrical conductivity which would reduce the figure of merit.

It would therefore be extremely advantageous to develop an integrated electron BTE which could effectively couple electron and phonon transport. This would also require the installment of a full scattering kernel to achieve high fidelity results where the relaxation time approximation is invalid. Depending on the strength of the coupling between electrons and phonons, new numerical procedures may need to be created to achieve convergence. Given that the electrons and phonons share the same Brillouin zone, it seems plausible to include the electron BTE into the phonon BTE's point coupled matrix to create a block coupled point matrix. However, because of their higher energies, the vast majority electrons responsible for transport reside in a very small portion of the Brillouin zone. Because of this, resolving the entire Brillouin zone for the electron BTE is unnecessary.

VOLUME-AVERAGED THEORY FOR COMPOSITES

We posited that at sufficiently high interface densities, interfacial scattering is analogous to volumetric scattering. From this, we further postulated that the length scale

of this scattering mechanism is proportional to the total volume compared to the interface surface area. These two lend nicely to the idea that it is possible to establish a volume averaged theory for nanocomposites using the BTE. In this formulation, an additional scattering kernel would be included on the right hand side of the BTE. To do this would require choosing a representative elemental volume (REV) over which the averaging occurs. Within this volume one could derive an expression for the interfacial scattering kernel in the following form:

$$\left(\frac{\partial e''}{\partial t}\right)_{\text{int}} = -\sigma e'' + \sum_{\varepsilon'} \int_{BZ} e''(\boldsymbol{K}', \varepsilon') \Theta(\boldsymbol{K}, \varepsilon, \boldsymbol{K}', \varepsilon') d^3 \boldsymbol{K}' \tag{62}$$

This kernel is adapted from the radiation literature [108]. Here, σ is a coefficient which determines the rate of energy loss from the phonon. The second term is a summation over all polarizations and integrated over the entire Brillouin zone. $\boldsymbol{K}$ and ε denote the wave vector and polarization of the phonon in question, while $\boldsymbol{K}'$ and ε' denote the dummy variables over which the summation and integration occurs. In the radiation literature Θ is called the scattering phase function, which corresponds to the rate of energy transfer from a phonon in polarization ε' and wave vector $\boldsymbol{K}'$ to a phonon of polarization ε and wave vector $\boldsymbol{K}$. Using a direct numerical solution (DNS) of the BTE in the REV, it would be possible to determine a discrete representation for the scattering phase function and the corresponding σ. Once a suitable scattering kernel is obtained, it would be possible to solve a volume averaged BTE without the need to resolve complex geometry.

References

[1] Fuechsle M., Miwa J. A., Mahapatra S., Ryu H., Lee S., Warschkow O., Hollenberg L. C. L., Klimeck G., and Simmons M. Y., 2012, "A Single-Atom Transistor," Nature Nanotechnology, **7**(4), pp. 242–246.

[2] Bergmair I., Hackl W., Losurdo M., Helgert C., Isic G., Rohn M., Jakovljevic M. M., Mueller T., Giangregorio M., Kley E.-B., Fromherz T., Gajic R., Pertsch T., Bruno G., and Muehlberger M., 2012, "Nano- and Microstructuring of Graphene Using UV-NIL.," Nanotechnology, **23**(33), p. 335301.

[3] Shirak O., Shtempluck O., Kotchtakov V., Bahir G., and Yaish Y. E., 2012, "High Performance Horizontal Gate-all-around Silicon Nanowire Field-effect Transistors.," Nanotechnology, **23**(39), p. 395202.

[4] Olsson III R. H., Fleming J. G., El-Kady I. F., Tuck M. R., and McCormick F. B., 2007, "Micromachined Bulk Wave Acoustic Bandgap Devices," International Conference on Solid-State Sensors, Actuators, and Microsystems, Lyon, France, pp. 317–321.

[5] Jensen B. D., Member S., Mutlu S., Miller S., Kurabayashi K., and Allen J. J., 2003, "Shaped Comb Fingers for Tailored Electromechanical Restoring Force," **12**(3), pp. 373–383.

[6] Liu X., Member S., Katehi L. P. B., Chappell W. J., and Peroulis D., 2010, "High-Q Tunable Microwave Cavity Resonators and Filters Using SOI-Based RF MEMS Tuners," Journal of Microelectricalmechanical Systems, **19**(4), pp. 774–784.

[7] Barton R. A., Storch I. R., Adiga V. P., Sakakibara R., Cipriany B. R., Ilic B., Wang S. P., Ong P., McEuen P. L., Parpia J. M., and Craighead H. G., 2012, "Photothermal self-oscillation and laser cooling of graphene optomechanical systems.," Nano letters, **12**(9), pp. 4681–6.

[8] 2009, "International Technology Roadmap for Semiconductors," http://www.itrs.net/Links/2009ITRS/Home2009.htm.

[9] Kittel C., 1996, Introduction to Solid State Physics, Wiley, New York, NY.

[10] Kaviany M., 2008, Heat Transfer Physics, Cambridge University Press, New York, NY.

[11] 2011, "International Technology Roadmap for Semiconductors," http://www.itrs.net/Links/2011ITRS/Home2011.htm.

[12] Novoselov K. S., Geim A. K., Morozov S. V., Jiang D., Zhang Y., Dubonos S. V., Grigorieva I. V., and Firsov A. A., 2004, "Electric Field Effect in Atomically Thin Carbon Films," Science, **306**, pp. 666–669.

[13] Reina A., Jia X., Ho J., Nezich D., Son H., Bulovic V., Dresselhaus M. S., and Kong J., 2009, "Large area, few-layer graphene films on arbitrary substrates by chemical vapor deposition.," Nano letters, **9**(1), pp. 30–5.

[14] Cai J., Ruffieux P., Jaafar R., Bieri M., Braun T., Blankenburg S., Muoth M., Seitsonen A. P., Saleh M., Feng X., Müllen K., and Fasel R., 2010, "Atomically precise bottom-up fabrication of graphene nanoribbons.," Nature, **466**(7305), pp. 470–3.

[15] Han M., Özyilmaz B., Zhang Y., and Kim P., 2007, "Energy Band-Gap Engineering of Graphene Nanoribbons," Physical Review Letters, **98**(20), pp. 1–4.

[16] Iijima S., and Ichihashi T., 1993, "Single-Shell Carbon Nanotubes of 1-nm diameter," Nature, **363**(603-605).

[17] Tans S. J., Verschueren A. R. M., and Dekker C., 1998, "Room-temperature Transistor based on a Single Carbon Nanotube," Nature, **672**(1989), pp. 669–672.

[18] Zheng G., Lu W., Jin S., and Lieber C. M., 2004, "Synthesis and Fabrication of High-Performance n-Type Silicon Nanowire Transistors," Advanced Materials, **16**(21), pp. 1890–1893.

[19] Cui Y., Duan X., Hu J., and Lieber C. M., 2000, "Doping and Electrical Transport in Silicon Nanowires," The Journal of Physical Chemistry B, **104**(22), pp. 5213–5216.

[20] Kang U., Chung H., Heo S., Park D., Lee H., Kim J. H., Ahn S., Cha S., Ahn J., Kwon D., Lee J., Joo H., Kim W., Jang D. H., Kim N. S., Choi J., Chung T., Yoo J., Choi J. S., Kim C., Member S., Jun Y., An A., and Ddr G., 2010, "8 Gb 3-D DDR3 DRAM Using Through-Silicon-Via Technology," IEEE Journal of Solid-State Circuits, **45**(1), pp. 111–119.

[21] Topol a. W., Tulipe D. C. La, Shi L., Frank D. J., Bernstein K., Steen S. E., Kumar a., Singco G. U., Young a. M., Guarini K. W., and Ieong M., 2006, "Three-dimensional integrated circuits," IBM Journal of Research and Development, **50**(4.5), pp. 491–506.

[22] Fairbanks J. W., 2012, "Automotive Thermoelectric Generators and HVAC," Directions in Engine-Efficiency and Emissions Research, Dearborn, MI.

[23] Administration U. S. E. I., 2013, "http://www.eia.gov/tools/faqs/faq.cfm?id=23&t=10."

[24] Administration U. S. E. I., 2013, "http://www.eia.gov/petroleum/gasdiesel/."

[25] Lundstrom M., 2000, Fundamentals of Carrier Transport, Cambridge University Press, New York, NY.

[26] Venkatasubramanian R., Siivola E., Colpitts T., and O'Quinn B., 2001, "Thin-film Thermoelectric Devices with High Room-Temperature Figures of Merit," Nature, **413**(6856), pp. 597–602.

[27] Mahan G., Sales B., and Sharp J., 1997, "Thermoelectric Materials: New Approaches to an Old Problem," Physics Today, **50**(3), pp. 42–47.

[28] Harman T. C., Taylor P. J., Walsh M. P., and Laforge B. E., 2002, "Quantum Dot Superlattice Thermoelectric Materials and Devices," Science, **297**, pp. 2229–2232.

[29] Poudel B., Hao Q., Ma Y., Lan Y., Minnich A., Yu B., Yan X., Wang D., Muto A., Vashaee D., Chen X., Liu J., Dresselhaus M. S., Chen G., and Ren Z., 2008, "High-Thermoelectric Performance of Nanostructured Bismuth Antimony Telluride Bulk Alloys," Science, **320**(5876), pp. 634–8.

[30] Zebarjadi M., Joshi G., Zhu G., Yu B., Minnich A., Lan Y., Wang X., Dresselhaus M., Ren Z., and Chen G., 2011, "Power Factor Enhancement by Modulation Doping in Bulk Nanocomposites," Nano Letters, **11**, pp. 2225–2230.

[31] Yu B., Zebarjadi M., Wang H., Lukas K., Wang H., Wang D., Opeil C., Dresselhaus M., Chen G., and Ren Z., 2012, "Enhancement of Thermoelectric Properties by Modulation-Doping in Silicon Germanium Alloy Nanocomposites.," Nano letters, pp. 6–11.

[32] Hsu K. F., Loo S., Guo F., Chen W., Dyck J. S., Uher C., Hogan T., Polychroniadis E. K., and Kanatzidis M. G., 2004, "Cubic AgPb(m) SbTe(2+m) : Bulk Thermoelectric Materials with High Figure of Merit," Science, **303**, pp. 818–821.

[33] Walraven J. A., 2003, "Failure Mechanisms in MEMS," International Test Conference, pp. 828–833.

[34] Merlijn van Spengen W., 2003, "MEMS reliability from a failure mechanisms perspective," Microelectronics Reliability, **43**(7), pp. 1049–1060.

[35] Majumdar A., 1993, "Microscale Heat Conduction in Dielectric Thin Films," ASME Journal of Heat Transfer, **115**, pp. 7–16.

[36] Sun L., and Murthy J. Y., 2006, "Domain Size Effects in Molecular Dynamics Simulation of Phonon Transport in Silicon," Applied Physics Letters, **89**(17), p. 171919.

[37] McGaughey A. J. H., and Kaviany M., 2006, "Phonon Transport in Molecular Dynamics Simulations : Formulation and Thermal Conductivity Prediction," Advances in Heat Transfer, **39**, pp. 169–255.

[38] Narumanchi S. V. J., Murthy J. Y., and Amon C. H., 2005, "Boltzmann Transport Equation-Based Thermal Modeling Approaches for Hotspots in Microelectronics," Heat and Mass Transfer, **42**(6), pp. 478–491.

[39] Bansal A., Meterelliyoz M., Singh S., Murthy J., and Roy K., 2006, "Compact Thermal Models for Estimation of Temperature-Dependent Power/Performance in finFET Technology," Asia and South Pacific Conference on Design Automation, 2006., pp. 237–242.

[40] Narumanchi S. V. J., Murthy J. Y., and Amon C. H., 2004, "Submicron Heat Transport Model in Silicon Accounting for Phonon Dispersion and Polarization," ASME Journal of Heat Transfer, **126**(6), p. 946.

[41] Murthy J. Y., and Mathur S. R., 2002, "Computation of Sub-Micron Thermal Transport Using an Unstructured Finite Volume Method," ASME Journal of Heat Transfer, **124**(6), p. 1176.

[42] Bazant M. Z., Kaxiras E., and Justo J. F., 1997, "Environment-Dependent Interatomic Potential for Bulk Silicon," Physical Review B, **56**(14), pp. 8542–8552.

[43] Pascual-Gutiérrez J., Murthy J. Y., and Viskanta R., 2009, "Thermal Conductivity and Phonon Transport Properties of Silicon Using Perturbation Theory and the Environment-Dependent Interatomic Potential," Journal of Applied Physics, **106**(6), p. 063532.

[44] Klemens P. G., 1951, "The Thermal Conductivity of Dielectric Solids at Low Temperatures (Theoretical)," Proceedings of the Royal Society A: Mathematical, Physical and Engineering Sciences, **208**(1092), pp. 108–133.

[45] Callaway J., 1959, "Model for Lattice Thermal Conductivity at Low Temperatures," Physical Review, **113**(4), pp. 1046–1051.

[46] Holland M. G., 1963, “Analysis of Lattice Thermal Conductivity,” Physical Review, **132**(6), pp. 2461–2471.

[47] Ziman J. M., 1963, Electrons and Phonons, Oxford University Press, Oxford.

[48] Ladd A. J. C., Moran B., and Hoover W. G., 1986, “Lattice Thermal Conductivity: A Comparison of Molecular Dynamics and Anharmonic Lattice Dynamics,” Physical Review B, **34**(8), pp. 5058–5064.

[49] McGaughey A. J. H., and Kaviany M., 2004, “Quantitative validation of the Boltzmann transport equation phonon thermal conductivity model under the single-mode relaxation time approximation,” Physical Review B, **69**(9), p. 094303.

[50] Henry A. S., and Chen G., 2008, “Spectral Phonon Transport Properties of Silicon Based on Molecular Dynamics Simulations and Lattice Dynamics,” Journal of Computational and Theoretical Nanoscience, **5**(2), pp. 1–12.

[51] Thomas J. a., Turney J. E., Iutzi R. M., Amon C. H., and McGaughey A. J. H., 2010, “Predicting phonon dispersion relations and lifetimes from the spectral energy density,” Physical Review B, **81**(8), pp. 1–4.

[52] Khalatnikov I. M., 1952, “Teploobmen mezhdu tverdym telom i geliem -II,” Journal of Experimental and Theoretical Physics, **22**(6), pp. 687–704.

[53] Little W. A., 1959, “The Transport of Heat Between Dissimilar Solids at Low Temperatures,” Canadian Journal of Physics, **37**(3), pp. 334–349.

[54] Schelling P. K., Phillpot S. R., and Keblinski P., 2002, “Phonon wave-packet dynamics at semiconductor interfaces by molecular-dynamics simulation,” Applied Physics Letters, **80**(14), p. 2484.

[55] Swartz E. T., and Pohl R. O., 1987, “Thermal Resistance at Interfaces,” Applied Physics Letters, **51**(26), pp. 2200–2202.

[56] Stevens R. J., Smith A. N., and Norris P. M., 2005, “Measurement of Thermal Boundary Conductance of a Series of Metal-Dielectric Interfaces by the Transient Thermoreflectance Technique,” Journal of Heat Transfer, **127**(3), p. 315.

[57] Costescu R. M., Wall M. A., and Cahill D. G., 2003, “Thermal conductance of epitaxial interfaces,” Physical Review B, **67**(5), p. 054302.

[58] Stoner R. J., and Maris H. J., 1993, "Kapitza Conductance and Heat Flow Between Solids at Temperatures from 50 to 300 K," Physical Review B, **48**(22), pp. 16373–16387.

[59] Hopkins P. E., Norris P. M., and Stevens R. J., 2008, "Influence of Inelastic Scattering at Metal-Dielectric Interfaces," Journal of Heat Transfer, **130**(2), p. 022401.

[60] Zhang W., Fisher T. S., and Mingo N., 2007, "The Atomistic Green's Function Method: An Efficient Simulation Approach for Nanoscale Phonon Transport," Numerical Heat Transfer, Part B: Fundamentals, **51**, pp. 333–349.

[61] Tian Z., Esfarjani K., and Chen G., 2012, "Enhancing Phonon Transmission Across a Si/Ge Interface by Atomic Roughness: First-Principles Study with the Green's Function Method," Physical Review B, **86**(23), p. 235304.

[62] Datta S., 2005, Quantum Transport: Atom to Transistor, Cambridge University Press, Cambridge.

[63] Li X., and Yang R., 2012, "Size-dependent phonon transmission across dissimilar material interfaces.," Journal of physics. Condensed matter : an Institute of Physics journal, **24**(15), p. 155302.

[64] Zhang W., Fisher T. S., and Mingo N., 2007, "Simulation of Interfacial Phonon Transport in Si–Ge Heterostructures Using an Atomistic Green's Function Method," Journal of Heat Transfer, **129**(4), p. 483.

[65] Omini M., and Sparavigna a, 1995, "An iterative approach to the phonon Boltzmann equation in the theory of thermal conductivity," Physica B: Condensed Matter, **212**(2), pp. 101–112.

[66] Omini M., and Sparavigna A., 1996, "Beyond the Isotropic-Model Approximation in the Theory of Thermal Conductivity," Physical Review B, **53**(14), pp. 9064–9073.

[67] Broido D. A., Ward A., and Mingo N., 2005, "Lattice Thermal Conductivity of Silicon from Empirical Interatomic Potentials," Physical Review B, **72**(1), p. 014308.

[68] Sparavigna A., 2002, "Influence of Isotope Scattering on the Thermal Conductivity of Diamond," Physical Review B, **65**(6), p. 064305.

[69] Sparavigna A., 2002, “Lattice thermal conductivity in cubic silicon carbide,” Physical Review B, **66**(17), p. 174301.

[70] Broido D., and Reinecke T., 2004, “Lattice Thermal Conductivity of Superlattice Structures,” Physical Review B, **70**(8), p. 081310.

[71] Ward A., and Broido D., 2008, “Intrinsic Lattice Thermal Conductivity of Si/Ge and GaAs/AlAs Superlattices,” Physical Review B, **77**(24), p. 245328.

[72] Broido D. A., Malorny M., Birner G., Mingo N., and Stewart D. A., 2007, “Intrinsic Lattice Thermal Conductivity of Semiconductors from First Principles,” Applied Physics Letters, **91**(23), p. 231922.

[73] Ward A., and Broido D. A., 2010, “Intrinsic Phonon Relaxation Times from First-Principles Studies of the Thermal Conductivities of Si and Ge,” Physical Review B, **81**(8), pp. 1–5.

[74] Ward A., Broido D., Stewart D., and Deinzer G., 2009, “Ab Initio Theory of the Lattice Thermal Conductivity in Diamond,” Physical Review B, **80**(12), pp. 1–8.

[75] Singh D., Murthy J. Y., and Fisher T. S., 2011, “Mechanism of thermal conductivity reduction in few-layer graphene,” Journal of Applied Physics, **110**(4), p. 044317.

[76] Singh D., Murthy J. Y., and Fisher T. S., 2011, “On the Accuracy of Classical and Long Wavelength Approximations for Phonon Transport in Graphene,” Journal of Applied Physics, **110**(11), p. 113510.

[77] Garg J., Bonini N., Kozinsky B., and Marzari N., 2011, “Role of Disorder and Anharmonicity in the Thermal Conductivity of Silicon-Germanium Alloys: A First-Principles Study,” Physical Review Letters, **106**(4), p. 045901.

[78] Mazumder S., and Majumdar A., 2001, “Monte Carlo Study of Phonon Transport in Solid Thin Films Including Dispersion and Polarization,” ASME Journal of Heat Transfer, **123**(4), p. 749.

[79] Lacroix D., Joulain K., and Lemonnier D., 2005, “Monte Carlo transient phonon transport in silicon and germanium at nanoscales,” Physical Review B, **72**(6), pp. 1–11.

[80] Chen Y., Li D., Lukes J. R., and Majumdar A., 2005, “Monte Carlo Simulation of Silicon Nanowire Thermal Conductivity,” Journal of Heat Transfer, **127**(10), p. 1129.

[81] Jeng M.-S., Yang R., Song D., and Chen G., 2008, "Modeling the Thermal Conductivity and Phonon Transport in Nanoparticle Composites Using Monte Carlo Simulation," Journal of Heat Transfer, **130**(4), p. 042410.

[82] Mittal A., and Mazumder S., 2010, "Monte Carlo Study of Phonon Heat Conduction in Silicon Thin Films Including Contributions of Optical Phonons," ASME Journal of Heat Transfer, **132**, p. 052402.

[83] Hamzeh H., and Aniel F., 2011, "Monte Carlo study of phonon dynamics in III-V compounds," Journal of Applied Physics, **109**(6), p. 063511.

[84] Randrianalisoa J., and Baillis D., 2008, "Monte Carlo Simulation of Steady-State Microscale Phonon Heat Transport," ASME Journal of Heat Transfer, **130**(7), p. 072404.

[85] Pascual-Gutierrez J. A., 2010, "On the Theory of Phonons: A Journey from their Origins to the Intricate Mechanisms of their Transport," Purdue University.

[86] Péraud J.-P. M., and Hadjiconstantinou N. G., 2011, "Efficient Simulation of Multidimensional Phonon Transport Using Energy-Based Variance-Reduced Monte Carlo Formulations," Physical Review B, **84**(20), p. 205331.

[87] Péraud J.-P. M., and Hadjiconstantinou N. G., 2012, "An alternative Approach to Efficient Simulation of Micro/Nanoscale Phonon Transport," Applied Physics Letters, **101**(15), p. 153114.

[88] Rahman A., 1964, "Correlations in the Motion of Atoms in Liquid Argon," Physical Review, **136**(2A), pp. A405–A411.

[89] Stillinger F. H., and Weber T. A., 1985, "Computer Simulation of Local Order in Condensed Phases of Silicon," Physical Review B, **31**(8), pp. 5262–5271.

[90] Tersoff J., 1988, "New Empirical Approach for the Structure and Energy of Covalent Systems," Physical Review B, **37**(12), pp. 6691–7000.

[91] Gonze X., and Lee C., 1997, "Dynamical matrices, Born effective charges, dielectric permittivity tensors, and interatomic force constants from density-functional perturbation theory," Physical Review B, **55**(16), pp. 10355–10368.

[92] Zhong Z., Wang X., and Xu J., 2004, "Equilibrium Molecular Dynamics Study of Phonon Thermal Transport in Nanomaterials," Numerical Heat Transfer, Part B: Fundamentals, **46**(5), pp. 429–446.

[93] Müller-Plathe F., 1997, "A Simple Nonequilibrium Molecular Dynamics Method for Calculating the Thermal Conductivity," The Journal of Chemical Physics, **106**(14), p. 6082.

[94] Schelling P. K., Phillpot S. R., and Keblinski P., 2002, "Comparison of Atomic-Level Simulation Methods for Computing Thermal Conductivity," Physical Review B, **65**(14), p. 144306.

[95] Goicochea J. V., Madrid M., and Amon C., 2010, "Hierarchical Modeling of Heat Transfer in Silicon-Based Electronic Devices," Journal of Heat Transfer, **132**(10), p. 102401.

[96] Goicochea J. V., Madrid M., and Amon C., 2010, "Thermal Properties for Bulk Silicon Based on the Determination of Relaxation Times Using Molecular Dynamics," Journal of Heat Transfer, **132**(1), p. 012401.

[97] Narumanchi S. V. J., Murthy J. Y., and Amon C. H., 2005, "Comparison of Different Phonon Transport Models for Predicting Heat Conduction in Silicon-on-Insulator Transistors," Journal of Heat Transfer, **127**(7), p. 713.

[98] Murthy J. Y., and Mathur S. R., 2003, "An Improved Computational Procedure for Sub-Micron Heat Conduction," ASME Journal of Heat Transfer, **125**(5), p. 904.

[99] Chai J. C., Lee H. S., and Patankar S. V., 1994, "Finite Volume Method for Radiation Heat Transfer," Journal of Thermophysics and Heat Transfer, **8**(3), pp. 419–425.

[100] Raithby G. D., and Chui E. H., 1990, "A Finite-Volome Method for Predicting a Radiant Heat Transfer in Enclosures With Participating Media," ASME Journal of Heat Transfer, **112**(2), pp. 415–423.

[101] Patankar S. V., 1980, Numerical Heat Transfer and Fluid Flow, Taylor & Francis, New York, NY.

[102] Boltzmann L., 1964, Lectures Notes on Gas Theory, Translated from the German Edition, Dover, New York, NY.

[103] Mathur S. R., and Murthy J. Y., 1999, "Coupled Ordinates Method for Multigrid Acceleration of Radiation Calculations," Journal of Thermophysics and Heat Transfer, **13**(4), pp. 467–473.

[104] Mazumder S., 2005, "A New Numerical Procedure for Coupling Radiation in Participating Media With Other Modes of Heat Transfer," Journal of Heat Transfer, **127**(9), p. 1037.

[105] Brandt A., and Livne O. E., 2011, Multigrid Techniques, SIAM, Philadelphia, PA.

[106] Mathur S. R., and Murthy J. Y., 1997, "A Pressure-Based Method for Unstructured Meshes," Numerical Heat Transfer, Part B: Fundamentals, **31**, pp. 195–217.

[107] Heaslet M. A., and Warming R. F., 1965, "Radiative Transport and Wall Temperature Slip in an Absorbing Planar Medium," International Journal of Heat and Mass Transfer, **8**, pp. 979–994.

[108] Modest M. F., 1993, Radiative Heat Transfer, New York, NY.

[109] Gironcoli S. De, 1992, "Phonons in Si-Ge Systems: An ab initio Interatomic-force-constant Approach," Physical Review B, **46**(4).

[110] Mingo N., Yang L., Li D., and Majumdar A., 2003, "Predicting the Thermal Conductivity of Si and Ge Nanowires," Nano Letters, **3**(12), pp. 1713–1716.

[111] Karypis G., and Kumar V., 1997, "A Coarse-Grain Parallel Formulation of Multilevel k-way Graph Partitioning Algorithm," 8th SIAM Conference on Parallel Processing for Scientific Computing, pp. 1–12.

[112] Swartz E. T., and Pohl R. O., 1989, Thermal Boundary Resistance.

[113] Landry E., and McGaughey a., 2009, "Effect of interfacial species mixing on phonon transport in semiconductor superlattices," Physical Review B, **79**(7), pp. 29–34.

[114] Singh D., Murthy J. Y., and Fisher T. S., 2011, "Effect of Phonon Dispersion on Thermal Conduction Across Si/Ge Interfaces," ASME Journal of Heat Transfer, **133**(12), p. 122401.

[115] Loy J. M., Mathur S. R., and Murthy J. Y., 2013, "A Coupled Ordinates Method for the Convergence Acceleration of the Phonon Boltzmann Transport Equation," ASME Journal of Heat Transfer, (Submitted).

[116] "http://www.ctcms.nist.gov/oof/oof2/."

[117] Chen G., 1997, “Size and Interface Effects on Thermal Conductivity of Superlattices and Periodic Thin-Film Structures,” ASME Journal of Heat Transfer, **119**, pp. 220–229.

[118] Yang R., and Chen G., 2004, “Thermal conductivity modeling of periodic two-dimensional nanocomposites,” Physical Review B, **69**(19), pp. 1–10.

[119] Tian W., and Yang R., 2007, “Thermal conductivity modeling of compacted nanowire composites,” Journal of Applied Physics, **101**(5), p. 054320.

[120] Tian W., and Yang R., 2007, “Effect of Interface Scattering on Phonon Thermal Conductivity Percolation in Random Nanowire Composites,” Applied Physics Letters, **90**(26), p. 263105.

[121] Hsieh T.-Y., and Yang J.-Y., 2010, “Thermal conductivity modeling of circular-wire nanocomposites,” Journal of Applied Physics, **108**(4), p. 044306.

[122] Singh D., 2011, “Frequency and Polarization Resolved Phonon Transport in Carbon and Silicon Nanostructures,” Purdue University.

[123] Minnich A. J., Dresselhaus M. S., Ren Z. F., and Chen G., 2009, “Bulk nanostructured thermoelectric materials: current research and future prospects,” Energy & Environmental Science, **2**(5), p. 466.

[124] Harrison W. A., 9189, Electronic Structure and the Properties of Solids, Dover, Mineola, NY.

[125] Glassbrenner C. J., and Slack G. A., 1966, “Thermal Conductivity of Silicon and Germanium from 3 K to the Melting Point,” Physical Review, **134**(4A), pp. A1058–A1069.

[126] Loy J. M., Murthy J. Y., and Singh D., 2013, “A Fast Hybrid Fourier–Boltzmann Transport Equation Solver for Nongray Phonon Transport,” ASME Journal of Heat Transfer, **135**(1), p. 011008.